Design, Development, and Control of an Assistive Robotic Exoskeleton Glove Using Reinforcement Learning-Based Force Planning for Autonomous Grasping

Wenda Xu

Dissertation submitted to the Faculty of the
Virginia Polytechnic Institute and State University
in partial fulfillment of the requirements for the degree of

Doctor of Philosophy
in
Mechanical Engineering

Pinhas Ben-Tzvi, Chair
Corina Sandu
Steve Southward
A. Lynn Abbott

September 8th, 2023
Blacksburg, Virginia

Keywords: Wearable Devices, Mechanical Design, Kinematics, Dynamics and Control, exoskeleton, Motion Planning, Reinforcement Learning.

Design, Development, and Control of an Assistive Robotic Exoskeleton Glove Using Reinforcement Learning-Based Force Planning for Autonomous Grasping

Wenda Xu

(ABSTRACT)

This dissertation presents a comprehensive exploration encompassing the design, development, control and the application of reinforcement learning-based force planning for the autonomous grasping capabilities of the innovative assistive robotic exoskeleton gloves. Exoskeleton devices have emerged as a promising avenue for providing assistance to individuals with hand disabilities, especially those who may not achieve full recovery through surgical interventions. Nevertheless, prevailing exoskeleton glove systems encounter a multitude of challenges spanning design, control, and human-machine interaction. These challenges have given rise to limitations, such as unwieldy bulkiness, an absence of precise force control algorithms, limited portability, and an imbalance between lightweight construction and the essential functionalities required for everyday activities.

To address these challenges, this research undertakes a comprehensive exploration of various dimensions within the exoskeleton glove system domain. This includes the intricate design of the finger linkage mechanism, meticulous kinematic analysis, strategic kinematic synthesis, nuanced dynamic modeling, thorough simulation, and adaptive control. The development of two distinct types of series elastic actuators, coupled with the creation of two diverse exoskeleton glove designs based on differing mechanisms, constitutes a pivotal aspect of this study.

For the exoskeleton glove integrated with series elastic actuators, a sophisticated dynamic

model is meticulously crafted. This endeavor involves the formulation of a mathematical framework to address backlash and the subsequent mitigation of friction forces. The pursuit of accurate force control culminates in the proposition of a data-driven model-free force predictive control policy, compared with a dynamic model-based force control methodology. Notably, the efficacy of the system is validated through meticulous clinical experiments.

Meanwhile, the low-profile exoskeleton glove design with a novel mechanism engages in a further reduction of size and weight. This is achieved through the integration of a rigid coupling hybrid mechanism, yielding pronounced advancements in wearability and comfortability. A deep reinforcement learning approach is adopted for the real-time force planning control policies. A simulation environment is built to train the reinforcement learning agent.

In summary, this research endeavors to surmount the constraints imposed by existing exoskeleton glove systems. By virtue of advancing mechanism design, innovating control strategies, enriching perception capabilities, and enhancing wearability, the ultimate goal is to augment the functionality and efficacy of these devices within the realm of assistive applications.

Design, Development, and Control of an Assistive Robotic Exoskeleton Glove Using Reinforcement Learning-Based Force Planning for Autonomous Grasping

Wenda Xu

(GENERAL AUDIENCE ABSTRACT)

This dissertation presents a comprehensive exploration encompassing the design, development, control and the application of reinforcement learning-based force planning for the autonomous grasping capabilities of the innovative assistive robotic exoskeleton gloves. Exoskeleton devices hold significant promise as valuable aids for patients with hand disabilities who may not achieve full recuperation through surgical interventions. However, the present iteration of exoskeleton glove systems encounters notable limitations in terms of design, control mechanisms, and human-machine interaction. Specifically, prevailing systems often suffer from bulkiness, lack of portability, and an inadequate equilibrium between lightweight construction and the essential functionalities imperative for daily tasks.

To address these challenges, this research undertakes a comprehensive exploration of diverse facets within the exoskeleton glove system domain. This encompasses a detailed focus on mechanical design, control strategies, and human-machine interaction. To address wearability and comfort, two distinct exoskeleton glove variations are devised, each rooted in different mechanisms. An innovative data-driven model-free force predictive control policy is posited to enable accurate force regulation. Rigorous clinical experiments are conducted to meticulously validate the efficacy of the system. Furthermore, a novel mechanism is seamlessly integrated into the design of a new low-profile exoskeleton glove, thereby augmenting wearability and comfort by minimizing size and weight. A deep reinforcement learning based

control agent, which is trained within a simulation environment, is devised to facilitate real-time autonomous force planning.

In summary, the overarching objective of this research lies in rectifying the limitations inherent in existing exoskeleton glove systems. By spearheading advancements in mechanical design, control methodologies, perception capabilities, and wearability, the ultimate aim is to substantially enhance the functionality and overall efficacy of these devices within the sphere of assistive applications.

Dedication

This dissertation is dedicated to

My parents: Zhiqiang Xu and Qingzhi Ma

Acknowledgments

I want to express my profound gratitude to Dr. Pinhas Ben-Tzvi, my Ph.D. advisor, for introducing me to the captivating realm of exoskeleton robotics. I am particularly appreciative of his sharp intuition, refined taste in research directions, and openness to my explorations of the unknown. Dr. Ben-Tzvi also served as a mentor in my personal life, offering solace during difficult times, inspiring me to strive for higher goals when I became too comfortable, and providing invaluable advice and assistance in my life decisions. His passion for his work always motivates me and reinforces my belief in hard work.

I would like to extend my gratitude to my dissertation committee members, Dr. Corina Sandu, Dr. Steve Southward, and Dr. A. Lynn Abbott, for their diligent examination of my research work and valuable feedback.

I would also like to thank my colleagues and collaborators in the Robotics and Mechatronics Lab, including Dr. Hailin Ren, Dr. Yujiong Liu, Dr. Yunfei Guo, and many others, for guiding me, working alongside me, and achieving exciting discoveries together. Your contributions have made my time in the RMLab joyful and fruitful.

Lastly, I am deeply grateful to my parents, Mr. Zhiqiang Xu and Mrs. Qingzhi Ma, whose love and support are immeasurable in my life. Without you, all of my accomplishments would be impossible. I also would like to acknowledge the Research reported in this publication was supported by the Eunice Kennedy Shriver National Institute of Child Health & Human Development of the National Institutes of Health under Award Number R21HD095027. The content is solely the responsibility of the authors and does not necessarily represent the official views of the National Institutes of Health.

Contents

3 Modeling and Development of a Novel Low-profile Exoskeleton Glove 78

List of Figures

List of Tables

List of Abbreviations

ADL: Activities of Daily Living

API: Application Programming Interface

BPI: Brachial Plexus Injuries

BT: Bluetooth

CMC: Carpo-Metacarpa

CNN: Convolution Neural Network

CPM: Continuous Passive Motion

CVASV: Configurable Voice Activation and Speaker Verification

DDPG: Deep Deterministic Policy Gradient

DIP: Distal Interphalangeal

DOF: Degree of Freedom

DRL: Deep Reinforcement Learning

EEG: Electroencephalogram

EMG: Electromyography

EOG: Electrooculogram

FSC: Force Sensing Capacitor

FSR: Force Sensing Resistor

HMI: Human Machine Interface

IP: Interphalangeal

LASSO: Least Absolute Shrinkage and Selection Operator

LSEA: Linear Series Elastic Actuator

MAPE: Mean Absolute Percentage Error

MCP: Metacarpophalangeal

MSE: Mean Squared Error

PCB: Printed Circuit Board

PIP: Proximal Interphalangeal

PM: Parallel Mechanism

PPO: Proximal Policy Optimization

RCHM: Rigid Coupling Hybrid Mechanism

RCM: Rigid Coupling Mechanism

RCoM: Remote Center of Motion

RMSE: Root Mean Squared Error

RSEA: Rotary Series Elastic Actuator

SEA: Series Elastic Actuator

sEMG: Surface Electromyogram

Chapter 1

Introduction

1.1 Motivation

Upper body impairments that affect the ability to lift or grasp objects are prevalent among a significant number of individuals in the United States. According to statistics, approximately 19.9 million people in the country suffer from such impairments [1]. Among them, 6.7 million individuals face challenges in grasping everyday objects, leading to difficulties in performing essential activities of daily living (ADLs) such as holding a cup or a pencil.

One of the major causes of upper body impairments is brachial plexus injury (BPI), typically resulting from motor vehicle accidents and extreme sporting accidents [2]. It is a severe peripheral nerve injury that primarily affects the upper extremities, causing functional damage and physical disability [3]. Patients with BPI, as depicted in Figure 1.1, commonly experience a loss of muscle control and sensations in the shoulder, arm, and hand. Studies suggest that immediate inpatient rehabilitation intervention following BPI has positive effects on overall functional recovery [4, 5].

While surgical interventions have shown success in restoring shoulder and arm function, they are less effective in regaining sensation and mobility in the hand due to the considerable distance between the injured nerves and the targeted rehabilitation zone [6]. As a result, patients with BPI often struggle with hand-related tasks essential for ADLs, significantly impacting their quality of life. Addressing the challenges associated with hand impairments in BPI patients requires innovative rehabilitation approaches and technologies.

Figure 1.1: The patients suffer from brachial plexus injury. Their soft and weakened hands result in a loss of muscle control and sensations.

In this situation, robotic exoskeletons provide a promising solution to help patients with upper body impairments regain lost hand function. Unlike end-effector systems that manipulate the hand from a distant point, exoskeletons attach directly to the human hand and move in synchronization with the joints of the fingers and thumb. This close integration opens up a wide range of possibilities, including strength augmentation and the ability to provide additional structural support and corrective assistance. By harnessing the power of robotic exoskeletons, we have the potential to significantly improve the quality of life for patients with hand disabilities.

1.2 Literature Review

In recent years, there has been a surge in the development of hand rehabilitation exoskeletons, with around 46 daily assistance devices being created [7]. Wearable devices, in particular, have garnered significant attention due to their portability compared to traditional stationary devices [8, 9].

Among wearable devices, motorized hand exoskeletons have emerged as a promising solution for rehabilitation practices. These exoskeletons are worn on the hand and fingers and utilize artificial actuators like electric motors and pneumatic chambers to induce finger movement. By providing external joint torque or force, these devices can assist in improving voluntary grasping motion during daily activities and support neuromuscular practice through repetitive motions. This not only benefits patients by enhancing their rehabilitation experience but also reduces the labor-intensive demands on healthcare providers.

Until the early 2010s, conventional hand exoskeletons mainly relied on rigid linkage/joint mechanisms. However, the past decade has witnessed remarkable advancements in 3D-printing technology and sensing mechanisms, enabling rapid fabrication and design trials, resulting in faster prototyping of hand exoskeleton systems. Additionally, progress in artificial intelligence and portable electronics has contributed to more autonomous control and user-friendly interfaces in these devices. Consequently, rehabilitative hand exoskeletons have seen substantial growth, leading to an increased number of publications in the field and reflecting the overall growth of rehabilitation robotics.

These developments hold great promise for transforming hand rehabilitation by providing innovative, efficient, and user-friendly solutions. As technology and research continue to progress, the capabilities and accessibility of hand exoskeletons will further improve, ultimately enhancing rehabilitation outcomes for individuals with hand impairments. It is anticipated that motorized hand exoskeletons will increasingly play a critical role in rehabilitation practices, contributing to the well-being and quality of life of patients.

In the realm of wearable exoskeletons, various transmission mechanisms are employed, leading to three main categories of hand exoskeleton systems: soft robotic gloves powered by pneumatic/hydraulic actuators, Tendon/Bowden-driven exoskeleton gloves, and linkage-driven exoskeleton gloves. Each of these categories offers distinct advantages and disadvantages, depending on the specific design requirements.

1.2.1 Soft Robotic Gloves

Soft robotic gloves [10, 11, 12, 13, 14, 15, 16, 17, 18] are designed with a soft and flexible structure to provide a natural and comfortable fit (Fig. 1.2). They typically consist of pneumatic/hydraulic actuators, control valves, and inflatable elastic actuators. The use of compliant materials allows these gloves to accommodate different hand shapes and sizes. The actuators are placed on each finger or joint and induce bending/contraction movements. On average, the wearable part of this type of exoskeleton hand weighs only about 162g, making it lightweight and easy to wear. The compliant and soft nature of these actuators enables shape-adaptive behavior and passive safety characteristics, allowing direct actuation of the fingers without the need for complex transmission parts.

Figure 1.2: Soft robotic exoskeleton glove system in the last decade. The compliant inflatable elastic segments actuated by the pneumatic actuators cover the whole hand.

However, a limitation of these design innovations is the requirement to use thick inflatable segments over the fingers for achieving bending. The inflatable actuators consume a significant portion of the wearable part's volume, resulting in larger average volume compared to rigid linkage-type exoskeletons. The pneumatic/hydraulic-based systems often need to be actuated by a relatively large pump, which raises challenges to the portability of these devices [19]. Few studies have addressed the issue of system portability in the context of pneumatic/hydraulic-based hand exoskeletons.

Additionally, the control system and pneumatic infrastructure can become complex due to the non-linearity of the soft actuators made from hyperelastic materials like silicone, necessitating careful calibration, maintenance, and support. Devices driven by hydraulic actuators face similar challenges in terms of control and maintenance complexity.

1.2.2 Tendon/Bowden-driven Gloves

Tendon-driven and Bowden-driven gloves, as demonstrated in various studies [20, 21, 22, 23, 24, 25, 26, 27, 28], is in spired by mechanisms of anatomical finger structures including tendons, ligaments, and muscles in the wearable part, pursuing a biomimetic design (Fig. 1.3). These biomimetic designs utilize high-strength synthetic fibers such as Dyneema, Spectra, and Kevlar to mimic the function of tendons in these exoskeletons. Tendon-driven and Bowden-driven gloves offer the advantage of compact size and remote motor installation. The artificial tendons are guided by flexible routing tubes and are typically placed along the surface of a thin glove made of 3-D printed parts, fabric,and polymer materials; consequently, most of the designs have a very compact wearable part. In the initial tendon-based designs, fabric was generally used to build the wearable part. The functional components of the exoskeleton, such as the tendon routing components, were sewn and anchored to the fabric.

More recently, polymer-based materials such as silicone and urethane with 3D printed parts have been gaining attention as the base structure of the glove due to their high flexibility, durability, and waterproof capabilities mimicking the properties of human skin.

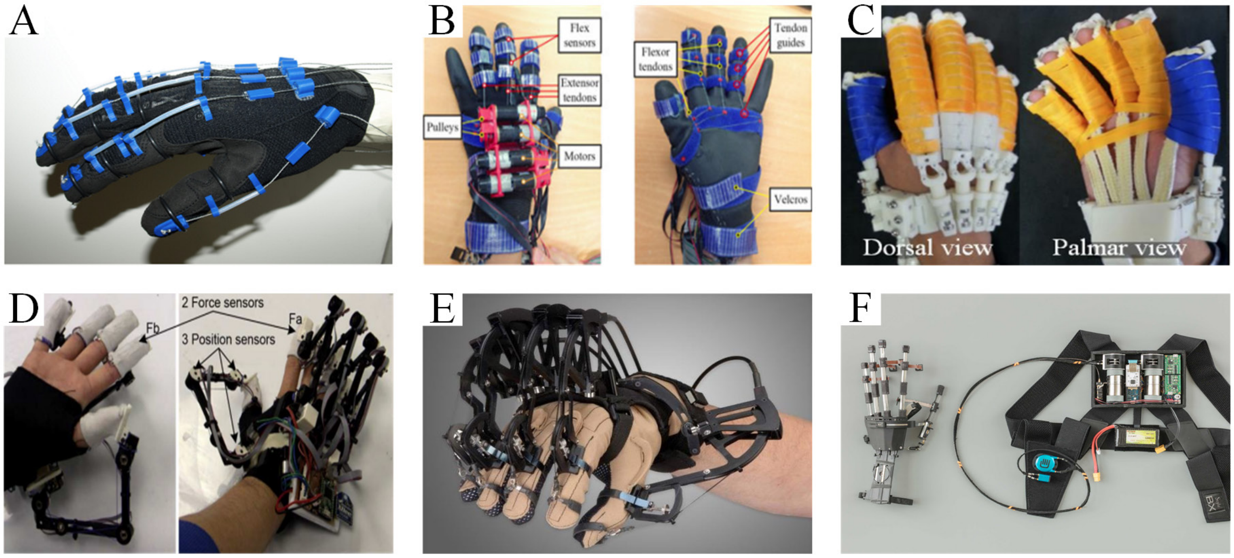

Figure 1.3: Tendon/Bowden driven robotic exoskeleton glove system in the last decade. It uses Tendon/Bowden to replicate the movement of muscle.

The Tendon/Bowden cable transmission, although widely used in exoskeletons glove, has certain limitations, including issues with friction, backlash, and a lower maximum force capacity before cable damage occurs. The thin wearable part of these exoskeletons often lacks sufficient space for embedding sensors, making direct sensing of joint angles or forces challenging. As a result, most tendon-driven exoskeletons employ indirect grasp control by measuring tendon displacement or force at the remote actuation stage.

Furthermore, due to the tendon-driven mechanism, grasping motions in this type of exoskeleton are primarily implemented with an under-actuated approach, utilizing a single tendon per finger. One inherent problem of the tendon-driven mechanism is that the user's finger joints have to withstand a similar amount of tendon tension, which also results in compressive force at the joints. This may cause discomfort and pain for the user during prolonged use.

Another concern is that the sheaths of Bowden cables can exert pressure on the exoskeleton during movement, potentially affecting the user's comfort. Tendon transmissions are susceptible to cable breakage and may require complex cable routing for bidirectional actuation, which could necessitate the use of additional actuators to apply force in the opposite direction.

Moreover, the limited space within the thin wearable part makes it challenging to embed sensors directly in the fingers, which may affect the exoskeleton's sensing capabilities and overall performance. As a consequence, achieving precise and direct control over the fingers can be more difficult in tendon-driven exoskeletons compared to other designs.

1.2.3 Direct Linkage-driven Gloves

Direct linkage transmission gloves, as demonstrated in various studies [29, 30, 31, 32, 33, 34], offer a straightforward, stable, and effective mechanism for transferring force and torque from actuators to hand joints (Fig. 1.4). This mechanism typically involves metallic or 3D-printed rigid bars forming sequential joints or employing 4-bar/redundant linkages. The actuator's spatial motions are directly converted to joint space motions through rigid transmission, allowing encoder signals, current measurements, or torque readings from the actuator to accurately reflect the corresponding finger states. This design ensures intuitive and straightforward hand control. Notably, although only a limited number of studies have reported on grasping force performance, the rigid link type exhibits the highest average precision grasp force (∼10.3 N) among all actuation mechanisms [35].

From a maintenance and reliability perspective, linkage-based fingers are often preferable compared to tendon-driven mechanisms and soft robotics. Moreover, while the mechanical

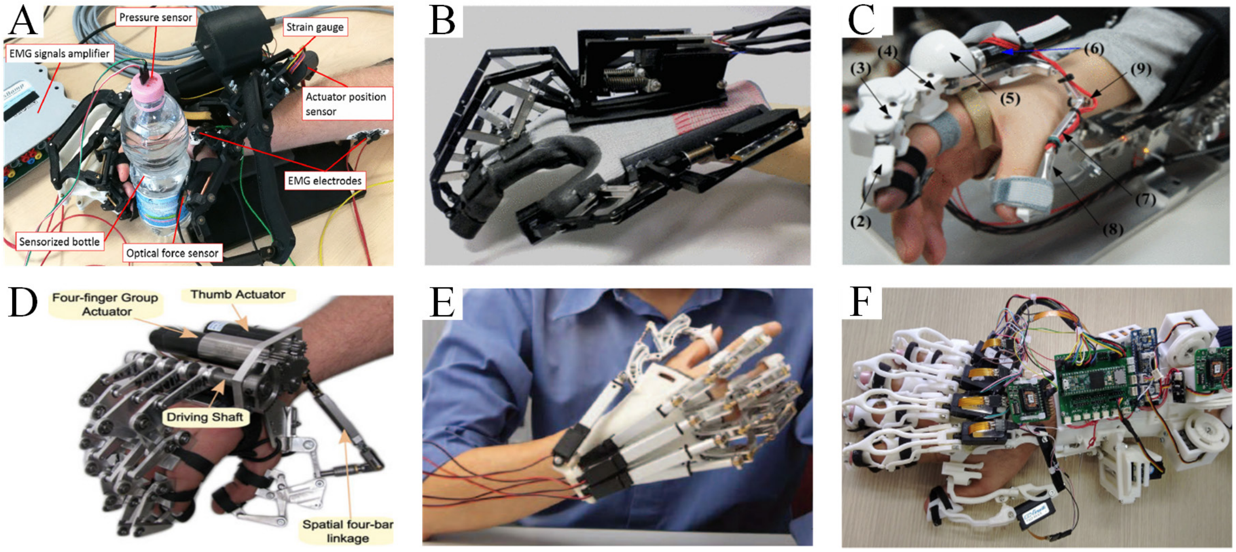

Figure 1.4: Direct linkage-driven robotic exoskeleton glove system in the last decade. It has good stability and reliability due to the mechanical structure.

structure of linkage-based fingers may appear more intricate than that of tendon-driven or pneumatic-driven counterparts, the overall configuration, including the driving mechanism, tends to be simpler. A natural characteristic of linkage-type hand exoskeletons is their bidirectional force transmission capability. This attribute confers several advantages, including a wide range of motion, enhanced dexterity, and heightened force output and torque transmission. Furthermore, integrating the actuator directly onto the hand enhances portability and fosters more natural movement.

However, it is worth acknowledging that certain direct linkage transmission gloves may exhibit drawbacks. Some designs could be characterized by substantial weight or bulkiness, potentially causing discomfort for patients. Additionally, achieving an optimal mechanical design that accurately mimics the motion and joint alignment of the human hand can present challenges. Addressing these limitations through careful design considerations and engineering solutions is crucial to realizing the full potential of direct linkage transmission gloves in hand rehabilitation and assistance.

1.2.4 Exoskeleton Glove Control

The variability in hand anatomical structure, compliance, and size, which can be influenced by factors like age and sex, introduces complexities and uncertainties when aiming for precise control in hand exoskeletons. While direct sensing of joint angles or grasping forces has the potential to enhance control accuracy, its implementation necessitates the design and integration of sophisticated sensors, thereby increasing the overall complexity of the system. Consequently, a trade-off exists between the system's control capability and its overall simplicity.

To tackle this challenge, several studies have proposed embedded sensing designs employing commercially available sensors, such as miniature piezoresistive force sensors [33], flex sensors [18, 36], force-sensitive resistors (FSR) [18], optical fibers [37], or specially crafted textile sensors [15, 38]. These sensors are seamlessly integrated into the wearable part of the exoskeleton, enabling direct measurements of joint angles or contact forces.

Most exoskeleton glove designs primarily focus on the mechanical structure, often utilizing passive motion for control purposes. Passive motion involves controlling the hand exoskeleton along a predefined trajectory without considering the user's intentions. This strategy typically employs low-level position or velocity controllers. While passive motion can be used for functional testing or achieving specific states, such as a neutral position for ease of wearing, it finds its most significant application in continuous passive motion (CPM) [39]. CPM, employed in the early stages after injury or surgery, can be effective in preventing stiffness development.

Researchers have also explored the integration of biosignals, such as electroencephalogram (EEG) and surface electromyogram (sEMG), into the control system. These control strategies involve using biological signals measured from the body, like electromyography

(EMG), EEG, or electrooculogram (EOG), to control the exoskeleton. Such strategies hold promise for real-time control of assistive exoskeletal devices, especially for users with impaired motor functioning. The challenge lies in mapping the measured signals to control inputs, as the correspondence between the signals and the controlled degrees of freedom is rarely unambiguous or independent. Biosignal control strategies can involve binary switches [40] or proportional control [41].

Another critical aspect is the implementation of force/torque control. While most of the hand exoskeleton studies reported in [35] focused on position control, a subset of studies integrated force control feedback loops through direct force/torque measurements at linkages, axes, tendons, embedded sensors, or series elastic actuators [18, 42, 43, 44, 45, 46]. Within these studies, grasping demonstrations predominantly utilized simple force control loops, without delving into higher-level control algorithms.

1.3 Problem Statement and Proposed Solution

As an exoskeleton device for ADLs, three major design requirements need to be satisfied [47]. Firstly, the exoskeleton device should feature a compact design to minimize collisions with the environment. This compactness also contributes to a lightweight and comfortable structure. Secondly, the mechanism should be simple to enhance reliability and safety while reducing the size and cost of the exoskeleton devices. Finally, the ergonomics of the human hand exoskeleton, including the remote center of motion and human motion imitation, are crucial for increasing comfort and providing natural hand movements.

Besides the hardware design, the control strategy is also a challenge for wearable rehabilitation devices. Previously, researchers have proven that force control based strategies are more efficient for upper limb rehabilitation devices [48, 49, 50] than position-based control strategies [51]. Traditional model-based force control requires an accurate dynamic model to consider various conditions. However, it is difficult to build an ideal model since many factors, such as backlash, collisions, friction force, and deformation are difficult to model and measure. In contrast, a simplified model would be easier to build, but may ignore important variables resulting in low accuracy.

Due to the various tasks involved in grasping different objects with different shapes and weights, simple force control algorithms may not be sufficient to successfully complete these tasks. Elaborate grasping force control is necessary for precise manipulation in real-world interactions, and it relies on robust sensing capabilities. However, according to a survey, less than half of the surveyed studies demonstrated the implementation of force control in hand exoskeleton systems [35]. This indicates the need for further development and research in this area to improve the effectiveness and applicability of force control algorithms in exoskeleton devices.

Given the challenges of previous wearable devices and control strategies, we propose two generations of exoskeleton glove system that is compact, relatively simple, multi-functional, and user-friendly for grasping based on an accurate force control.

Figure 1.5 shows the prototype of the exoskeleton glove integrated with series elastic actuators (SEAs). It is driven by two types of evolutionary SEAs compared with the previous design [52]. The linkage system couples the motion of the metacarpophalangeal (MCP), proximal interphalangeal (PIP), and distal interphalangeal (DIP) joints into one degree of freedom to greatly simplify the mechanism. It is optimized based on ergonomic factors to provide a comfortable wearing experience for patients and also make up for design deficiencies based on lessons learned from previous research [53]. Besides the basic bending mechanism of each finger, a passive abduction-adduction mechanism has also been implemented. The model-free data-driven force control strategy is integrated and compared against a model-based backlash-compensated force control strategy to achieve a balance between the computation time and accuracy.

To enhance the grasping capabilities of the exoskeleton glove system and improve its interaction with the environment, a vision system has been designed and integrated into the system. The main objective of the vision system is to estimate the weight and shape of the target object, providing valuable information for force planning and control of the exoskeleton glove. In addition, the prototype of the proposed exoskeleton glove system incorporates features such as object slip detection [54] and voice activation [55, 56], further enhancing its functionality and usability.

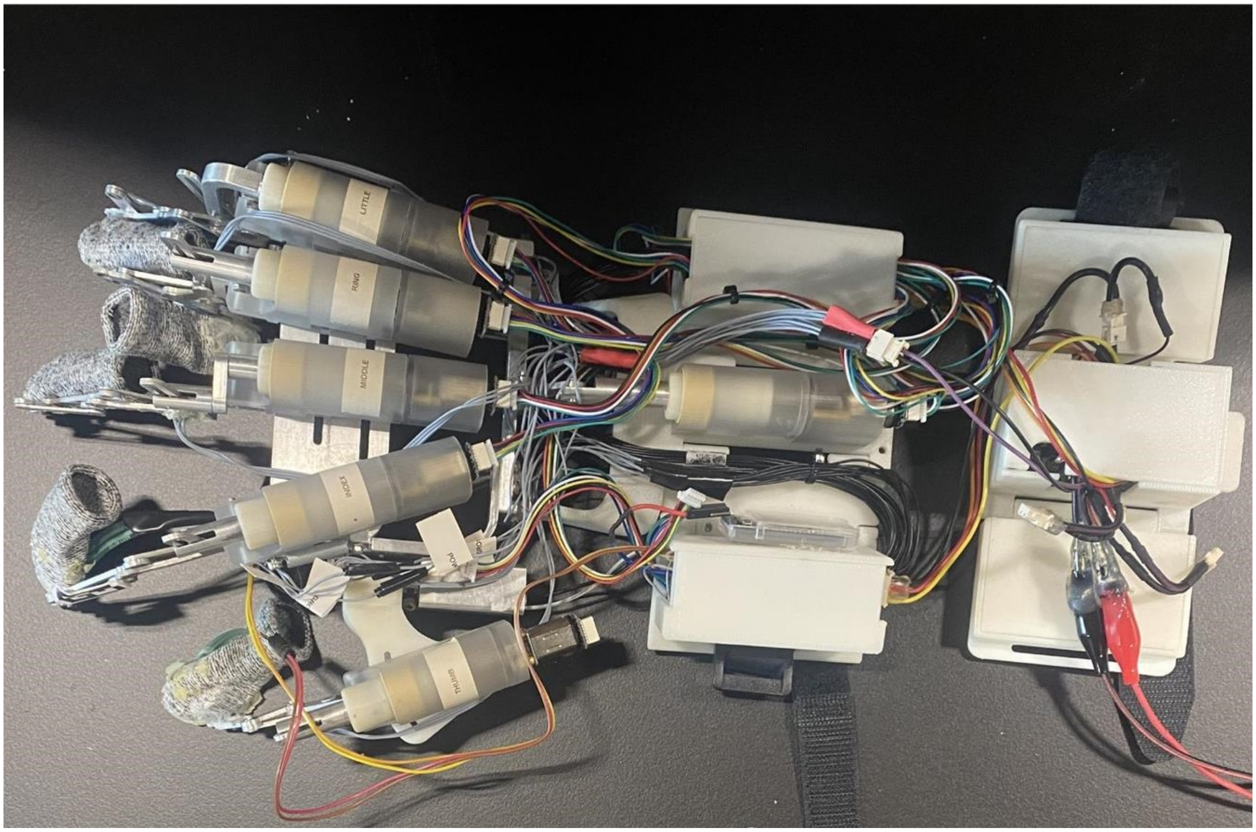

Figure 1.5: Overview of the exoskeleton glove system integrated with series elastic actuators

The unique characteristics of the proposed exoskeleton glove system can be summarized as follows:

1. An integrated system encompassing a linkage mechanism aligned with ergonomic principles, complemented by a human-machine interface facilitated through voice activation.
2. Comprehensive design of the exoskeleton glove system to ensure complete coverage over the entire hand.
3. Implementation of precise force control within the glove system, facilitating intelligent control capabilities.
4. Integration of a vision system to endow the exoskeleton glove with perceptual abilities.

These, along with other improvements implemented based on previous research[52, 57, 58] make our proposed glove system portable, lightweight, and much more capable than before.

To further improve the performance of the robotic gloves in terms of wearability, comfortability, and portability, we propose the exoskeleton glove system (Fig. 1.6) designed with new mechanism and integrated with reinforcement learning-based force planning for autonomous grasping, that is compact, low-profile, portable, and functional for ADLs for patients by considering both the general requirements of hand exoskeleton devices and the shortcomings of existing wearable devices.

In our innovative design, each finger linkage is actuated by a customized linear actuator. The motion of each finger exoskeleton is coupled by using a rigid coupling hybrid mechanism (RCHM) to reduce the number of degrees of freedom and improving overall functionality. To ensure a natural and comfortable user experience, we have carefully synthesized the mechanism to closely imitate the natural motion of the human hand. This approach improves

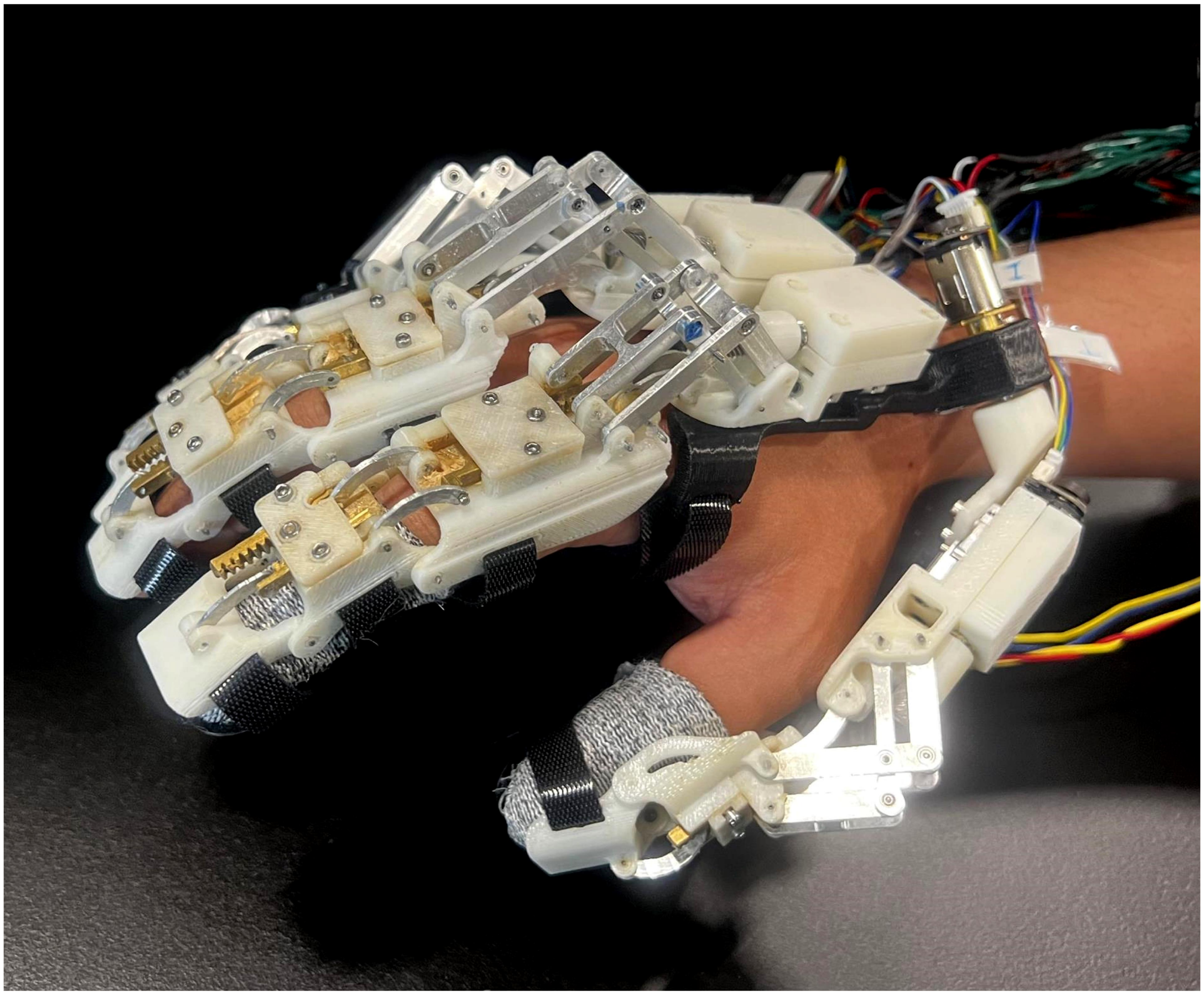

Figure 1.6: The prototype of the novel low-profile exoskeleton glove, designed with a focus on enhanced wearability and comfortability by further reducing size and weight.

wearability and comfortability, allowing users to perform various ADLs easily. Furthermore, the compact and low-profile design of the exoskeleton glove enhances its portability, allowing users to wear it comfortably in different environments.

To enhance the versatility of the glove, a reinforcement-learning-based force control policy is integrated into the control system. The exoskeleton glove is imported into a predefined simulation environment for training. The training process is focused on generating a self-adjusting control policy tailored for grasping tasks encompassing five distinct object types, each associated with widely utilized grasp types for activities of daily living. During each training episode, a target object is randomly chosen from the predefined object types, with its size and weight parameters also randomly selected within specified constraints. Comprehensive fine-tuning of environment parameters and component attributes is undertaken to closely replicate real-world conditions.

Furthermore, an additional data analysis step is executed to bridge the disparity between the simulation environment and the physical world. Through this approach, the glove gains the capability to adeptly address diverse grasping tasks by autonomously adapting the applied forces.

The unique characteristics of the proposed novel low-profile exoskeleton glove system can be summarized as follows:

1. Incorporation of a novel finger linkage mechanism tailored for constructing a low-profile exoskeleton glove, emphasizing customized optimization to enhance wearability and comfortability.
2. Encompassing design of the exoskeleton glove system, ensuring comprehensive coverage over the entire hand.
3. Integration of a reinforcement-learning-based self-adjustable force control policy within

the glove system, enhancing its capacity to grasp a variety of objects pertinent to daily activities.

1.4 Dissertation Structure

The structure of this dissertation is outlined as follows:

Chapter 1 introduces the research context, motivation, literature review, problem statement and proposed solutions. It provides an overview of the dissertation's structure by summarizing the content of each subsequent chapter.

Chapter 2 delves into the mechanical design, kinematic analysis, and synthesis of the finger linkage mechanism for the exoskeleton glove with series elastic actuators. It explores the development of series elastic actuators, hardware components, and force control strategies for the exoskeleton glove. The impact of factors like backlash and friction force is investigated and mitigated by building the mathematical model. The chapter also introduces a novel model-free data-driven force predictive control method and compares it with traditional model-based approaches using various experimental evaluations. The amount of experiments on healthy subjects and clinical experiments with patients are also presented.

Chapter 3 focuses on the mechanical design, kinematic analysis, and kinematic synthesis of the novel low-profile exoskeleton glove. The primary aim is to achieve a reduction in size and weight while retaining functionality. Detailed insight into the mechanism of this iteration is provided.

Chapter 4 delves into the application of deep reinforcement learning (DRL) methods for various grasp tasks. It discusses the simulation environment, force planning algorithms, and the challenges associated with transitioning from simulation to the real world. Extensive experiments are conducted to assess the effectiveness of the DRL-based approach.

Chapter 5 offers a comprehensive summary of the research's major contributions. It outlines the significant findings and insights derived from the study, and provides a roadmap for potential future research directions.

1.5 List of Contributions

The major contributions of this research are summarized as follows:

1. Mechanical design, kinematic analysis and kinematic synthesis for the finger linkage of two generation exoskeleton gloves.

2. Design and development of the linear series elastic actuator and rotary series elastic actuator.

3. Development and realization of the two generations of exoskeleton gloves system.

4. Dynamic modeling and analysis of the exoskeleton gloves.

5. Proposal and implementation of backlash estimation and friction force compensation for the exoskeleton glove with series elastic actuators.

6. Proposal of the model-free data-driven force predictive control method for the exoskeleton glove with series elastic actuators.

7. Creation of a simulation environment for the novel low-profile exoskeleton glove.

8. Conducting clinical experiments on human subjects using the exoskeleton glove with series elastic actuators.

9. Building the simulation environment and implementation of the deep reinforcement-learning based force planning for autonomous grasping

1.6 Selected Publications

Disclosure: Part of the content of this dissertation uses materials directly adapted from the following peer-refereed journal publications and conference proceedings. The authorization from the publication presses of using these materials in this dissertation are provided as supplementary material.

Peer-Reviewed Journal Paper

1. Xu, W., Guo, Y., Bravo, C., Ben-Tzvi, P., ”Design, Control, and Experimental Evaluation of a Novel Robotic Glove System for Patients with Brachial Plexus Injuries”, IEEE Transactions on Robotics, vol. 39, no. 2, pp. 1637-1652, April 2023.

2. Xu, W., Guo, Y., Ben-Tzvi, P., “Vision Based Human Machine Interface for a Rehabilitation Robotic Exoskeleton Glove” Autonomous Robots, August 2023, Under review.

3. Xu, W., Guo, Y., Ben-Tzvi, P., “Development of A Novel Compact Exoskeleton Glove with Reinforcement Learning Control” Journal of Mechanisms and Robotics, Transactions of the ASME, May 2023, Under review.

4. Guo, Y., Xu, W., Pradhan, S., Bravo, C.J., Ben-Tzvi, P., “Data Driven Calibration and Control for Compact Lightweight Series Elastic Actuators for Robotic Exoskeleton Gloves”, IEEE Sensors Journal, Vol. 21, Issue 19, pp. 21120-21130, October 2021.

   * Selected as a featured article.

5. Guo, Y., Xu, W., Pradhan, S., Bravo, C.J., Ben-Tzvi, P., “Personalized Voice Activated Grasping System for a Robotic Exoskeleton Glove”, Mechatronics Journal, Vol. 83, pp. 102745:1-12, May 2022.

Peer-Reviewed Conference Paper

1. Xu, W., Guo, Y., Bravo, C., Ben-Tzvi, P., “Robotic Exoskeleton Glove System Design and Simulation for Patients with Brachial Plexus Injuries”, Proceedings of the 2023 ASME IDETC/CIE, 47th Mechanisms & Robotics Conference, Boston, MA, August 20-23, 2023.

2. Xu, W., Liu, Y., Ben-Tzvi, P., ” Development of a Novel Low-profile Robotic Exoskeleton Glove for Patients with Brachial Plexus Injuries”, Proceedings of the 2022 IEEE International Conference on Intelligent Robots and Systems (IROS 2022), Kyoto, Japan, Oct. 23-27, 2022.

3. Xu, W., Guo, Y., Bravo, C., Ben-Tzvi, P., ”Development and Experimental Evaluation of a Novel Portable Haptic Robotic Exoskeleton Glove System for Patients with Brachial Plexus Injuries”, Proceedings of the 2022 IEEE International Conference on Intelligent Robots and Systems (IROS 2022), Kyoto, Japan, Oct. 23-27, 2022.

4. Xu, W., Liu, Y., Bravo, C., Ben-Tzvi, P., ”Design, Analysis, and Prototyping of a Novel Single DOF Index Finger Exoskeleton Mechanism”, Proceedings of the 2022 ASME IDETC/CIE, 46th Mechanisms & Robotics Conference, St. Louis, MO, Aug. 16-19, 2022.

5. Xu, W., Pradhan, S., Guo, Y., Bravo, C.J., Ben-Tzvi, P., ”A Novel Design of a Robotic Glove System for Patients With Brachial Plexus Injuries.” Proceedings of the ASME

2020 International Design Engineering Technical Conferences and Computers and Information in Engineering Conference. Volume 10: 44th Mechanisms and Robotics Conference (MR). August 17–19, 2020.

6. Guo, Y., Xu, W., Pradhan, S., Bravo, C.J., Ben-Tzvi, P., ”Integrated and Configurable Voice Activation and Speaker Verification System for a Robotic Exoskeleton Glove.” Proceedings of the ASME 2020 International Design Engineering Technical Conferences and Computers and Information in Engineering Conference. Volume 10: 44th Mechanisms and Robotics Conference (MR). August 17–19, 2020.
7. Guo, Y., Xu, W., Bravo, C., Ben-Tzvi, P., “Voice-based Human Machine Interface for Rehabilitation Exoskeleton Robotic Glove with Speaker Verification Feature Using One-shot Learning”, Proceedings of the 2024 IEEE International Conference on Robotics and Automation (ICRA2024), Yokohama, JAPAN, May 23-27, 2024, Submitted.

Patents

Xu, W., Ben-Tzvi, P., Refour, E., Sebastian, B., Pradhan, S., Guo, Y., “Robotic Exoskeleton Glove System”, U.S. Patent Application No. 16/888,993, Filed June 1, 2020. (to be issued).

Chapter 2

Modeling and Control of the Exoskeleton Glove with Series Elastic Actuator

2.1 Introduction

Given the challenges of previous wearable devices and control strategies that discussed in Chapter 1, we propose a new exoskeleton glove with Series Elastic Actuators that is compact, relatively simple, multi-functional, and user-friendly for grasping based on an accurate model-free force control. This chapter presents the design details, optimization, control, and development of the proposed exoskeleton glove system (Fig. 2.1). The glove is driven by two types of evolutionary SEAs compared with the previous design [52]. The linkage system couples the motion of the metacarpophalangeal (MCP), proximal interphalangeal (PIP), and distal interphalangeal (DIP) joints into one degree of freedom to greatly simplify the mechanism. It is optimized based on ergonomic factors to provide a comfortable wearing experience for patients and also make up for design deficiencies based on lessons learned from previous research [53]. Besides the basic bending mechanism of each finger, a passive abduction-adduction mechanism has also been implemented. The model-free data-driven force control strategy is presented and compared against a model-based backlash-compensated force con-

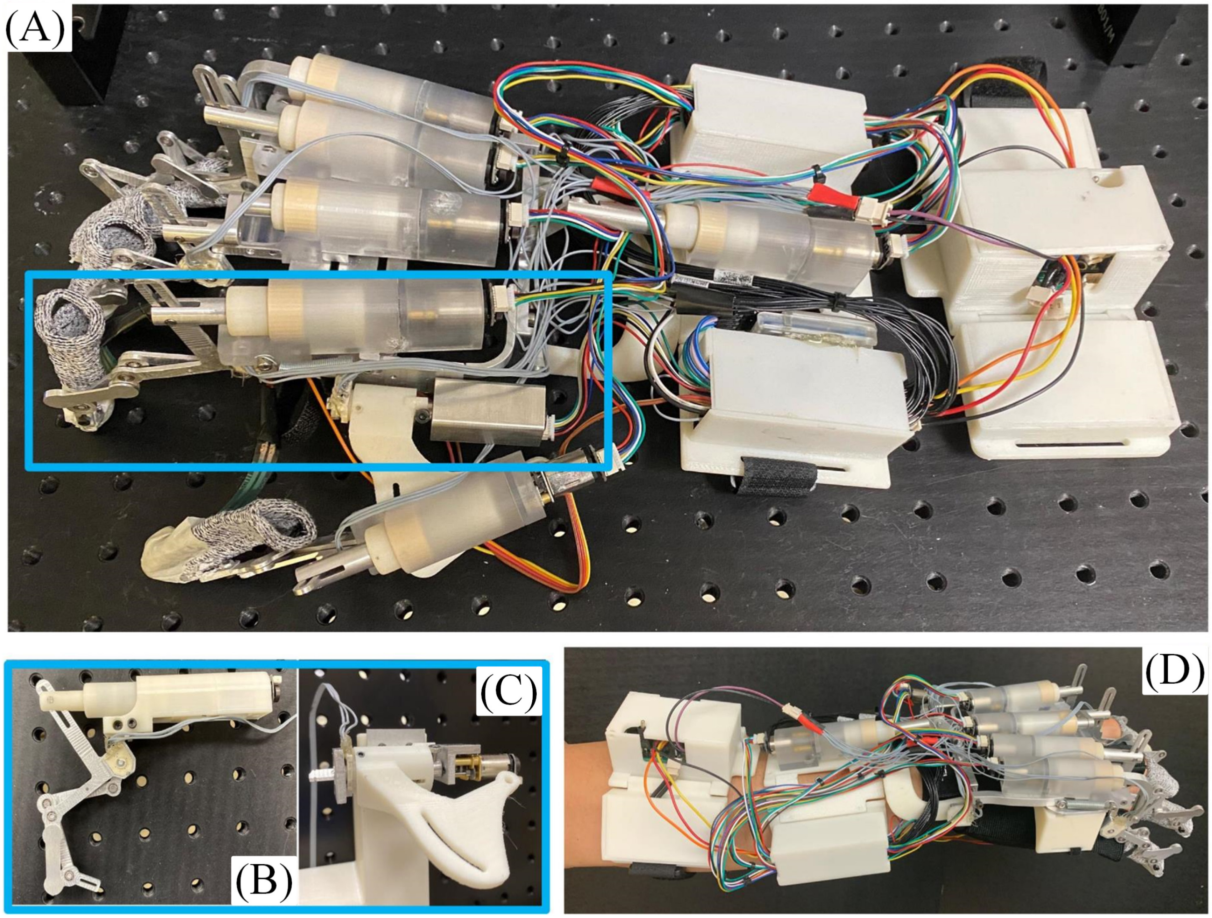

Figure 2.1: (A) Overview of the exoskeleton glove system, (B) index finger linear Series Elastic Actuators (SEA), (C) rotary SEA, (D) user wearing the exoskeleton glove. Blue – enlarged view of index finger linear SEA and rotary SEA.

trol strategy to achieve a balance between the computation time and accuracy. Finally, a prototype of the proposed exoskeleton glove system [59] with integrated object slip detection [54] and voice activation [55, 56] was developed.

The unique characteristics of the proposed exoskeleton glove system can be summarized as follows:

1. an integrated system that contains a linkage mechanism that satisfies ergonomics and includes a human-machine interface through voice activation;

2. the exoskeleton glove system was designed to fit over the entire hand;
3. the glove system is implemented with model-free data-driven accurate force control, which provides the feasibility for intelligent control.
4. the slip detection is implemented to enable real-time adjustments of grasping force.

These, along with other improvements implemented based on previous research[52, 57, 58] make our proposed glove system portable, lightweight, and much more capable than before.

2.2 Exoskeleton Finger Mechanism Design

The goal of the exoskeleton finger mechanism design is to build a compact finger linkage that can imitate the human finger grasping motion while maximizing the workspace of each finger. Each human finger consists of 3 different joints, including the MCP joint, the PIP joint, and the DIP joint (shown in Fig. 2.2). The DIP and PIP joints have one flexion-extension DOF, but the MCP joint has one more abduction-adduction DOF. The thumb digit consists of interphalangeal (IP), MCP, and Carpometacarpal (CMC) joints. Similarly, the IP and MCP joints have one DOF (flexion–extension), but the CMC has two DOFs, including flexion–extension and abduction-adduction [60].

Previous research [61, 62, 63] has proven that a finger linkage with reduced DOFs can achieve most of the grasping motions needed for ADLs because of the coupled motion of different joints on each finger while grasping. Furthermore, an exoskeleton finger linkage with reduced DOFs requires fewer actuators for grasping, which results in a more compact design. To overcome the problems mentioned in Sec. 1.3 and achieve the design goals proposed above, the coupling mechanism is adopted and attached to the side of each finger.

This allows the entire exoskeleton to be more slim and more lightweight with respect to the existing design. Fig. 2.2 shows an example of the proposed mechanism. The joints of each exoskeleton finger mechanism are coincident with the joints of the human finger. It is worth mentioning that the MCP joint of the middle and ring fingers on the exoskeleton are placed forward of the human counterparts to avoid interference with the finger-webs. The blue, green, and orange links shown in Fig. 2.2 represent the Distal phalanx, Intermediate phalanx and Proximal phalanx, respectively. The adjacent links are connected at their extensions by constraint links (brown links) for coupling the motion. Therefore, the three DOFs for the flexion-extension motion are reduced to one DOF flexion-extension motion for each finger. The rotations of the first two joints on the thumb are coupled by the same method.

The abduction-adduction motion is also important for stable and comfortable grasping [64]. The web between fingers and the interossei muscles help to perform the adduction motion during the process of closing the hand. The proposed exoskeleton glove implements a passive abduction-adduction mechanism as shown in Fig. 2.3. A revolute joint is added at the bottom of the SEA to connect the base and the housing (partial view in Fig. 2.3). A soft spring on the side is used to connect the housing of the SEA and the base for abduction motion while opening the hand. A mechanical limit is added to restrict the maximum angle and prevent over-rotation. When the patient's hand opens, the spring will pull the finger to one side until it reachs the mechanical limit to achieve abduction motion and hold the position. When the patient's hand closes, the internal mechanism of the human finger mentioned above will force the hand to perform adduction motion.

For most ADLs, the weight of the goal object is unknown. Therefore, pre-defining a specific grasp force for each object is unrealistic. Thus, it is necessary to integrate a slip detection function. Previous researches [56, 65] have shown that sensor fusion can help with

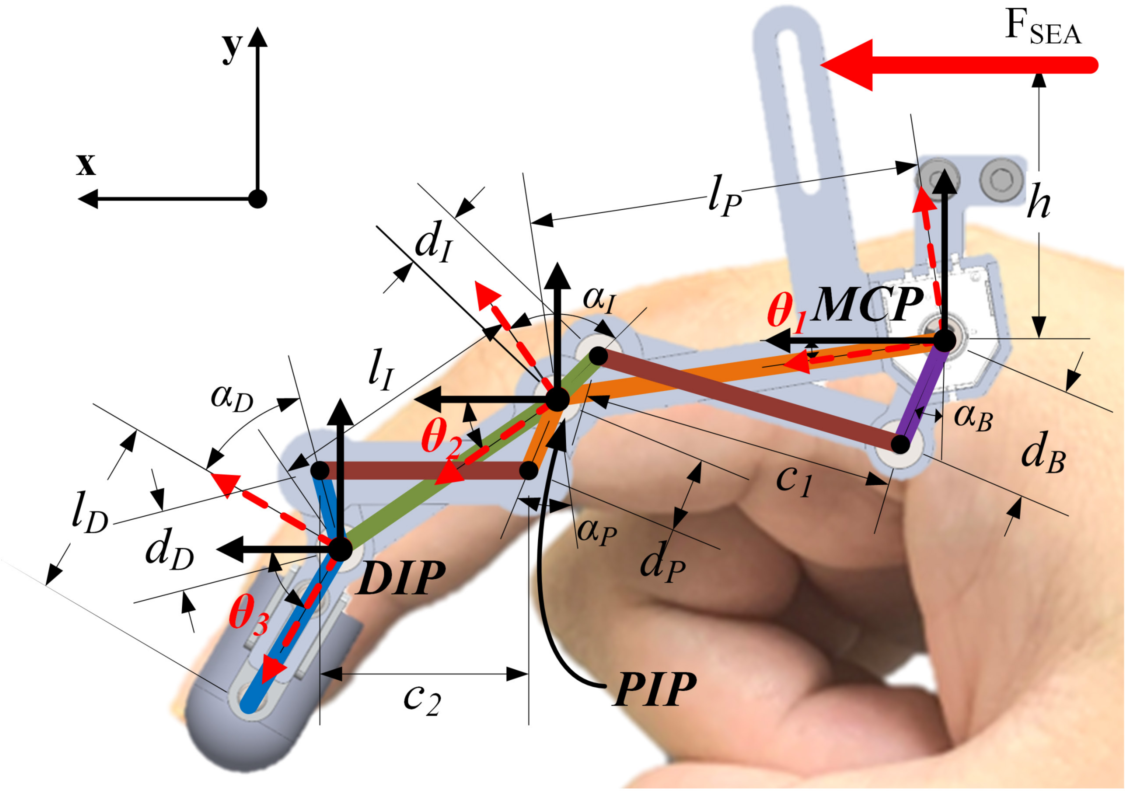

Figure 2.2: Mechanism schematic and kinematic model of the index exoskeleton finger linkage. Different colors represent different links: Blue link – Distal phalanx, Green link – Intermediate phalanx, Orange link – Proximal phalanx, Brown links – constraint links.

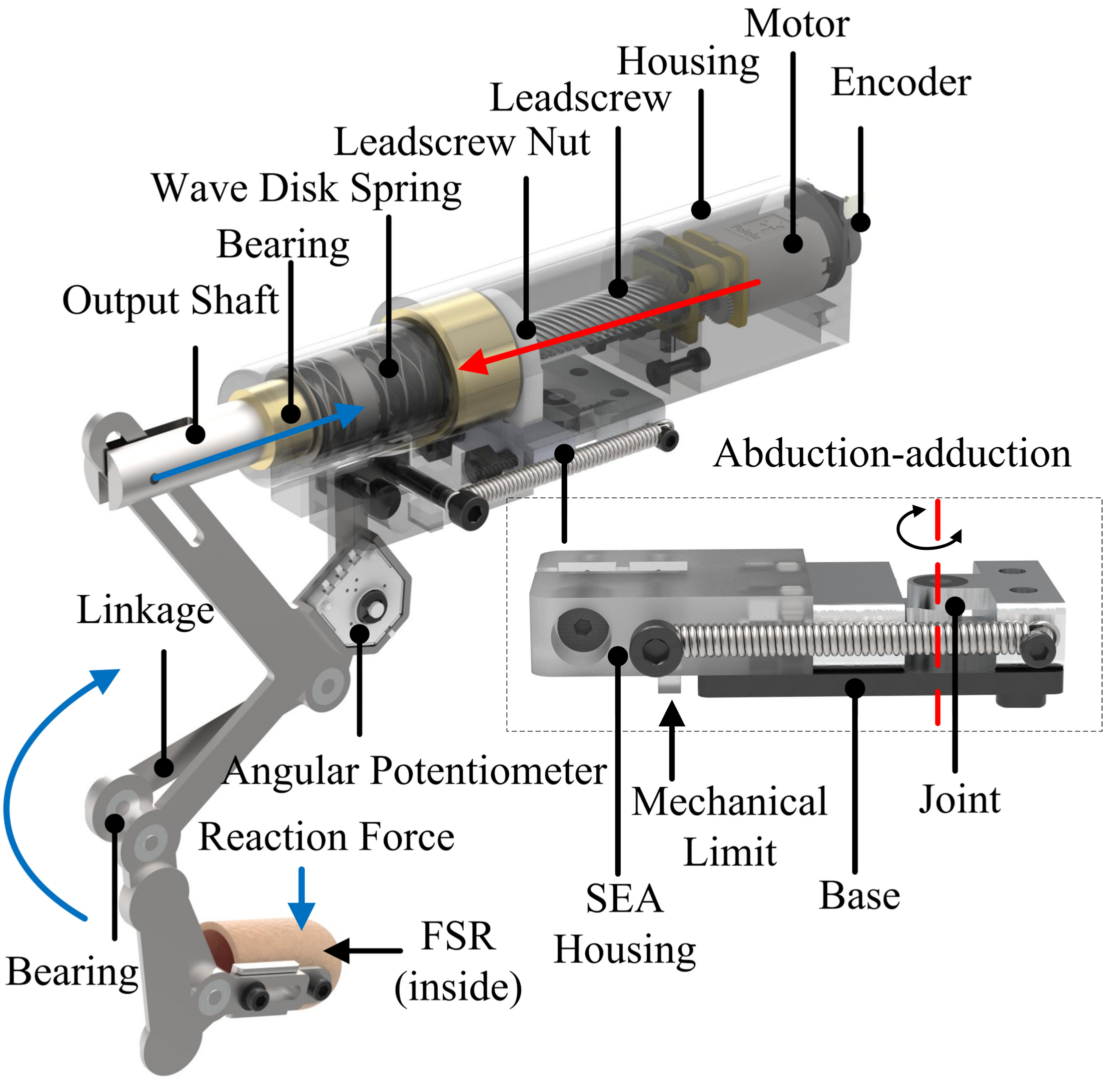

Figure 2.3: Perspective View of the index linkage. The screw nut guided by leadscrew connects to the output shaft. The compressed wave disk spring between the output shaft and screw nut measures the force by its deformation when the fingertip makes contact with an object. The red arrow shows the force generation flow and the blue arrow shows the force measurement flow. The distal link is adjustable and can be extended by 7mm. The LSEA can slide on the base to accommodate different hand size. The partial view shows the details of the abduction-adduction mechanism. It is implemented at the bottom of the SEA to connect the finger linkage with the base through a joint. At the initial position, the hand needs to be open and be ready for grasping. The spring on the side pulls the exoskeleton finger linkage to the side to perform the abduction. Mechanical limits were added to avoid excess force to the fingers. The palmar interossei muscle group will perform the adduction automatically and stretch the spring while grasping.

slip detection. This method is implemented by attaching force-sensing resistor (FSR) sensors on the fingertip of the thumb and index finger of the exoskeleton. The control logic used in our exoskeleton is based on a slip-grasp policy. Upon receiving a voice command, the SEAs will first apply a predefined force to ensure the exoskeleton made contact with the object. The FSRs are used to verify that the object has contact with either index or thumb fingers. The slip detection is activated after the initial force has been applied. The changes of FSRs and SEAs readings are monitored. If either FSRs or SEAs measured a drop in force for more than 5%, 2N force will be added incrementally to all fingers. The FSR sensors only work for contact detection and slip detection but not for force measurement due to their high sensitivity and low linearity.

2.3 Kinematic Analyses and Synthesis

In order to optimize the finger mechanism design presented above, the kinematics of the mechanism needs to be modeled. The kinematic model used in previous research [53] did not consider the trajectory limitation of the human hand. In this research, the index exoskeleton finger linkage is selected for illustration purposes. Assuming that the origin of the global coordinate frame is located at the MCP joint as shown in Fig. 2.2, the open-loop equation for the kinematic chain of the finger exoskeleton linkage is given by Eqn. 2.1,

$$l_P e^{\theta_1 i} + l_I e^{\theta_2 i} + l_D e^{\theta_3 i} = x_{tip} + y_{tip} i \tag{2.1}$$

where l_1, l_2 and l_3 are the lengths of the Proximal link, Intermediate link, and Distal link of the exoskeleton, respectively. θ_1, θ_2 and θ_3 are the angles between the corresponding link and the x-axis. (x_{tip}, y_{tip}) represents the fingertip coordinate in the global frame of reference.

Forward kinematics is used for evaluating the angles θ_1, θ_2 and θ_3. The relationship between them is formed by adding constraint links to couple their motion. The constraints can be expressed as Eqn. 2.2 and Eqn. 2.3,

$$\begin{aligned} c_1^2 =& [l_P \cos\theta_1 - d_I \sin(\alpha_I - \theta_2) - d_B \sin\alpha_B]^2 \\ &+ [l_P \sin\theta_1 - d_I \cos(\alpha_I - \theta_2) - d_B \cos\alpha_B]^2 \end{aligned} \tag{2.2}$$

$$\begin{aligned} c_2^2 =& [l_I \cos\theta_2 + d_D \sin(\theta_3 - \alpha_D) - d_P \sin(\alpha_P - \theta_1)]^2 \\ &+ [l_I \sin\theta_2 - d_D \cos(\theta_3 - \alpha_D) - d_P \cos(\alpha_P - \theta_1)]^2 \end{aligned} \tag{2.3}$$

where c_1 and c_2 are the lengths of the corresponding constraint links. d_B, d_P, d_I and d_D are the extension lengths of the base, Proximal link, Intermediate link and Distal link to be connected with the constraint links, respectively. α_B, α_P, α_I and α_D are the angles of extension of the base, Proximal link, Intermediate link, and Distal link with respect to the y-axis of the local coordinates (only acute angles), respectively.

Because θ_1 is driven by the actuator directly, given a particular θ_1, the unique corresponding θ_2 and θ_3 can be derived based on the above constraint equations. Analytically, θ_2 and θ_3 can be expressed as Eqn. 2.4 and Eqn. 2.5,

$$\begin{aligned} \theta_2 =& -\tan^{-1}\left\{ \frac{\sqrt{-[A + (c_1 - d_I)^2][A + (c_1 + d_I)^2]}}{-c_1^2 - A + B + d_I^2} - \right. \\ & \left. \frac{2 d_I l_P \cos\theta_1 - 2 d_B d_I \sin\alpha_B}{-c_1^2 - A + B + d_I^2} \right\} + \alpha_I \end{aligned} \tag{2.4}$$

where,

$$A = 2d_B l_P \sin(\alpha_B + \theta_1) - l_P^2 - d_B^2 \tag{2.5}$$

$$B = 2d_I l_D \sin\theta_1 - 2d_B d_I \cos\alpha_B \tag{2.6}$$

$$\begin{split}\theta_3 = \tan^{-1}\Bigg\{ & \frac{\sqrt{-[C + (c_2 - d_D)^2][C + (c_2 + d_D)^2]}}{-c_2^2 - C + D + d_D^2} \\ & - \frac{2d_D l_I \cos\theta_2 - 2d_P d_D \sin(\alpha_P - \theta_1)}{-c_2^2 - C + D + d_D^2}\Bigg\} + \alpha_D\end{split} \tag{2.7}$$

where,

$$C = 2d_P l_I \sin(\alpha_P - \theta_1 + \theta_2) - l_I^2 - d_P^2 \tag{2.8}$$

$$D = -2d_D d_P \cos(\alpha_P - \theta_1) + 2d_D l_I \sin\theta_2 \tag{2.9}$$

.

The Jacobian of the mechanism is calculated to evaluate the velocity kinematics. Numerical computation in MATLAB is used to evaluate the Jacobian of the system. The velocity of the endpoints of the exoskeleton linkages in the global x and y directions can be expressed as Eqn. 2.10,

$$[\dot{\mathbf{p}}]_{2\times1} = [\mathbf{J}]_{2\times1}[\dot{\boldsymbol{\theta}}_1]_{1\times1} \tag{2.10}$$

The geometric parameters of each link, especially the joints' position and the length of the constraint links, determine the properties of the linkage such as workspace and force transmission ratio. The optimization process is used to find the values for the design variables that minimize the objective function, which are related to the properties of the linkage, while satisfying the constraints. Considering the passive abduction-adduction mechanism, each exoskeleton finger mechanism is optimized in 2D space separately.

Based on the analysis of the kinematics model, all of the parameters except for l_P, l_I, l_D, and θ_1, are design variables for each specific exoskeleton finger. To build a more general exoskeleton glove that is suitable for most people, the values of l_P, l_I, and l_D for each linkage are determined by considering the results of the previous research [66], which provides the range of length of the finger phalanges, and the measurement results of the user's hand. The final selected values are shown in Table 2.1.

Table 2.1: Links Length of Each Finger

Finger Name	l_P (mm)	l_I (mm)	l_D (mm)
Index	42	25	17,7
Middle	47	28.3	17.4
Ring	43	26.2	17.3
Little	31.3	20.5	16
Thumb	32	-	22

To be better able to imitate a human hand's grasp motion, the optimization takes the coincidence of the fingertips, the PIP joint positions, and the DIP joint positions into account. The rotation angles of each joint on the grasping trajectory are obtained from the HUST dataset [67]. The dataset provides broadly 33 types of grasps with respect to 30 subjects. The data from Grasp 2 of Subject 24, which performs a small diameter grasp, is selected as a reference trajectory due to its large bending angles. Four points, which are equally distributed on the reference trajectory, are selected as reference points. It is worth mentioning that θ_1 is selected by mapping rotation angles of the MCP joint into $0^\circ \sim 40^\circ$ because of the rotation limitation of each exoskeleton finger mechanism. The objective function Z is the sum of the distance between endpoints, the distance between DIP joints, and the distance between PIP joints on four reference points with different weights. It can be expressed as Eqn. 2.11,

$$Z = \sum_{i=1}^{3} \mathbf{w}_i^T \mathbf{e}_i \tag{2.11}$$

where $[\mathbf{w_1}]_{4\times1}$ represents the weights of endpoints with respect to each reference point, $[\mathbf{w_2}]_{4\times1}$ represents the weights of the DIP joints with respect to each reference point, $[\mathbf{w_3}]_{4\times1}$ represents the weights of the PIP joints with respect to each reference point, $[\mathbf{e_1}]_{4\times1}$ represents the distances of endpoints with respect to each reference point, $[\mathbf{e_2}]_{4\times1}$ represents the distances of the DIP joints with respect to each reference point, and $[\mathbf{e_3}]_{4\times1}$ represents the distances of the PIP joints with respect to each reference point. Fig. 2.4 shows the index finger joints trajectory with different values of the MCP rotation angle. The angle varies from 5° to 35° and leaves 5° to reach the limitation for safety.

Considering the need to avoid interference between the finger-webs and the finger linkages, the exoskeleton MCP joints for the ring and middle fingers were offset forward and upward with respect to the corresponding finger's MCP joint. The offset of the MCP joint between the exoskeleton and the human finger are also design variables to be optimized with inequality constraints. The trajectory for a small-diameter cylindrical grasp with the optimized exoskeleton glove is shown in Fig. 2.5.

To have a better grasp performance, the impact of the coupled wrist motion is also considered since the hand impairments also result in the wrist impairments. An LSEA is used to connect the wrist and the glove to help patients hold the initial position of the hand for grasping. The LSEA on the wrist will be automatically adjusted to maintain the initial

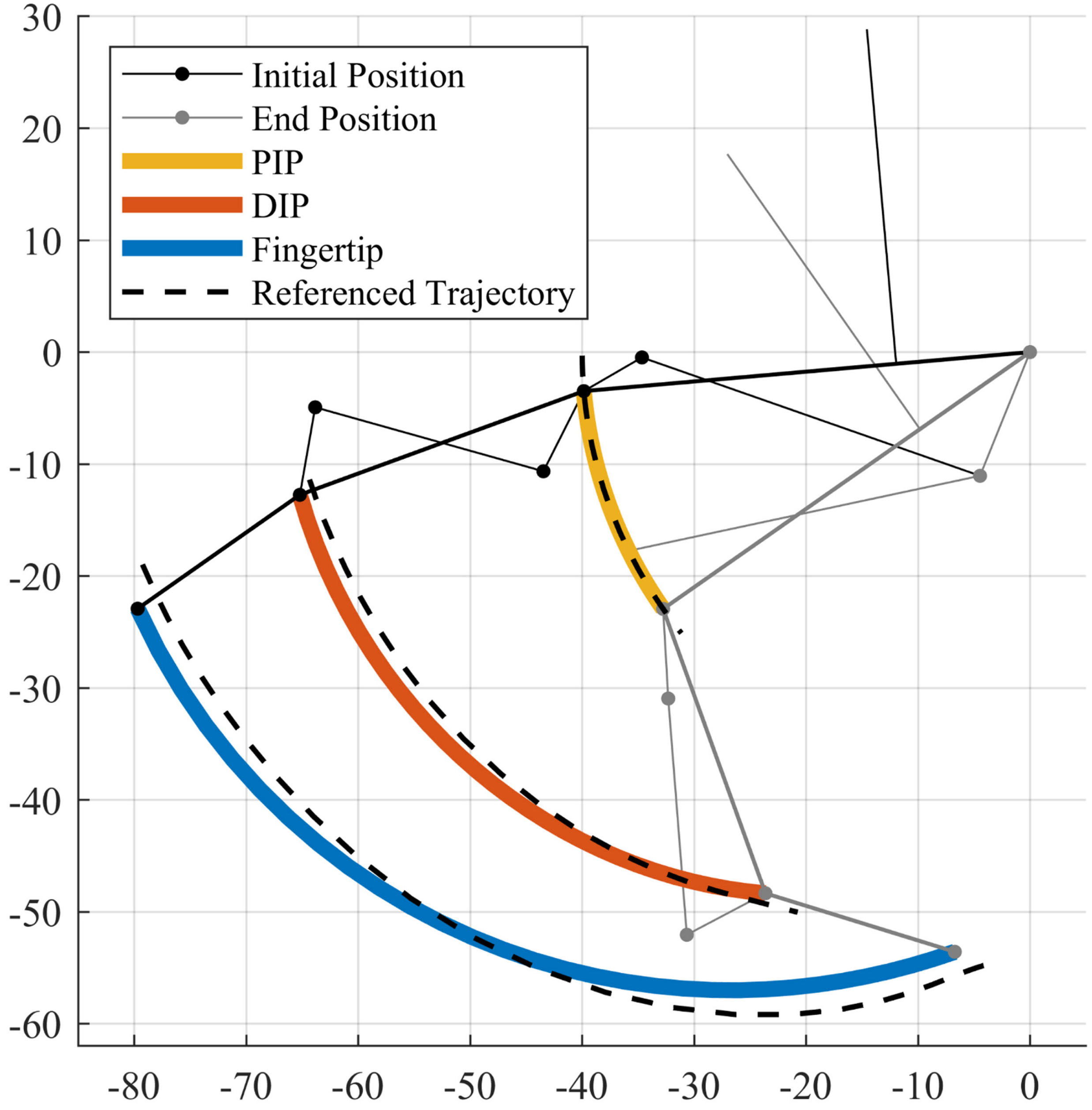

Figure 2.4: Kinematic simulation of the optimized index finger exoskeleton rotating around the MCP joint from 5° to 35°. The trajectories of the PIP joint, DIP joint, and fingertip are shown. The referenced trajectories, which are based on the referenced joint angle with a selected finger length, are also shown for comparison.

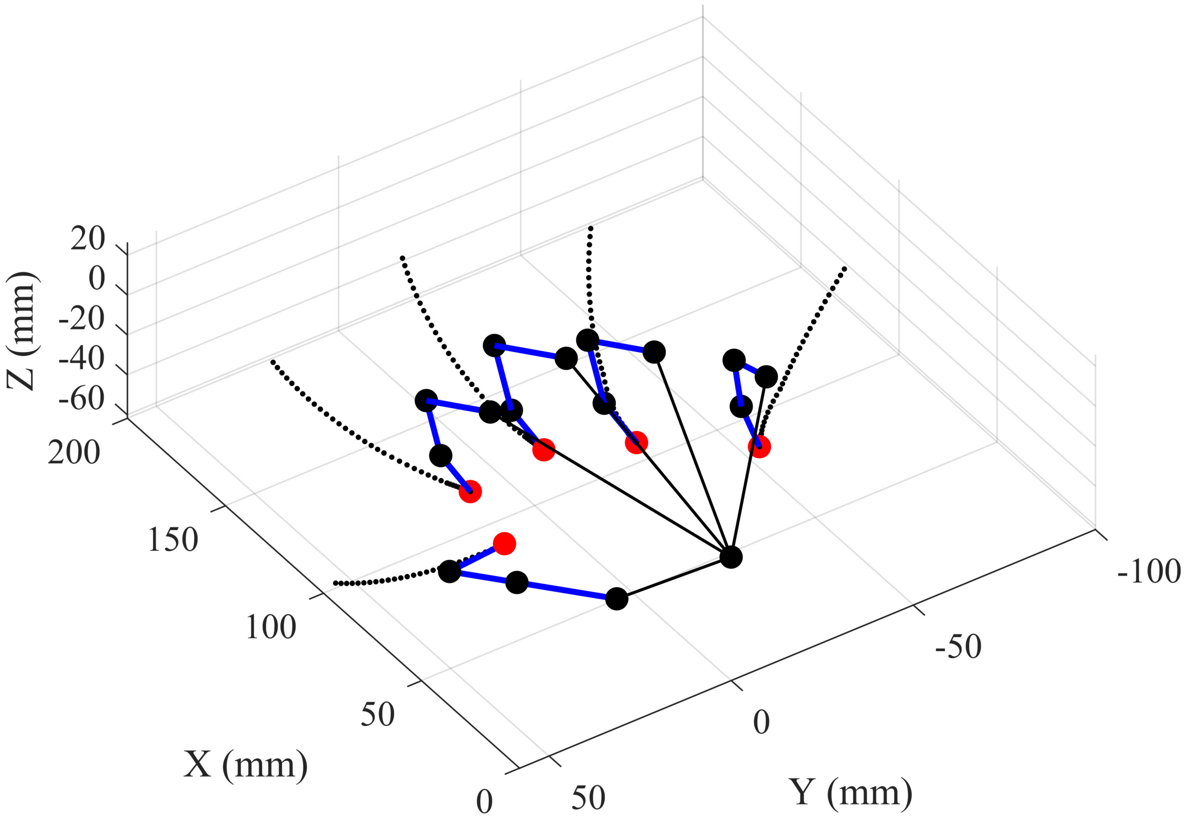

Figure 2.5: Simulation of a small diameter cylindrical grasp with optimized finger linkages. The blue bars represent the exoskeleton links. The black dots represent the exoskeleton joints. The red dots represent the endpoints of each linkage. The dotted lines represent the trajectories of the fingers' motion.

position smoothly. It is worth mentioning that only the flexion and extension is considered since these movements are commonly used for our selected grasp types mentioned in Sec. 2.7.

2.4 Series Elastic Actuator

To achieve accurate and stable force control, comfortable wearability, and safe human-robot interaction, Series Elastic Actuators (SEAs) [68] were incorporated into our proposed glove design. The SEAs do not only act as force actuators or force sensors, but also as compliant elements to introduce pliability and to avoid injury to the user. Two types of SEAs were designed, including Linear SEA (LSEA) and Rotary SEA (RSEA).

2.4.1 Linear Series Elastic Actuator

The LSEAs are used to provide and measure forces for the five fingers and wrist. The perspective view in Fig. 2.6 shows the components of the LSEA. The wave disk springs are used as elastic elements because of their lower operating height and their ability to transmit 100% of the axial load. It is worth mentioning that the leadscrew nut, two wave disk springs, and the output shaft are firmly connected and move as one slider on the leadscrew, powered by a motor mounted at the end. In this design, only the back spring works as the elastic element for the LSEA, and the front one works as a buffer to avoid harm from sudden force application. The output motor torque is transmitted to an output force through a gearbox, leadscrew, and wave disk spring. Considering the following leadscrew load-lifting calculation by Eqn. 2.12 and Eqn. 2.13,

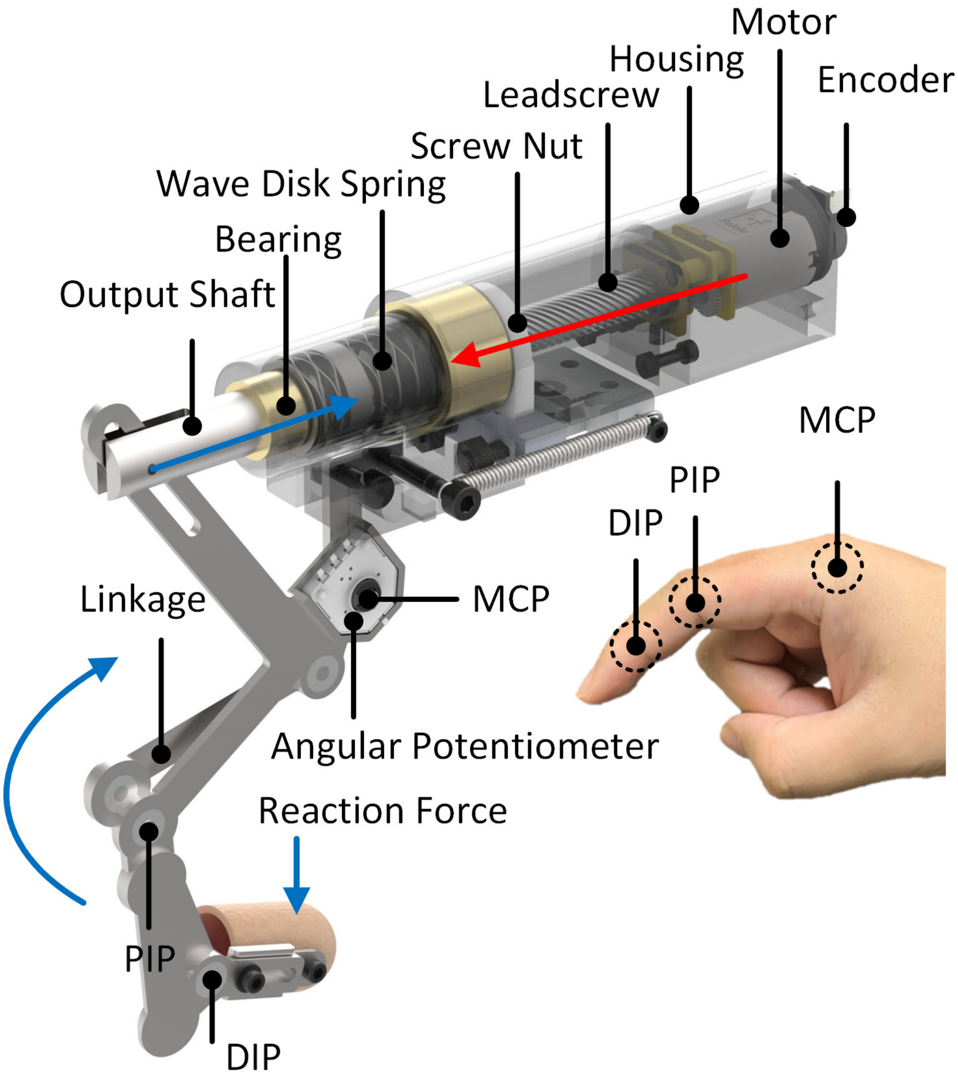

Figure 2.6: Perspective View of the Linear SEA. Working principle of the Linear SEA: the screw nut guided by leadscrew connects the output shaft. The spring between the output shaft and screw nut is compressed when there is contact with an object and measures the force by its deformation at the same time.

$$\tan(\lambda) = \frac{l}{\pi d_m} \tag{2.12}$$

$$F_{raise} = \frac{2T}{d_m}\eta_s(\frac{1 - \mu \sec\alpha \tan\lambda}{\mu \sec\alpha + \tan\lambda}) \tag{2.13}$$

the output force F_o and speed v_o at the SEA output shaft, related to the input torque T_m and speed n_m from the motor, can be calculated according to Eqn. 2.14 and Eqn. 2.15:

$$F_o = \frac{2T_m i}{d_m}\left(\frac{1 - \mu \sec\alpha \tan\lambda}{\mu \sec\alpha + \tan\lambda}\right)\eta_s\eta_g\eta_m \tag{2.14}$$

$$v_o = \frac{l n_m}{60i} \tag{2.15}$$

where l is the lead of the leadscrew; d_m is the pitch diameter; λ is the lead angle; α is the thread angle; μ is the friction coefficient; i is the reduction rate; η_s is the efficiency of the leadscrew; η_g is the transmission efficiency; and η_m is the efficiency of the motor combination. The transmission efficiency is defined as the ratio of the output force and the input force.

The above equations specify the largest force that can be generated by the LSEA. However, the measurable forces (F_{SEA}) are determined by the displacement of elastic elements. For the LSEA, it is hard to measure the displacement of elastic elements inside the LSEA directly. Thus, the displacement measurement (Δs) of the wave disk spring is performed by calculating the relationship between the readings from the potentiometer (θ, initial angle θ_i) on the linkage and the motor encoder ($\Delta ticks$, compared with the initial position), as shown in Eqn. 2.16,

$$F_{SEA} = k\Delta s = k\left[\frac{l\Delta ticks}{N_{cpr}i} - h(\tan\theta - \tan\theta_i)\right] \tag{2.16}$$

where, k is the spring constant, h is the height from the LSEA output shaft to the MCP joint, and N_{cpr} is the counts per revolution of the encoder.

2.4.2 Rotary Series Elastic Actuator

The operating principle of the RSEA (Fig. 2.7) is similar to the LSEA. However, the displacement of the wave disk spring is replaced by the angular deflection of a torsion spring. One leg of the torsion spring is connected to the inner shaft, which is powered by the motor directly, while the other one is connected to the thumb thenar part that is attached to the hand. When the patient performs a grasp, the difference of the rotation angle between the inner shaft and the thumb thenar is used to calculate the torque, which is applied to the thumb thenar as

$$\tau = \kappa\Delta\phi \tag{2.17}$$

where τ is the generated torque; κ is the torsion constant, and $\Delta\phi$ is the angle difference between the inner shaft and the thumb thenar read by the angular potentiometer.

2.5 Hardware Development and Electronics Design

According to the previous research [34, 69], the LSEA is designed to measure 10N on each finger. The detailed fingertip force derivation is discussed in Sec. 2.6. To satisfy the measurement requirements and maintain the small size of the transmission system, the wave

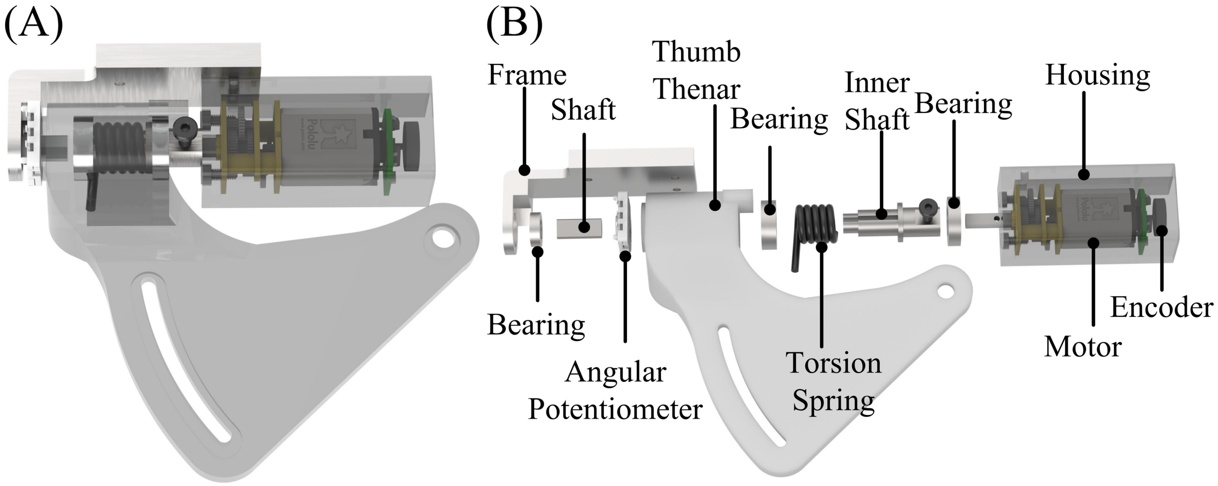

Figure 2.7: Design of RSEA for thumb thenar: (A) Perspective view of the RSEA, (B) Exploded view of the RSEA.

disk spring ($k = 5.5$N/mm, $load = 40$N), the dual shaft gear motors ($i = 380 : 1$, $T_m = 490$ N $\cdot$ mm, $n_m = 32300$RPM) and the leadscrew ($l = 20$mm, $d_m = 5.5$mm, $\alpha = 30°$, $\mu = 0.2$, $\eta_s = 0.78$, $\lambda = 49.27°$) have been selected. For the RSEA, a more powerful dual shaft gear motors ($i = 1000 : 1$, $T_m = 980$ N $\cdot$ mm, $n_m = 35000$RPM) and a torsion spring ($\kappa = 1.85$ N $\cdot$ mm/deg) were chosen.

Sensors

Each SEA includes a Bourns 3382H angular potentiometer on the side of the linkage to measure the SEA output shaft position and a 12-bit Pololu magnetic encoder to measure the input shaft position. A voltage of 21 volts is applied to the potentiometer on the linkage to achieve better measurement accuracy at small angular displacements. Both mechanical limits and over-voltage protection circuits were implemented to ensure that the measured voltage is within a measureable range. Sparkfun SN-09375 (FSR) is mounted inside the finger sleeve to provide small force slip detection and contact detection due to its exponential force sensitivity but low linearity.

Electrical Components

The glove's onboard electronics consist of four main parts, including three separate PCBs, and a lithium-ion battery pack, as shown in Fig. 2.8. Each component is connected using quickly detachable connectors for easier repair and replacement. Three individual PCBs contain two control units to process the signal from sensors and control the motor. Control unit 1 integrates a Teensy 4.1 micro-controller for multi-threading signal processing and force control, and an HC 5.0 Bluetooth model for wireless communication. This control unit is responsible for processing signals from the sensors, sending data to the server, receiving commands from the server, and performing force control. This control unit also has over-voltage protection circuit for safely reading potentiometer signals. Control unit 2 receives signals from control unit 1 and controls seven motors using Pololu md21a motor controller. The power supply PCB is used for power conversion to provide various voltages to different sub-systems. The lithium-ion battery pack contains three DTP-603050 batteries (3.7v 1050 mAh) in series to provide 11.1v output with a 1C discharge rate.

Power Consumption

The average power consumption (P) is measured by monitoring the instant current (I_{inst}) of an external power source when performing the grasping experiments above and calculated using Eqn. 2.18,

$$P = \frac{U \cdot \sum I_{inst}}{t} \tag{2.18}$$

where U is the 11.1v supplied voltage and t is the total time cost during the grasping.

The average power consumption for active grasping is 4.7W, and 1.7W for idle. A battery package that contains three 1050mAh Li–Po batteries is used to power the device. The batteries can hold up to 2.5h of continuous operation or 6.7h of idling, which is sufficient

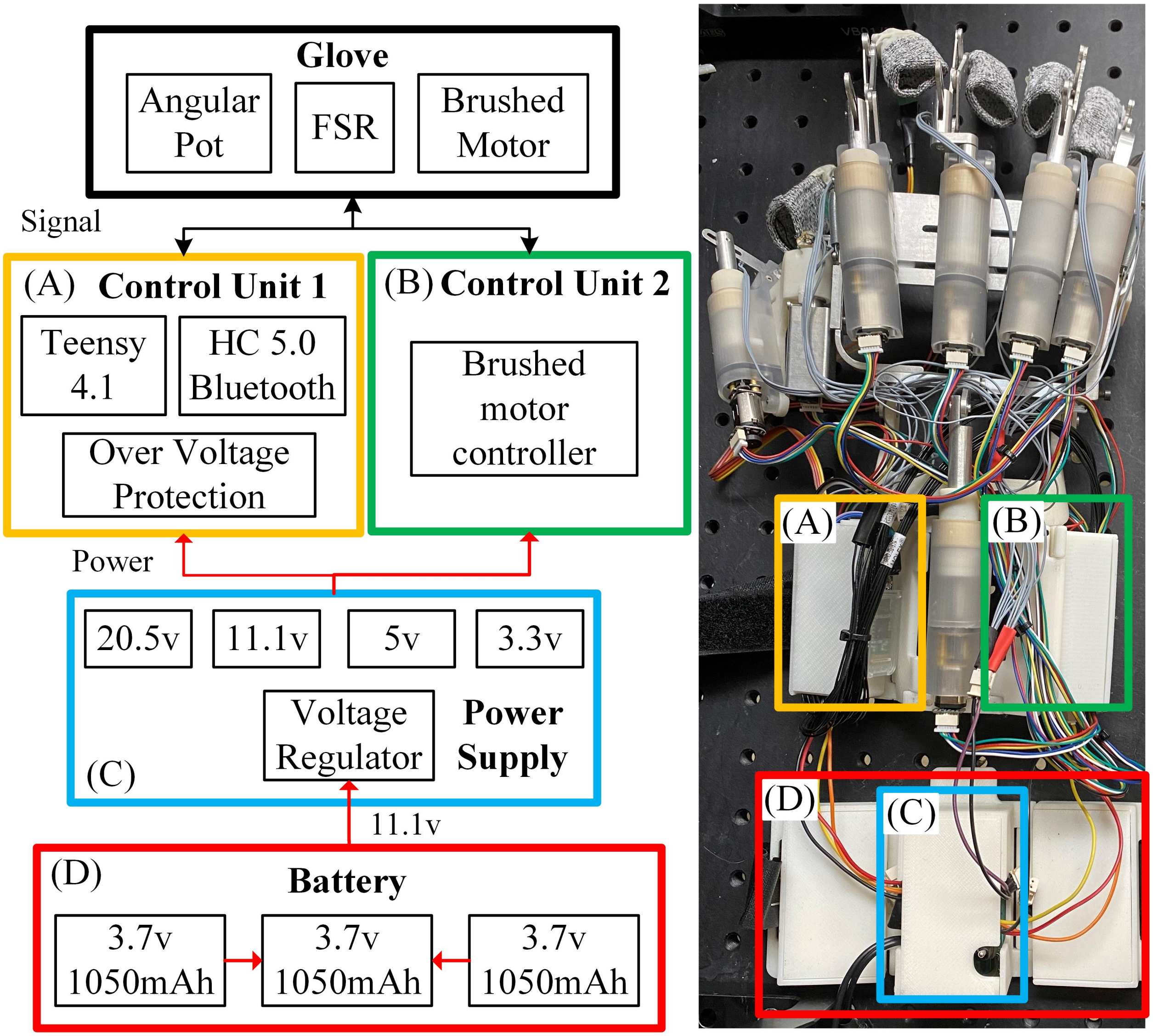

Figure 2.8: Electronics design overview: (A) micro-controller board, (B) brushed motor controller board, (C) power conversion board, (D) 3-in-1 battery package.

for our application.

2.6 Exoskeleton Glove Force Control

In this section, the estimation method that is used to eliminate the impact of backlash, and two types of prediction methods for LSEA force control based on model-based and model-free force predictive control methods are investigated. The control software architecture is also introduced. The index exoskeleton finger is used as an example for illustration purposes, while keeping in mind that the other exoskeleton fingers use the same method but different values of parameters.

2.6.1 Backlash Estimation for Linear Series Elastic Actuator

In order to achieve accurate force control, an elaborate mathematical model needs to be developed. However, the backlash causes a significant effect on the LSEAs force measurement performance. It can be sourced from the backdrivable motor and the linear motion transmission between different parts. Sleeve bearings are used instead of linear bearing due to the limited space, which cannot prevent the backlash during the motion transmission process.

To illustrate and quantify the backlash effects, the index LSEA was excited with a sinusoidal signal to push and pull the output shaft without load. The amplitudes (3mm, 6mm to 8mm) are changed as time elapses. It was shown in Sec. 2.4 that the force measurement is mainly based on measuring the displacement of the wave disk spring, which is calculated by the readings from the encoder and angular potentiometer. Fig. 2.9 shows the backlash effect between these two sensors. The gap represents the backlash.

To solve this problem, a mathematical model inspired by [70, 71, 72] was built to represent

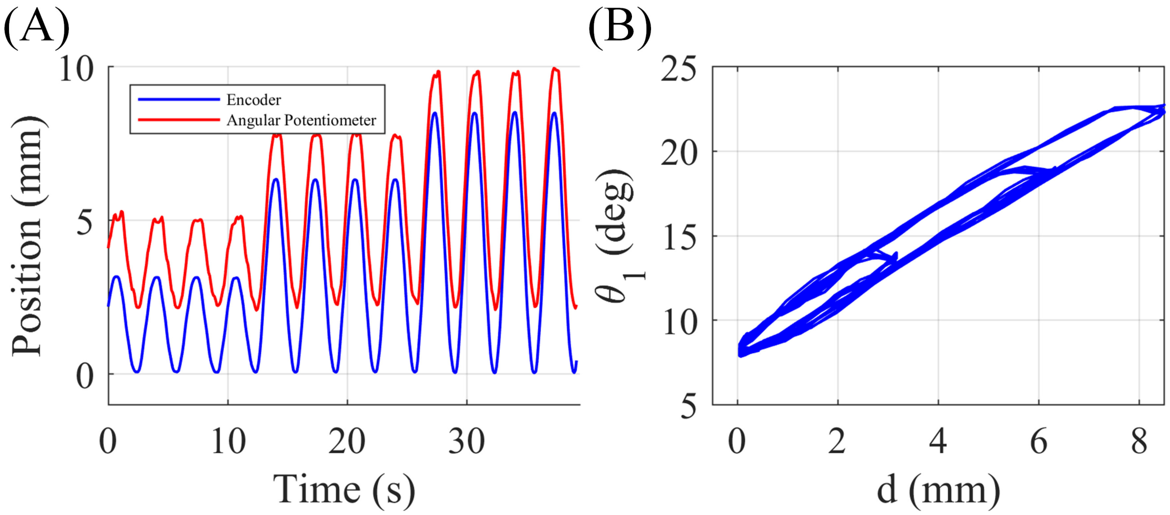

Figure 2.9: Backlash illustration. (A) The motor position calculated by encoder and angular potentiometer separately, (B) The relationship between the motor position d and the MCP joint angle θ_1.

the backlash with the assumption that the LSEAs follow a quasi-static condition. It is also worth mentioning that the leadscrew nut displacement d represents the motor position since the leadscrew is connected to the motor output shaft rigidly and can be calculated by the expression $d = \frac{l\Delta ticks}{N_{cpr}} i$, for our application. If there is no backlash, the motor position should match the angle of the MCP joint as shown in Eqn. 2.19,

$$d(t_i) = h(\tan(\theta_1(t_i)) - \tan(\theta_{init})) \tag{2.19}$$

Considering the backlash, the angle of the MCP joint can be modeled as shown in Eqn. 2.20:

$$\theta_1(t_i) = \begin{cases} \tan^{-1}\left[\frac{\alpha(d(t_i)-p_{push})}{h} + \tan(\theta_{init})\right], & \dot{d}(t_i) > 0 \\ \tan^{-1}\left[\frac{\alpha(d(t_i)-p_{pull})}{h} + \tan(\theta_{init})\right], & \dot{d}(t_i) < 0 \\ \theta_1(t_{i-1}), & otherwise \end{cases} \tag{2.20}$$

where $\theta_1(t_i)$ represents the MCP joint angle at time t_i, $d(t_i)$ represents the motor position at time t_i calculated by encoder reading, θ_{init} represents the initial angle of the MCP joint, h represents the height from the LSEA output shaft to the MCP joint, α represents the slope of the linear function, p_{push} and p_{pull} represent the offsets of push and pull movements. α, p_{push}, and p_{pull} can be calculated from the data collected under no load conditions.

The inversion of the above conditional equations (Eqn. 2.20) can be used to determine the current motor position $d(t_i)$ with respect to the current MCP joint configuration, on condition of backlash. When the load is applied on the fingertip, any further motor movement $\delta d = d_c - d(t_i)$ can be considered as motion without backlash, where d_c is the motor current position under load. The compensation is implemented by substituting

$$d = \frac{l \Delta ticks}{N_{cpr}} i \tag{2.21}$$

into Eqn. 2.16 and replacing d with δd. However, when the LSEA changes the direction of motion, the actual movement is continuous but the derived model is discontinuous. A smooth parameter

$$\gamma = \frac{1}{1 + e^{-\beta \dot{d}(t_i)}} \tag{2.22}$$

based on the sigmoid function is used to eliminate discontinuity. Here, β represents the smoothness between each condition. Thus, the inverse backlash model with a smooth parameter can be expressed as follows,

$$d(t_i) = \frac{h(\tan(\theta_1(t_i)) - \tan(\theta_{init}))}{\alpha} + p_{push}\gamma + p_{pull}(1-\gamma) \tag{2.23}$$

2.6.2 Friction Force Compensation

In addition to backlash, frictional forces also have a significant impact on force calculations. Friction may occur between various pairs of relative movements, such as the lead screw and linear SEA housing, and the output shaft and sleeve bearing. A simple test platform was built as shown in Fig. 2.10 (A) to assess the friction force. In this setup, the linear SEA is instructed to push forward and generate 4N to 24N forces based on a predefined linear SEA force model. The actual generated force is measured using a load cell located in the front of the platform.

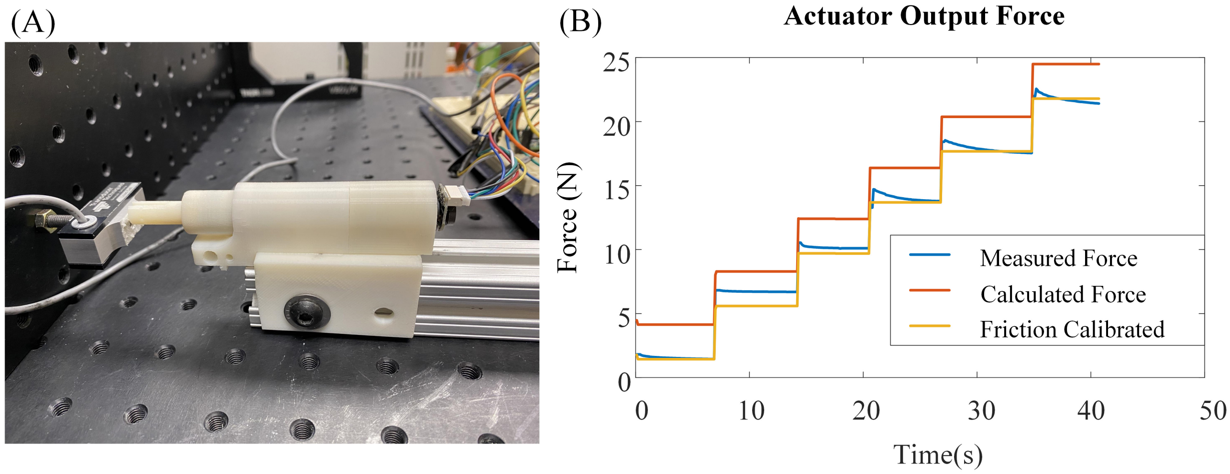

Figure 2.10: Friction force illustration. (A) The test platform to measure the generated force on the linear SEA output shaft, (B) The difference between the measured force and calculated force based on the linear SEA model, which is caused by friction force.

The results depicted in Fig. 2.10 (B) illustrate the influence of friction force. It is evident that there is a noticeable discrepancy between the calculated force and the force measured by the load cell. This difference can be primarily attributed to the presence of friction force within the linear SEA.

Since the linear SEA requires the MCP joint rotation angle to calculate the force, it is also necessary to consider the finger linkage to measure the friction force. Experimental measurements were conducted to accurately quantify the combined friction force resulting from the finger linkage and the linear SEA. The linear SEA was actuated against a load cell from various angles to assess the friction force. The expectation was that as the linear SEA was actuated, the compression measured from the linear SEA would increase while the load cell reading would remain at zero. However, once the applied force exceeded the friction force threshold, the load cell reading would no longer be zero. In this case, the compression of the spring was used to quantify the magnitude of the friction force. The obtained results, depicted in Figure 2.11, illustrate the variation in friction forces observed at different angles.

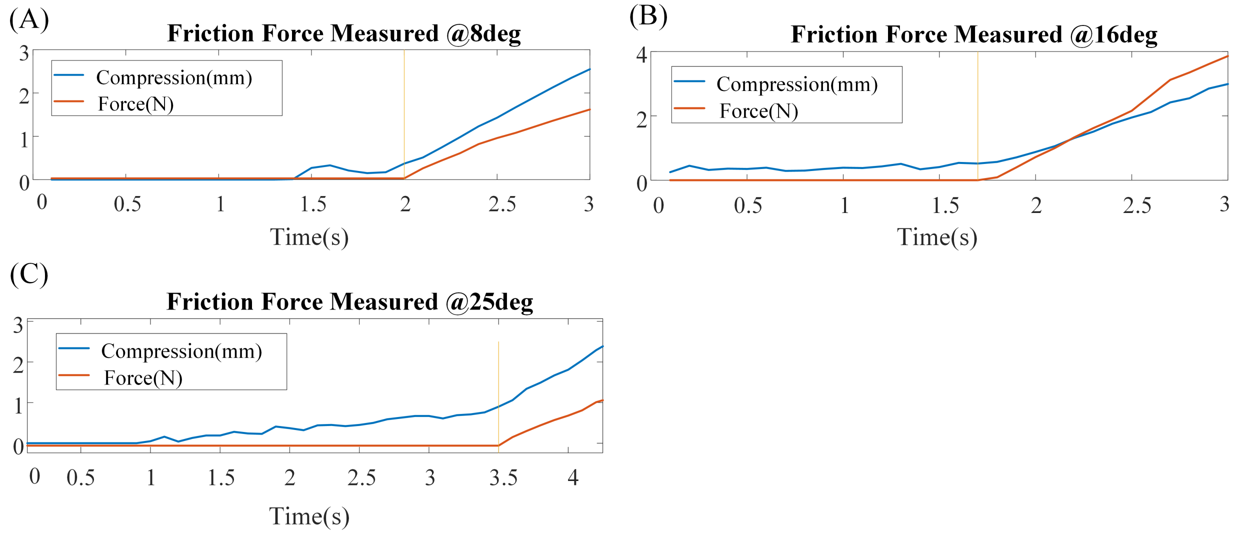

Figure 2.11: Example of measuring frictional force at various angles. (A) Friction at an 8° MCP joint angle is 2.1N, (B) Friction at a 16° MCP joint angle is 2.4N, (C) Friction at a 25° MCP joint is 4.45N.

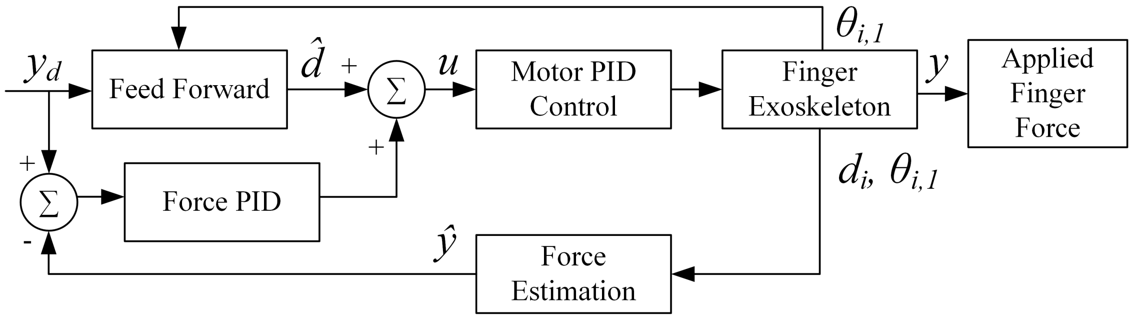

Figure 2.12: Force control scheme for a single exoskeleton finger. $\theta_{i,1}$ represents the MCP joints of exoskeleton finger $i(i \in \{1,2,3,4,5\})$. d_i represents the current motor position of exoskeleton finger i.

2.6.3 Model-based Force Control Policy

The goal of the currently designed controller is to track the desired forces applied to the fingertips by the exoskeleton. Fig. 2.12 shows the proposed control scheme. It is worth mentioning that the action/contact force on the load is assumed to be perpendicular to the last link, for a stable grasp. The estimated action force $\widehat{\mathbf{y}}$ magnitude can be expressed as the function $\hat{y} = f(d, \theta_1)$ with respect to the motor current position d and the MCP joint current angle θ_1. Similarly, giving the information of desired action force y_d and measured MCP joint angle θ_1, the required motor position $\hat{d}$, which is predicted by feed-forward part, can be expressed as $\hat{d} = g(y_d, \theta_1)$.

The PID controller with the corresponding feed-forward and feed-back terms is then given by Eqn. 2.24,

$$\begin{aligned} \hat{y} &= f(d, \theta_1) \\ e &= y_d - \hat{y} \\ \hat{d} &= g(y_d, \theta_1) \\ u &= \hat{d} + k_p e + k_d \dot{e} + k_i \int e dt \end{aligned} \tag{2.24}$$

Considering the kinematics model derived in Sec. 2.3, $\widehat{\mathbf{y}}$ can be estimated by the principle of virtual work, as expressed in Eqn. 2.25:

$$\langle \mathbf{T}, \delta \boldsymbol{\theta}_1 \rangle = \langle \widehat{\mathbf{y}}, \delta \mathbf{p} \rangle \tag{2.25}$$

where $\mathbf{T} = \mathbf{F}_{SEA} \cdot h$, $\mathbf{F}_{SEA}$ is calculated by solving Eqn. 2.16 and Eqn. 2.23 simultaneously to take backlash estimation into account, h is the distance from the LSEA output shaft to MCP joint (Fig. 2.2), $\mathbf{p}$ is the position of endpoints, $\langle , \rangle$ is the dot product of the vectors. Considering Eqn. 2.10, the $\widehat{\mathbf{y}}$ can be expressed as Eqn. 2.26,

$$\widehat{\mathbf{y}} = \begin{bmatrix} \hat{y}_x \\ \hat{y}_y \end{bmatrix} = T \cdot \begin{bmatrix} \frac{\tan \theta_3}{J_1 \tan \theta_3 + J_2} \\ \frac{1}{J_1 \tan \theta_3 + J_2} \end{bmatrix} \tag{2.26}$$

where J_1 is the first element of the Jacobian, J_2 is the second element of the Jacobian, θ_3 is the angle between the last link and x-axis (Fig. 2.2), $\hat{y}_x$, and $\hat{y}_y$ are the component of forces $\widehat{\mathbf{y}}$ in global x direction and y direction, respectively.

Similarly, solving the simultaneous equations of Eqn. 2.16 and Eqn. 2.20, the estimation of motor position $\hat{d}$ can be calculated based on the desired force y_d and the MCP joint current angle θ_1.

The accuracy of the proposed control method depends on the accuracy of the model-based force estimation function $f(d, \theta_1)$ and motor position estimation function $g(y_d, \theta_1)$. The prerequisites for such functions are the assumptions of no friction force, rigid parts, and no backlash inside the LSEA. However, the actual LSEA system does not satisfy these critical conditions. The simplified mathematical model causes a significant impact on the accuracy of force control.

2.6.4 Model-free Data-Driven Force Predictive Control Policy

To solve the problems mentioned above in an effort to achieve more accurate force control, a data-driven method to estimate the action force $\hat{y} = \hat{f}(d, \theta_1)$ on the fingertip, and the required motor position $\hat{d} = \hat{g}(y_d, \theta_1)$ for the desired force generation is proposed. The control scheme that was used is shown in Fig. 2.12.

The proposed method is inspired by the dynamic mode decomposition (DMD) methods [73, 74], sparsity in dynamical systems [75, 76], and sparse identification of nonlinear dynamics method [77, 78]. Similarly, the method is based on observations that most physical systems have only a few relevant terms that define the dynamics, making the governing equations sparse in a high-dimensional nonlinear function space. The difference is that our method does not estimate the dynamic model but estimates the output directly based on measurable features. In addition, one more strict assumption is added such that all other unmeasurable features depend on measurable features. To collect the data, the actual action force magnitude vector $[\mathbf{y_m}]_{n\times 1}$ of n samples applied on the fingertip is measured by pressing the finger mechanism on a six-axis load cell, while the actual motor position vector $[\mathbf{d_m}]_{n\times 1}$ is calculated directly from a rotary encoder. The estimation was solved by sparse regression methods.

For the force prediction function $\hat{y} = \hat{f}(d, \theta_1)$, the current motor position and the current angle of the MCP joint θ_1 are selected as basic features since they are either measured directly by sensors or the measured parts are precisely aligned with sensors. Because the directly measured features are not enough for data analysis, an augmented feature set is constructed which consists of nonlinear functions of basic features by looking into the dynamic model under the ideal condition and surmising the relevant term. The feature set includes the constant ($[\mathbf{1}]_{n\times 1}$), polynomial ($[\mathbf{P}]_{n\times 2m}$), trigonometric ($[\mathbf{T_{sin}}]_{n\times 2m}$, $[\mathbf{T_{cos}}]_{n\times 2m}$)

and combination of polynomial and trigonometric ($[\mathbf{C_{sin}}]_{n\times m^2}$, $[\mathbf{C_{cos}}]_{n\times m^2}$) terms as shown in Eqn. 2.27-2.31,

$$\mathbf{P} = \begin{bmatrix} d_1 & \cdots & d_1^m & \theta_{1,1} & \cdots & \theta_{1,1}^m \\ \vdots & \ddots & \vdots & \vdots & \ddots & \vdots \\ d_n & \cdots & d_n^m & \theta_{1,n} & \cdots & \theta_{1,n}^m \end{bmatrix} \tag{2.27}$$

$$\mathbf{T_{sin}} = \begin{bmatrix} \sin(d_1) & \cdots & \sin(md_1) & \sin(\theta_{1,1}) & \cdots & \sin(m\theta_{1,1}) \\ \vdots & \ddots & \vdots & \vdots & \ddots & \vdots \\ \sin(d_n) & \cdots & \sin(md_n) & \sin(\theta_{1,n}) & \cdots & \sin(m\theta_{1,n}) \end{bmatrix} \tag{2.28}$$

$$\mathbf{T_{cos}} = \begin{bmatrix} \cos(d_1) & \cdots & \cos(md_1) & \cos(\theta_{1,1}) & \cdots & \cos(m\theta_{1,1}) \\ \vdots & \ddots & \vdots & \vdots & \ddots & \vdots \\ \cos(d_n) & \cdots & \cos(md_n) & \cos(\theta_{1,n}) & \cdots & \cos(m\theta_{1,n}) \end{bmatrix} \tag{2.29}$$

$$\mathbf{C_{sin}} = \begin{bmatrix} d_1\sin(\theta_{1,1}) & \cdots & d_1\sin(m\theta_{1,1}) & \cdots & d_1^m\sin(m\theta_{1,1}) \\ \vdots & & \ddots & & \vdots \\ d_n\sin(\theta_{1,n}) & \cdots & d_n\sin(m\theta_{1,n}) & \cdots & d_n^m\sin(m\theta_{1,n}) \end{bmatrix} \tag{2.30}$$

$$\mathbf{C_{cos}} = \begin{bmatrix} d_1\cos(\theta_{1,1}) & \cdots & d_1\cos(m\theta_{1,1}) & \cdots & d_1^m\cos(m\theta_{1,1}) \\ \vdots & & \ddots & & \vdots \\ d_n\cos(\theta_{1,n}) & \cdots & d_n\cos(m\theta_{1,n}) & \cdots & d_n^m\cos(m\theta_{1,n}) \end{bmatrix} \tag{2.31}$$

where m specifies the highest polynomial order. Each row represents the feature values corresponding to the specific data sample. It is worth to mention that it is not necessary to add the combination of polynomial and trigonometric terms if the order is high, since the separate terms have considered linearity and non-linearity of the data. However, such combination terms provide the diversity of the augmented features when the order is low. The feature matrix $[\mathbf{X_y}]_{n\times(2m^2+6m+1)}$ can be represented as Eqn. 2.32,

$$\mathbf{X_y} = [\mathbf{1} \quad \mathbf{P} \quad \mathbf{T_{sin}} \quad \mathbf{T_{cos}} \quad \mathbf{C_{sin}} \quad \mathbf{C_{cos}}] \tag{2.32}$$

and the force estimation $[\widehat{\mathbf{y}}]_{n\times 1}$ can be the linear combination of constructed features matrix with proper weights vector $[\mathbf{b_y}]_{(2m^2+6m+1)\times 1}$ as shown in Eqn. 2.33,

$$\widehat{\mathbf{y}} = \mathbf{X_y}\mathbf{b_y} \tag{2.33}$$

For the motor position prediction function $\hat{d} = \hat{g}(y_d, \theta_1)$, the $[\mathbf{X_d}]_{n\times(2m^2+6m+1)}$ is constructed by using the same feature matrix structure, estimated the weights vector$[\mathbf{b_d}]_{(2m^2+6m+1)\times 1}$, and replaced the estimated force $\widehat{\mathbf{y}}$ with estimated position $[\widehat{\mathbf{d}}]_{n\times 1}$ as shown in Eqn. 2.34,

$$\widehat{\mathbf{d}} = \mathbf{X_d}\mathbf{b_d} \tag{2.34}$$

Intuitively, the more features we use, the more accurate predictor we can get. However, previous research [77, 78] has shown that some major features are enough to estimate the original functions under a reasonable precision, making it sparse in the space of possible functions. Moreover, the large number of negligible features wastes the computing power and decreases the control frequency. Given the above conditions, the least absolute shrinkage and selection operator (LASSO) is imported to perform the feature selection and regularization for the accuracy prediction, as shown in Eqn. 2.35—2.36,

$$\underset{\mathbf{b_y}}{\operatorname{argmin}} \left(\frac{1}{2n} ||\mathbf{X_y}\mathbf{b_y} - \mathbf{y_m}||_2^2 + \lambda_y ||\mathbf{b_y}||_1 \right) \tag{2.35}$$

$$\underset{\mathbf{b_d}}{\operatorname{argmin}} \left(\frac{1}{2n} ||\mathbf{X_d} \mathbf{b_d} - \mathbf{d}||_2^2 + \lambda_d ||\mathbf{b_d}||_1 \right) \tag{2.36}$$

where λ_y and λ_d are the non-negative regularization parameters.

By calculating the linear combination of the features created by real-time data, with non-zero weights in $\mathbf{b_y}$, $\mathbf{b_d}$, the $\widehat{\mathbf{y}}$, $\widehat{\mathbf{d}}$ are predicted. Theoretically, the proposed data-driven method takes backlash, parts deformation, and friction forces into account since such immeasurable variables are hidden behind the relationships between the measurable data.

2.6.5 Control Software Architecture

The exoskeleton control software architecture can be divided into a high-level controller, which runs on a mobile device, and a low-level controller, which runs on the onboard Teensy 4.1 micro-controller.

The high-level controller consists of two parts. The first part is the voice data input from a Bluetooth Microphone, which will be sent to the configurable voice activation and speaker verification human-machine interference (CVASV HMI) [55]. The CVASV HMI supports customized activation keywords and provides voice-based bio-authentication while converting speech to text. The CVASV HMI will be activated by the bio-authenticated voice command gathered from the user. The type of grasps that need to be performed will be passed to the slip grasp program. The second part is the slip detection program. If the object slips while being lifted, the system will add force incrementally to each SEA. The force command will be sent from the computer to the micro-controller. The two high-level controllers mentioned above run on a computer in parallel to ensure voice commands can be received and executed while sending the commands to low-level controllers. The control structure is shown in Fig. 2.13.

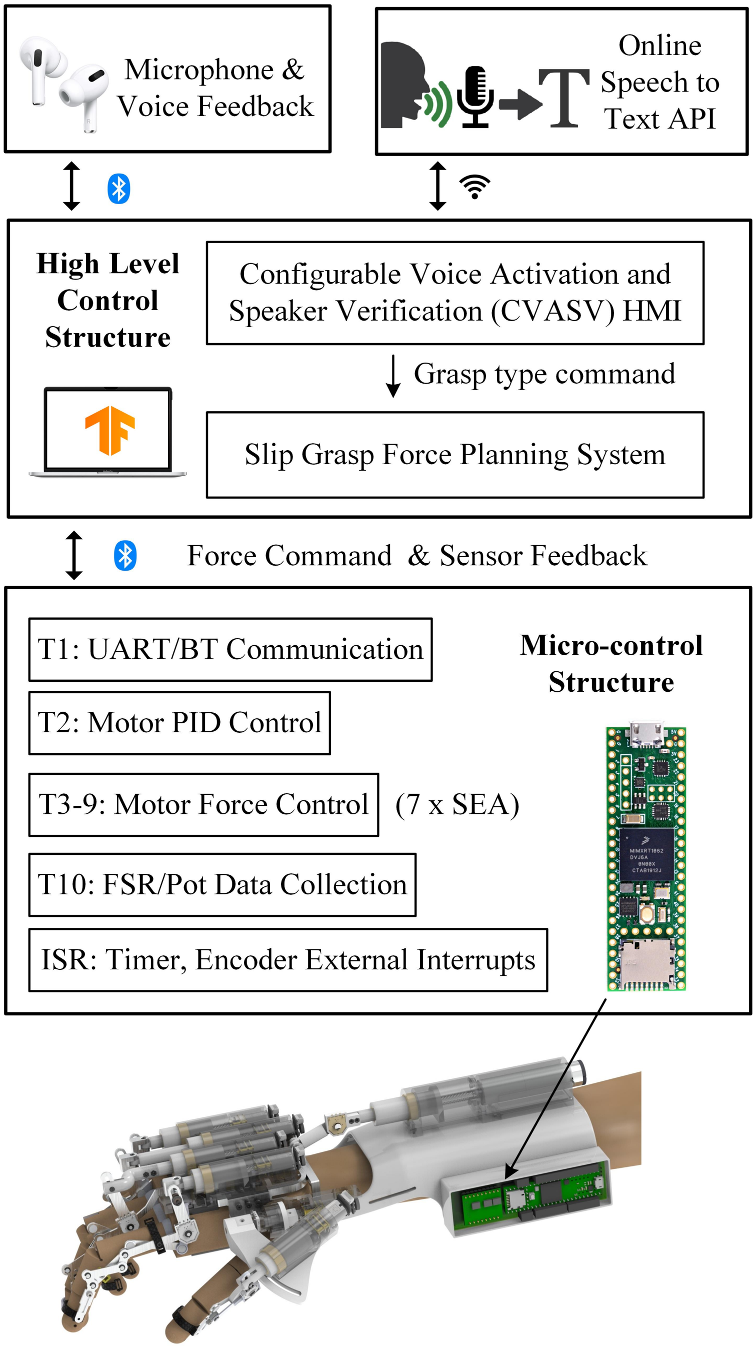

Figure 2.13: Illustration of the control software architecture. Patient's voice command is captured via earphones, from which the grasp type is extracted and conveyed to the slip grasp force planning system. The resulting force command is subsequently transmitted to the micro-controller for the purpose of actuators control.

The force control process of the LSEAs can be divided into three sections. First, the force command is sent to the micro-controller from the computer grasping program through Bluetooth (BT). BT communication thread (T1) will parse the command into desired force output on each fingertip. Second, the motor force controller (T3) will follow the control schema shown in Fig. 2.12 to predict the motor position u. Third, the motor force controller (T3) commands the motor PID controller (T2) to regulate the SEA input shaft to achieve desired forces on the fingertips. All 7 SEAs run in parallel on T3-T9 at 10Hz on a Teensy 4.1 Micro-controller using FreeRTOS to ensure minimal control latency. The control structure is shown in Fig. 2.13.

2.6.6 Comparison of the Model-based and the Model-free Data-Driven Force Control

In this section, the performance of the two proposed control methods are compared thoroughly.

Data Preparation

The data collection is performed on two different test platforms (Fig. 2.14) to measure the force on the fingertips. During the data collection process, the LSEA was mounted on a stand that simulates the human hand. The six-axis load cell (ATI mini45, resolution 0.25N) is fixed either horizontally or vertically to accommodate different exoskeleton finger configurations. The index exoskeleton finger is set up as an example to show the performance.

Considering the force leverage between the LSEA and the fingertip which depends on the angle of the MCP joint (θ_1), a set of θ_1 (roughly around 10°, 12°, 14°, 19°, 23°, 25°, and 27°) when contact happens is predefined as the test configuration. The motor controller

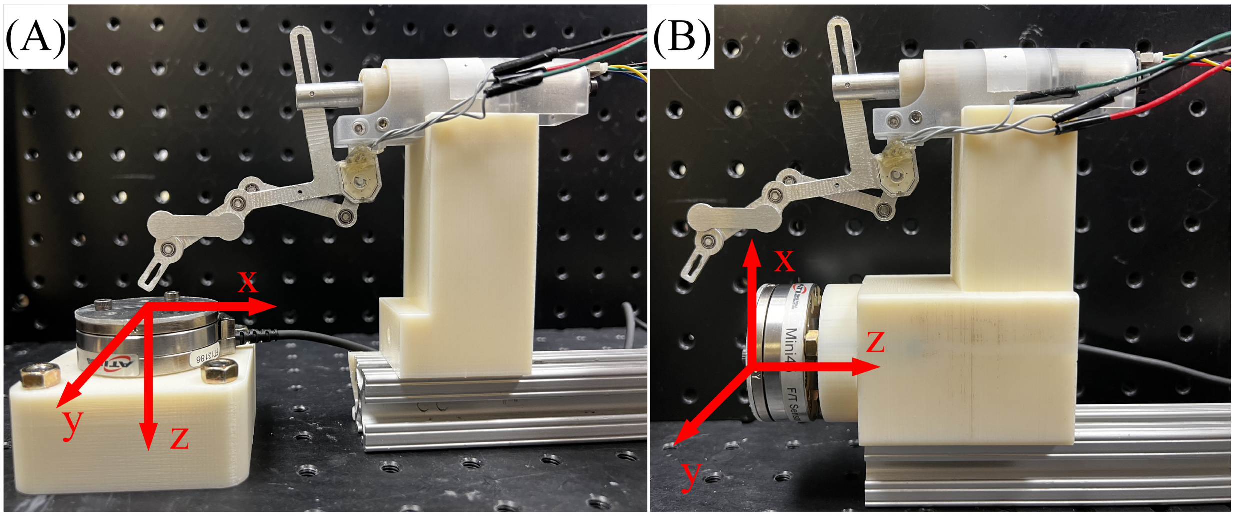

Figure 2.14: Test platform with different load cell mounting positions. (A) load cell is mounted horizontally. (B) load cell is mounted vertically.

is designed to output a sinusoidal position signal on the leadscrew nut (Fig. 2.15). The highest normal force is limited to a range from 5N to 10N by changing the magnitude of the sinusoidal signal. Each angle configuration was performed three times and two of them were randomly selected for training. The remaining data was used for testing. Since the lateral and friction forces are negligible compared with the normal force detected by the load cell as shown in Fig. 2.16, we assumed that the normal force detected by the load cell is the total reaction force on the fingertip.

Fingertip Force Prediction

The backlash model experiments include 3 identical sets. Each of them repeats a back and forth motion to one of the designed motor positions (3mm, 6mm, 8mm and initial at 0mm) 4 times, continuously. Fig. 2.17 shows the backlash estimation result based on the defined mathematical model. The root mean squared (RMS) error for the motor current position estimation based on the current MCP joint angle is 0.27mm.

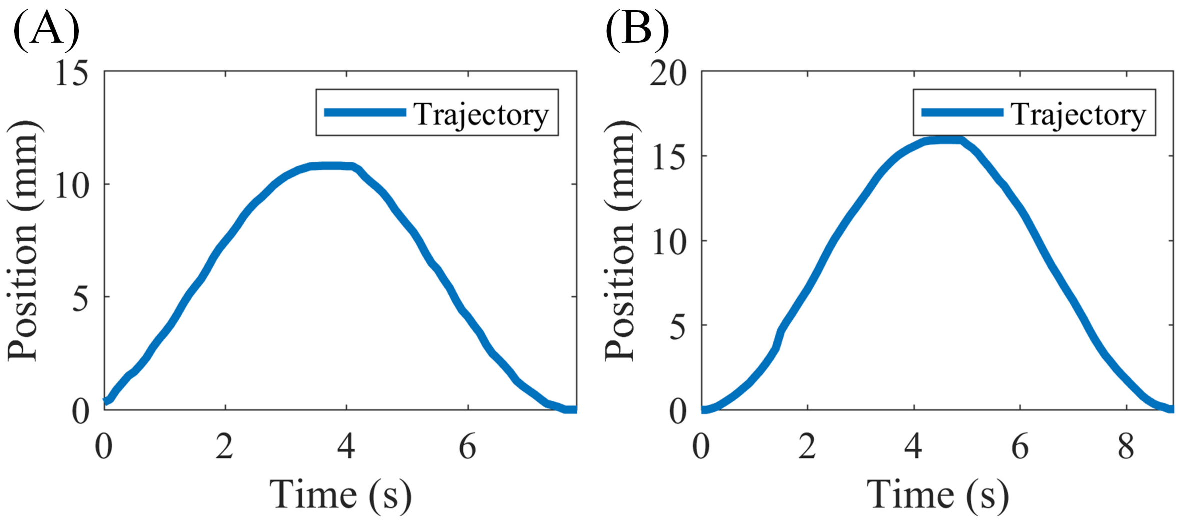

Figure 2.15: (A) The LSEA motor position trajectory with load cell horizontal installation ($\theta_1 = 12°$). (B) The LSEA motor position trajectory with load cell vertical installation ($\theta_1 = 25°$).

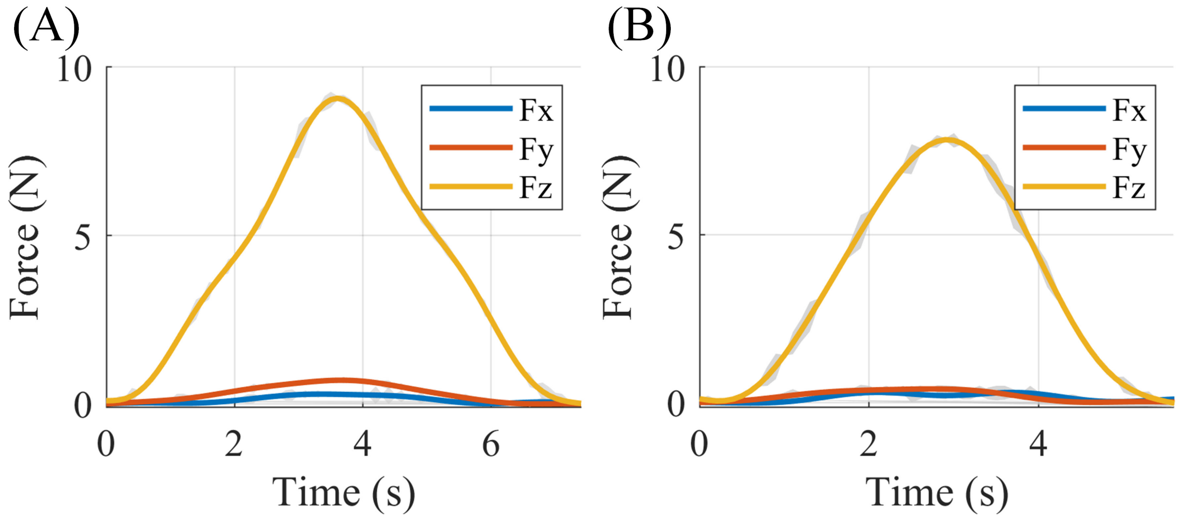

Figure 2.16: (A) Force measurement with load cell horizontal installation ($\theta_1 = 12°$). (B) Force measurement with load cell vertical installation ($\theta_1 = 25°$).

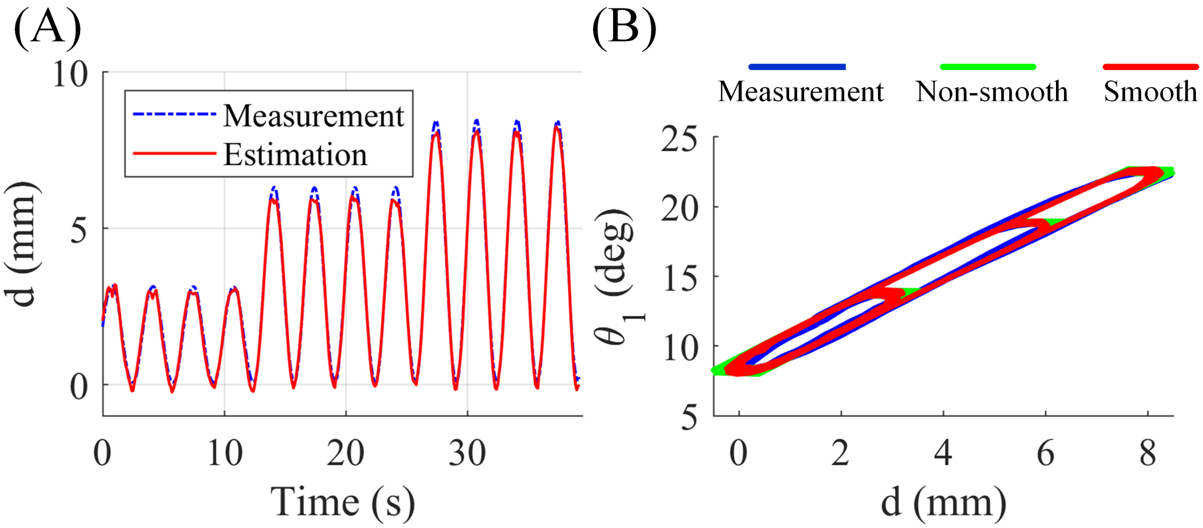

Figure 2.17: (A) The comparison between the estimation of motor current position and measurement from encoder. (B) The comparison between the estimation of motor current position and measurement from encoder, related to MCP joint angle θ_1.

The model-based force prediction is implemented with the developed backlash model (Sec. 2.6.3). The results on the training and test datasets are shown in Fig. 2.18 and Fig. 2.19, respectively. The mean squared error (MSE) on the training dataset and test dataset is 2.65 and 1.46, respectively. In most cases, the model-based calculation is larger than the measurements since the impact of deformable parts and friction force are hard to measure and are not considered in the model. Moreover, the model is not robust enough to counter the vibration noise of the angular potentiometer at the beginning and end of contact. In addition, the backlash model is estimated under no load conditions, which is different compared to the working conditions. Every measurement error or estimation error is accumulated in the final results.

For the model-free force prediction, the MSE and the number of active features of the highest polynomial order from 3 to 20 are compared, as shown in Fig. 2.20. The highest polynomial order that equals 10 was picked since the MSE decrease slows down while achieving the acceptable active features number. One hundred eligible non-negative λ_y values are

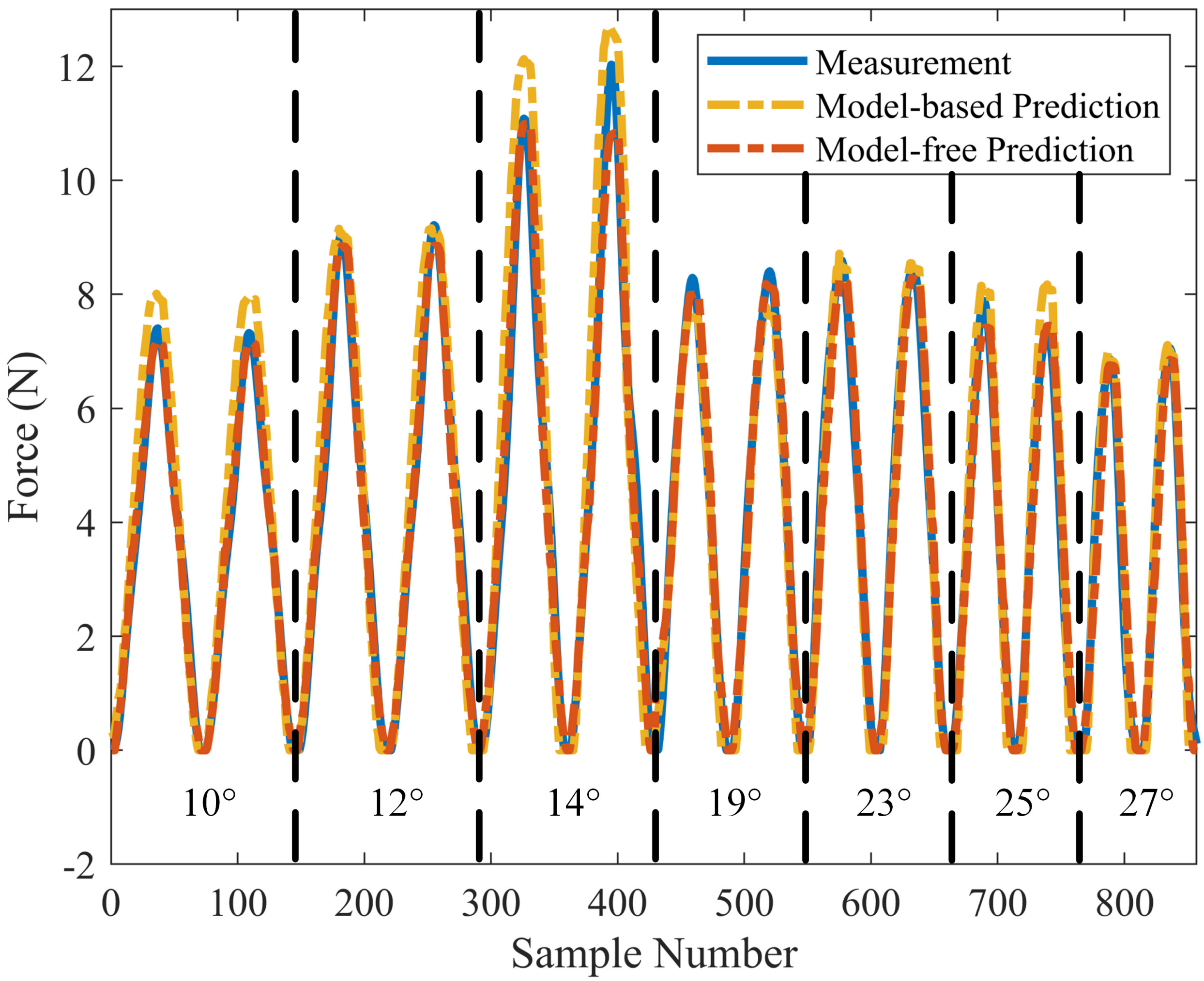

Figure 2.18: Force prediction results on training dataset with different θ_1 configurations. Each configuration is performed twice in sequential order. Different configurations are not time related.

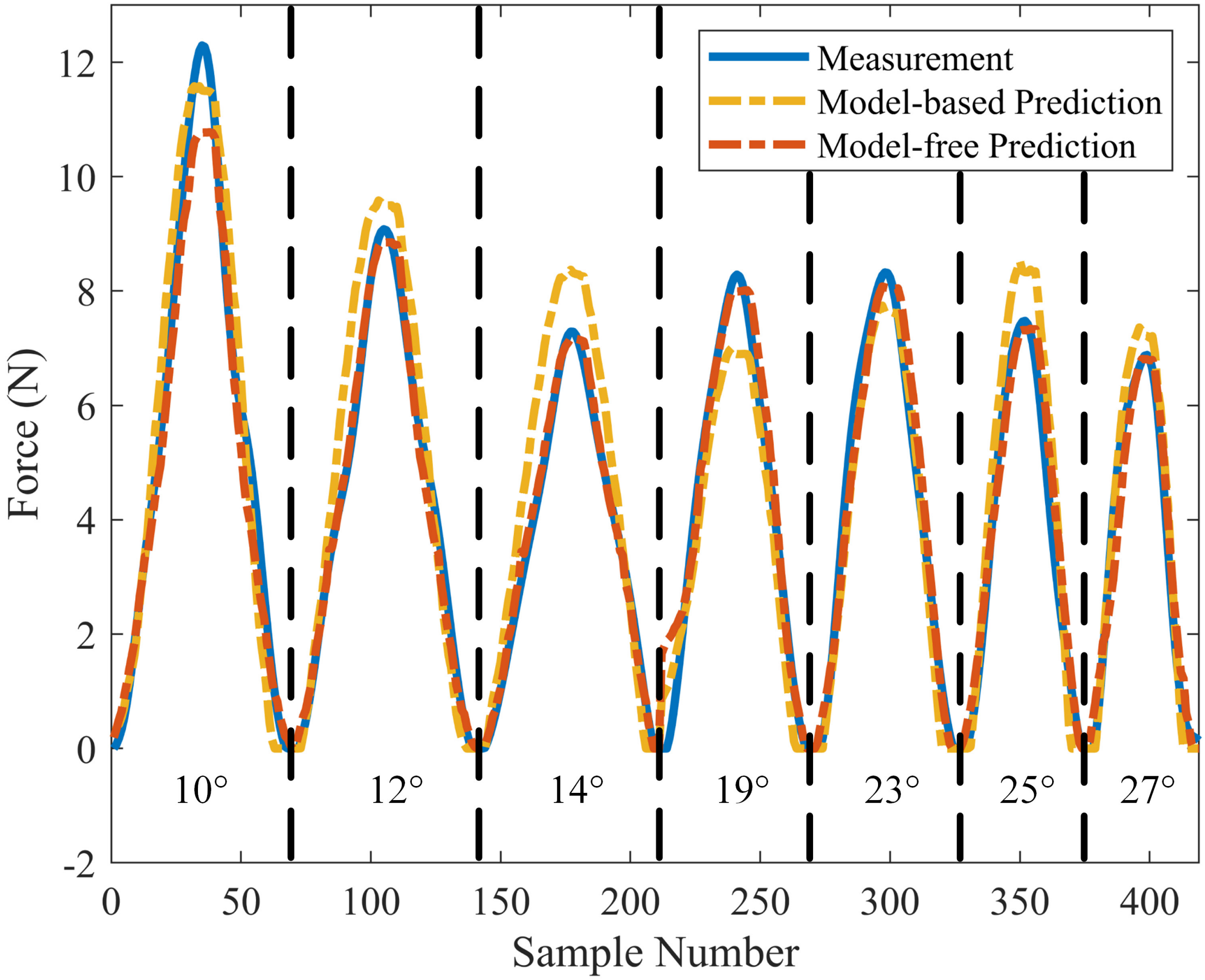

Figure 2.19: Force prediction results on test dataset with different θ_1 configurations. Each configuration is performed once. Different configurations are not time related.

calculated and ranked in an ascending order. The first 50 λ_y were selected to be analyzed. According to the results shown in Fig. 2.21, as lambda increased, the number of active features dramatically decrease but the MSE increases quickly. Considering the resolution of the load cell, The $\lambda_y = 0.0003$ is chosen which results in 65 active features in total and achieve acceptable MSE (0.20 on the training dataset and 0.25 on the test dataset).

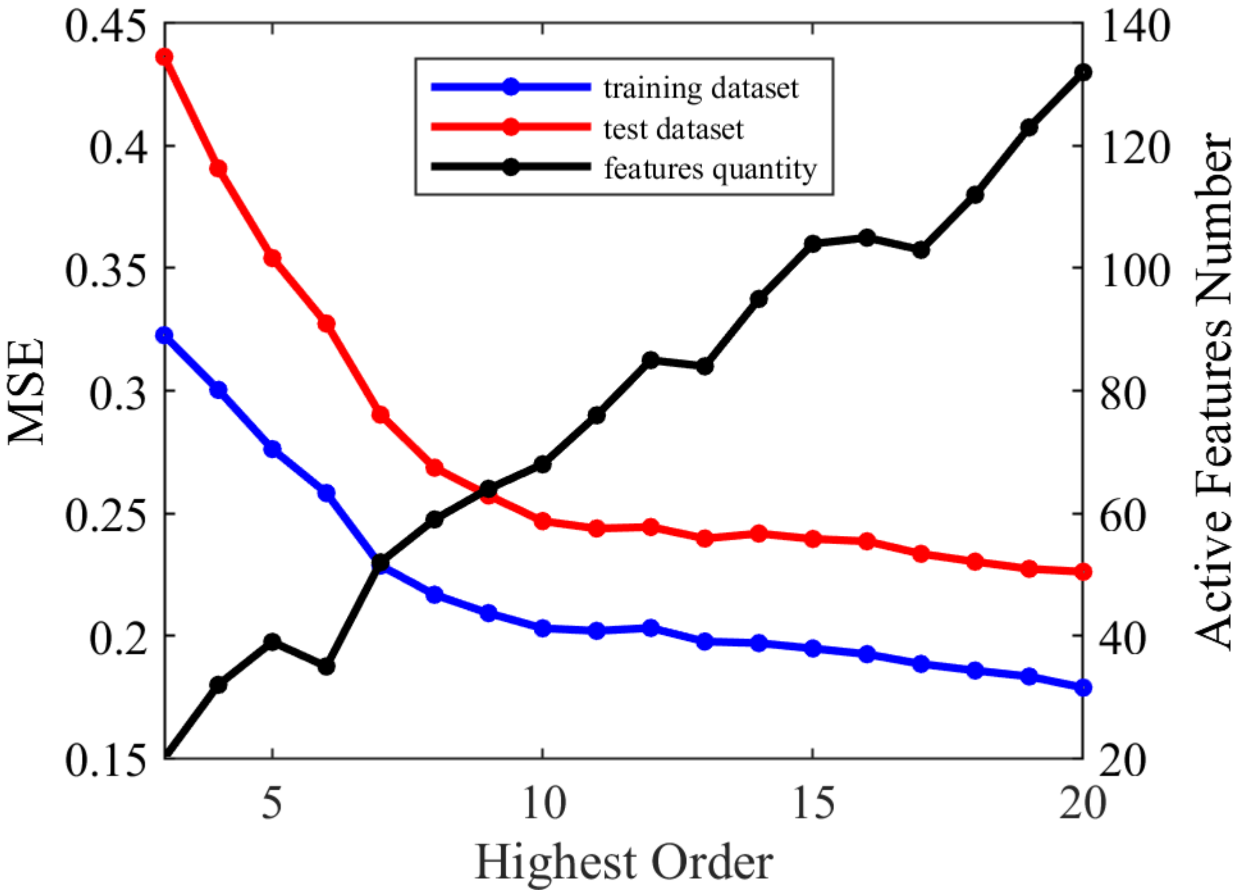

Figure 2.20: The red and blue curves illustrate the comparison of Mean Squared Error (MSE) on both the training dataset and the test dataset across different highest polynomial orders. The black curve represents the relationship between the number of active features and the various highest polynomial orders.

The estimation results of the training dataset and the test dataset are shown in Fig. 2.18 and Fig. 2.19, respectively. It is worth mentioning that the applied fingertip force that

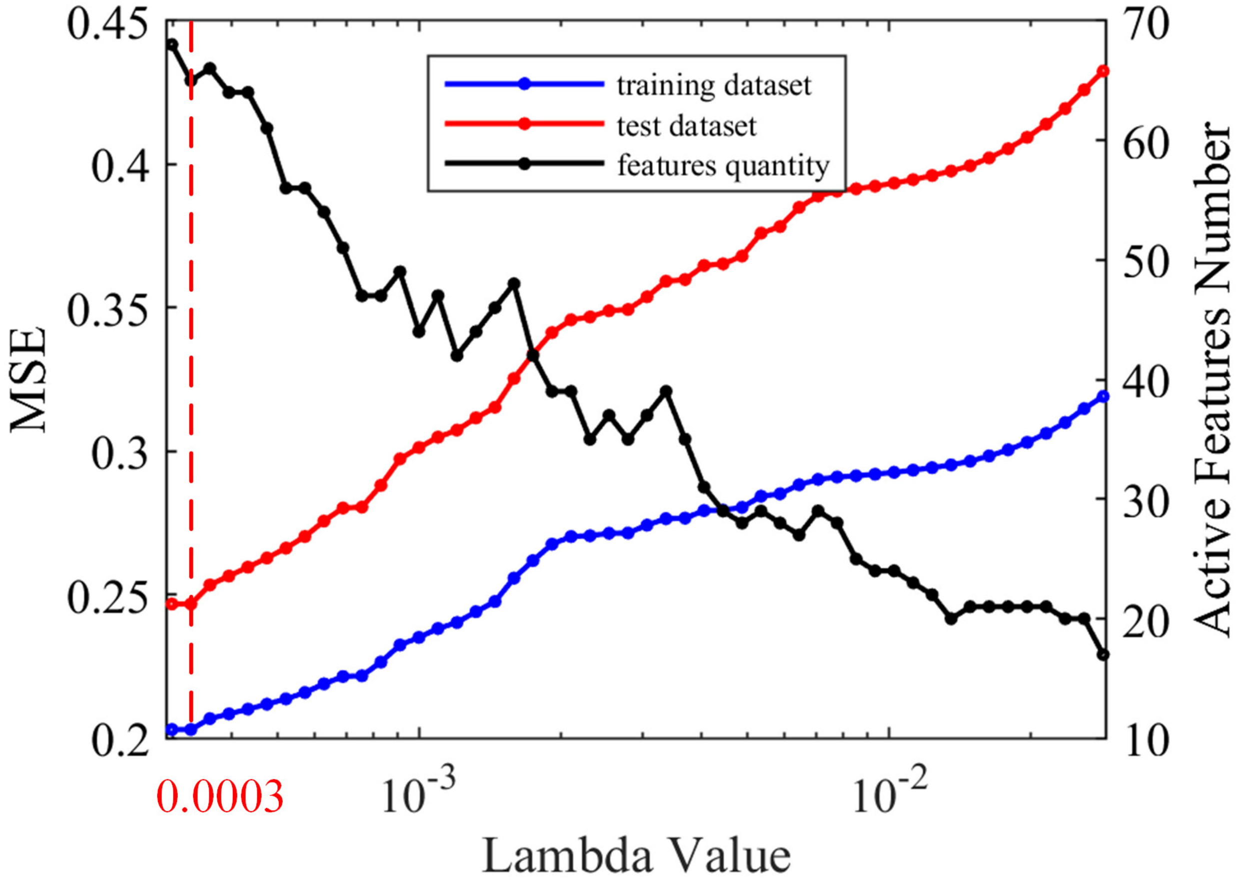

Figure 2.21: The red and blue curves illustrate the comparison of Mean Squared Error (MSE) on both the training dataset and the test dataset across different λ_y. The black curve represents the relationship between the number of active features and the various λ_y.

is larger than 10N may not be estimated accurately with low θ_1 configuration since the force exceeds the measuring range of the LSEA due to the large mechanical advantage. Besides the advantage of accuracy compared with the model-based method, the model-free force prediction is more robust to vibrational noise at the beginning of the contact and the end of the contact.

Based on the results presented above, the model-free force prediction performs much better than the model-based force prediction.

Motor Position Prediction

The motor position prediction is incorporated as the feed-forward part in the control system. Since the forces corresponding to the condition where $y_d > 0$ are needed, the part of the data where the measured forces result in $y_m \leq 0$ in the prepared dataset are ignored. The model-based motor position prediction is implemented with the developed backlash model without smoothing since the gradient of the motor position is unknown. Fig. 2.22 and Fig. 2.23 show the results on the training and the test dataset with different θ_1 configurations. The MSE on each dataset is 1.2 and 1.6, respectively. The error mostly occurs when the motor direction is changed, which may be caused by the error of the non-smooth backlash model as shown in Fig. 2.17.

For the model-free motor position prediction, the MSE and the number of active features of the highest polynomial order from 3 to 20 are compared, as shown in Fig. 2.24. The highest polynomial of order 13 was selected since the MSE decrease slows down and the active features number is acceptable. One hundred eligible non-negative λ_d are calculated and ranked them in ascending order. The first 50 λ_d were selected to be analyzed (Fig. 2.25). Here, the first one ($\lambda_d = 0.00036$) are chosen which results in the lowest MSE since

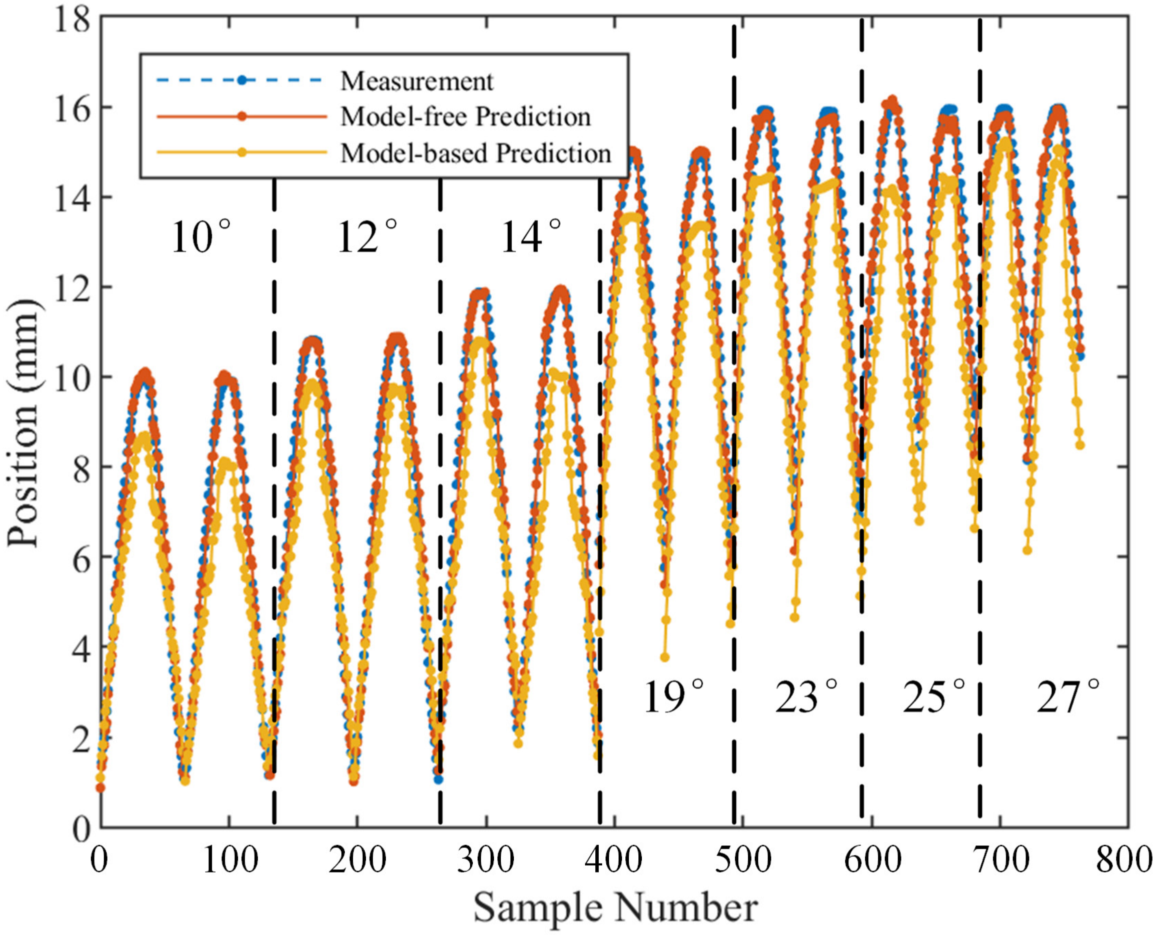

Figure 2.22: Results of motor position prediction on training dataset with different θ_1 configurations. Each configuration has 2 sets of data. The x-axis represents the sample number which is put in time order. Different sets of data are not time related.

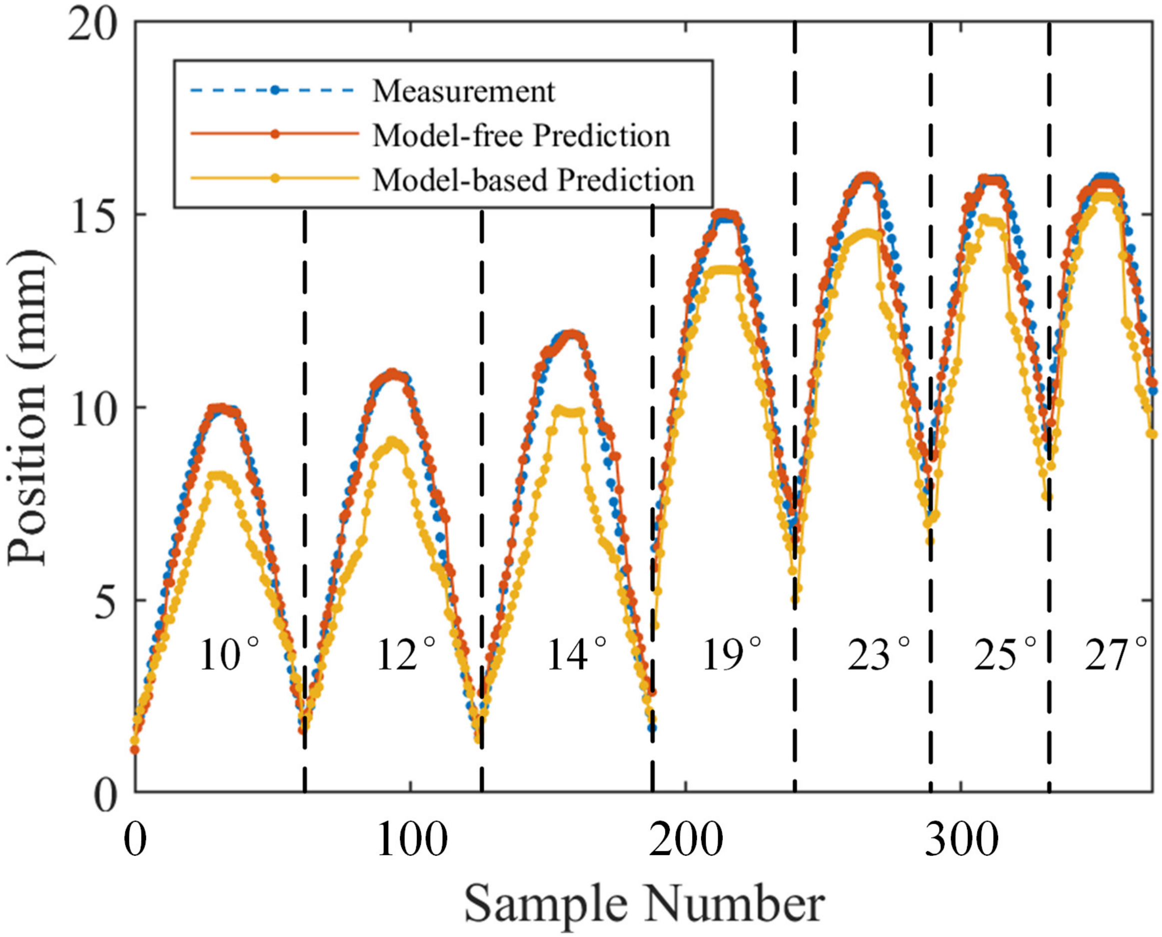

Figure 2.23: Results of motor position prediction on test dataset with different θ_1 configurations. Each configuration has 1 set of data. The x-axis represents the sample number which is put in time order. Different sets of data are not time related.

the resolution of the encoder is much lower than the calculated MSE (0.16 on the training dataset and 0.2 on the test dataset) with an acceptable number of active features. The estimation results of the training dataset and the test dataset are shown in Fig. 2.22 and Fig. 2.23, respectively. The prediction performs good tracking of the measurement.

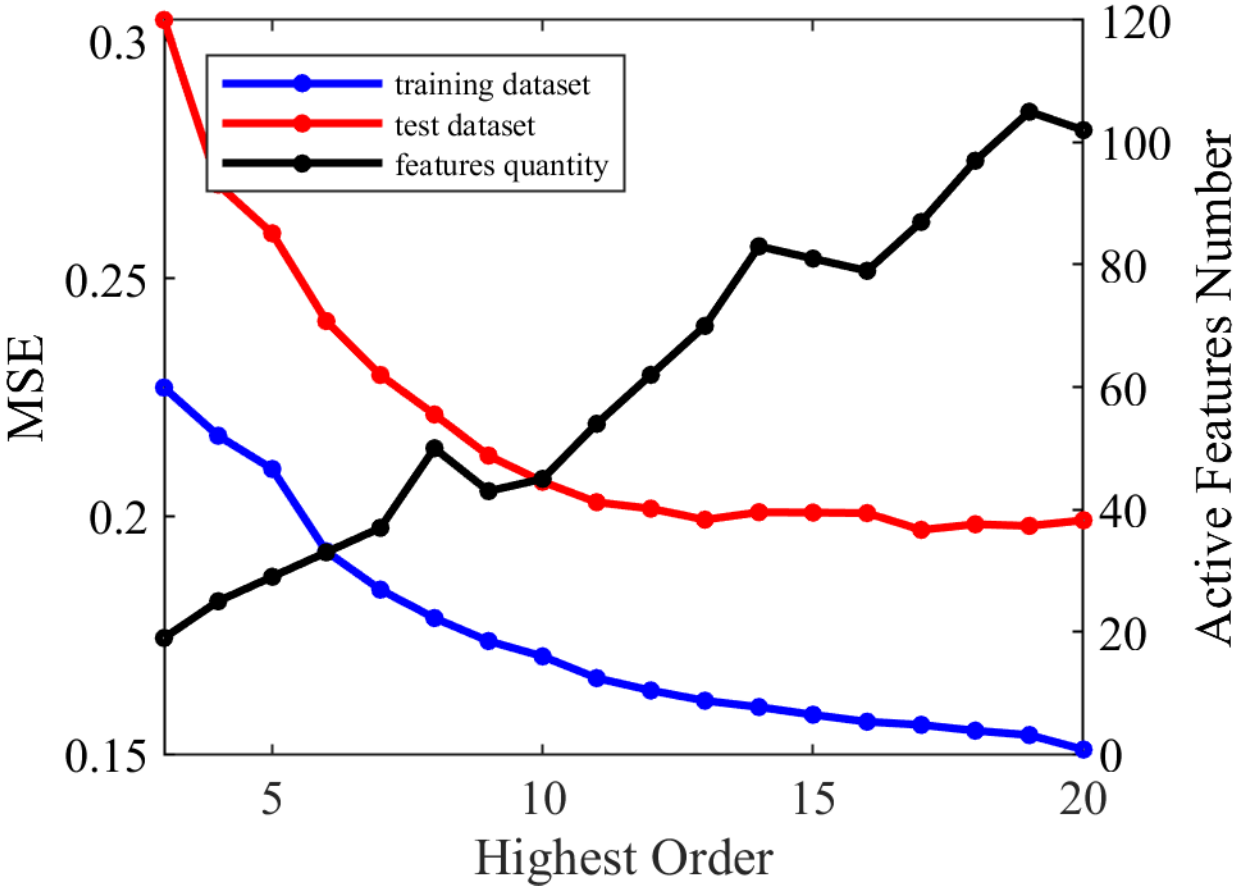

Figure 2.24: The red and blue curves illustrate the comparison of Mean Squared Error (MSE) on both the training dataset and the test dataset across different highest polynomial orders. The black curve represents the relationship between the number of active features and the various highest polynomial orders.

Based on the results presented above, the model-free motor position prediction performs much better than the model-based motor position prediction.

The Table 2.2 summarizes the mean square error (MSE) comparison results of model-

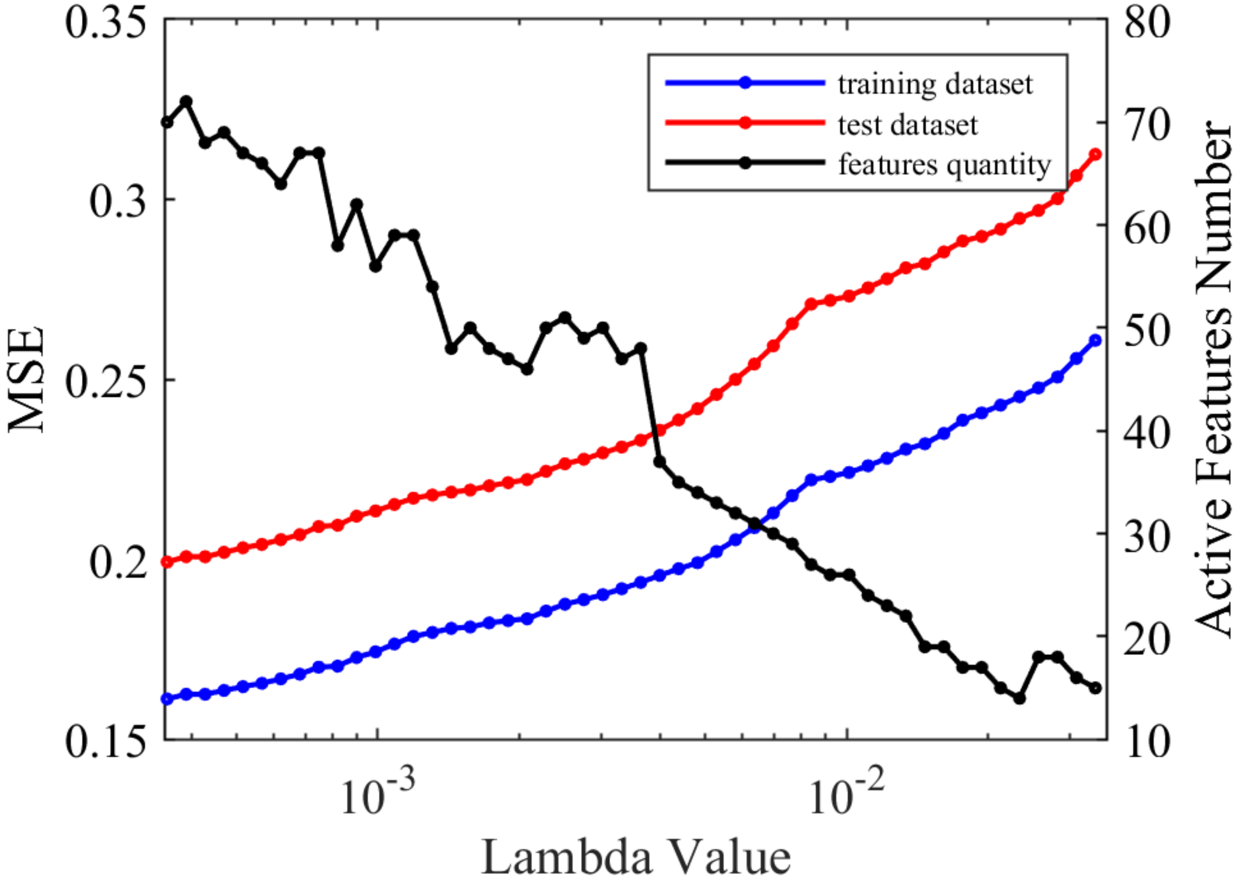

Figure 2.25: The red and blue curves illustrate the comparison of Mean Squared Error (MSE) on both the training dataset and the test dataset across different λ_d. The black curve represents the relationship between the number of active features and the various λ_d.

based and model-free data-driven force control methods. Based on the results presented, the model-free method outperform in both force prediction and motor position prediction.

Table 2.2: Model-based and Model-free Data-driven Methods MSE Comparison

	Model-based	Model-free data-driven
Force Estimation (Train)	2.65	0.20
Force Estimation (Test)	1.46	0.25
Position Estimation (Train)	1.20	0.16
Position Estimation MSE (Test)	1.60	0.20

2.6.7 Control algorithms Evaluation

The proposed control system should perform and track the desired force applied on the fingertip. Based on the comparison results of the model-based and model-free predictions, the model-free method was selected to be integrated into the final control system. The experiments were performed on the same test platforms as shown in Fig. 2.14. The readings from the load cell were treated as reference for evaluation. For each mounting position, the exoskeleton finger is required to generate static forces every Newton from 5N to 8N. According to the results shown in Fig. 2.26, even with the prediction error and the measurement error, the proposed control algorithms manage to have a stable performance. The RMSE was 0.42N for the entire experiment.

2.6.8 Slip-Grasp Force Control Policy

To control the exoskeleton glove applying force on the target object and grasp it successfully, a slip-grasp force control policy is proposed. Slip detection on the exoskeleton glove can be achieved by monitoring changes in contact forces [79]. Two methods commonly used for this

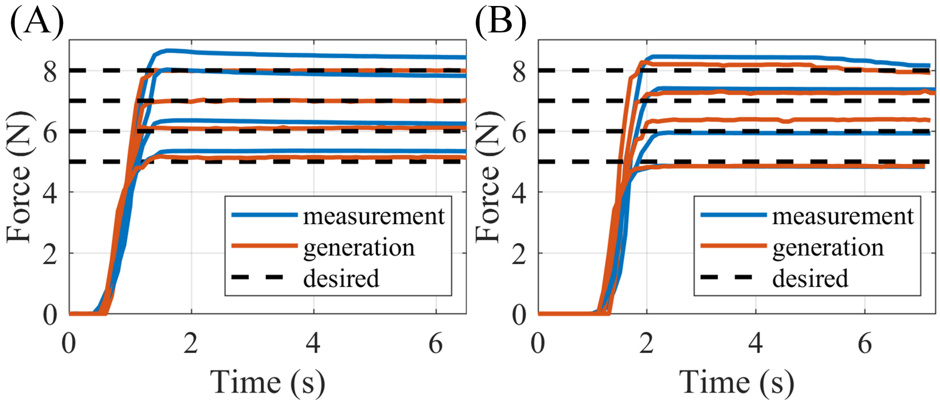

Figure 2.26: The comparison between desired force, measured force and generated force. (A) shows the experimental results on horizontal platform ($\theta_1 = 14.9°$) and (B) shows the experimental results on vertical platform ($\theta_1 = 21°$).

purpose are the use of series elastic actuators (SEAs) or force-sensitive resistors (FSRs), each with their own advantages and disadvantages.

SEAs offer consistency in detecting slip across different force levels due to the linear relationship between force and spring compression. However, the proposed linear SEA force control has an error of 0.42N, which means it is not sensitive to changes in contact force below this threshold. Additionally, slip detection using SEAs can be delayed due to the presence of backlash and friction forces.

FSRs, on the other hand, are known for their high sensitivity but have poor repeatability. As shown in Figure 2.27 (A), FSRs are capable of detecting small force changes, such as 0.2N applied to the fingertips. To leverage the advantages of both SEAs and FSRs, both of them are combined and integrated into slip detection.

The proposed Slip-Grasp force control policy utilizes slip detection based on both linear SEAs and FSRs. Slip is detected if the SEA compression changes by more than 20% or if the raw FSR reading changes by more than 10% within a timeframe of 0.3s, as demonstrated in Figure 2.27 (B).

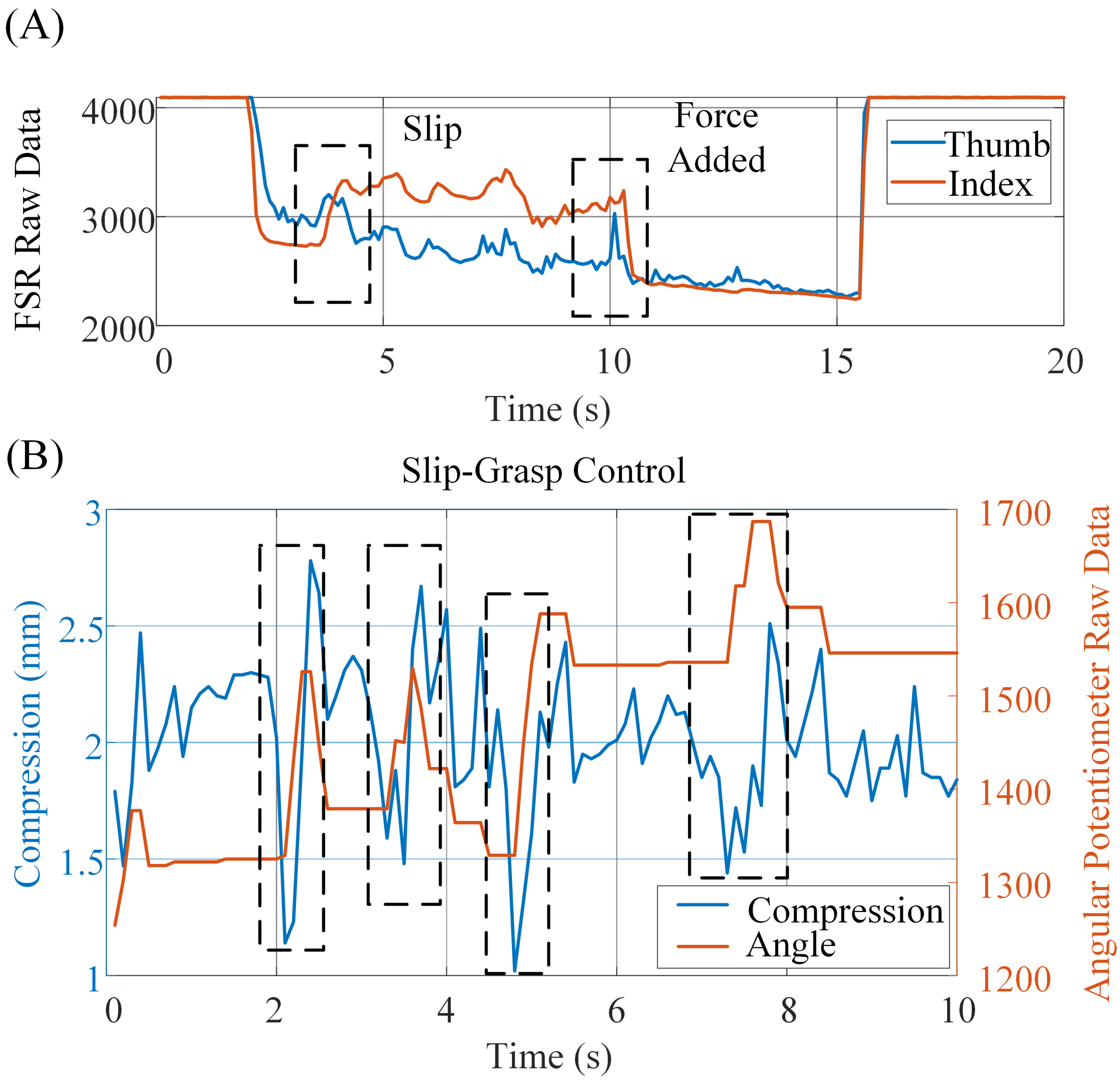

Figure 2.27: Linear SEA slip detection. (A) FSR reading while object slipping and force increment. (B) Linear SEA reading while applying slip-grasp force control policy.

2.7 Experiments

2.7.1 Experiments on Healthy Subjects

The goal of the experiments is to evaluate the performance of the whole glove system. The proposed exoskeleton glove system was developed for patients who suffer from brachial plexus injuries whose elbow and shoulder are functional, but require assistance to restore the function of the hand for ADLs. Previous research on hand taxonomy shows that there are 33 human grasp types [80]. The five most used grasp types in ADLs are selected for the experiments, which include cylinder grasp, sphere grasp, tip grasp, tripod grasp, and lateral grasp. Ten objects are selected, that belong to different grasp types for the experiments as shown in Table 2.3.

Table 2.3: Goal Objects Selection

Name	Grasp Type	Weight (g)
Bottle	Cylinder	400
Jar	Cylinder	209
Tape	Tip	15
Small Box	Tip	5
Small ball	Tip	5
Screw Driver	Tripod	48
Pen	Tripod	15
Flat Box	Lateral	142
Bowl	Lateral	316
Ball	Sphere	316

Because the model-free force prediction and compression prediction are trained based on the load cell measurements which generates the desired action force $\mathbf{y_d}$ that is normal to the contact surface, the actual desired force $\mathbf{F_d}$, which is perpendicular to the last link based on the assumption, should be converted to $\mathbf{y_d}$ as the input of the control system. Considering that the critical conversion point between two kinds of test platforms is $\theta_1 = 15.2°$ and Eqn. 19, the magnitude of $\mathbf{y_d}$ is expressed as Eqn. 30,

$$y_d = \begin{cases} \frac{F_d J_1 \sin\theta_3}{J_2} + F_d \cos\theta_3, & \theta_1 < 15.2° \\ \frac{F_d J_2 \cos\theta_3}{J_1} + F_d \sin\theta_3, & \theta_1 \geq 15.2° \end{cases} \tag{2.37}$$

where θ_3 is the angle between the last link and the x axis, J_1, J_2 are the components of the Jacobian. The similar conversion equations are applied to the other exoskeleton finger linkages. The force control is activated only if the contact is detected by the FSR sensors on the fingertips.

Three healthy subjects participated in the experiments. The experimental procedure involving human subjects in this paper was approved by the Carilion Clinic Institutional Review Board (IRB-19-330). Each of the subjects wore the exoskeleton glove and performed the grasps without any intentional finger movements. The wrist was adjusted to the best grasp position for each subject. Each object was grasped for 5 times by each participant. For each trial, the exoskeleton glove was activated by voice activation from the participant using the keywords “Hey, glove”. After receiving the feedback “activated” from the earphone, the participant should indicate the grasp type (as shown in Table 2.3) based on the goal object through voice command. After receiving another feedback “start” from the earphone, the exoskeleton glove performs the grasp based on the specific grasp type. The initial grasp force on each fingertip was set to be 2N and the force will be gradually increased by 0.5N increments if slipping of the grasped object is detected. The participants were also asked to hold the object up and shake it to show a stable grasp. When the grasp is finished, the participant should give the command “release” to let the glove return to the initial position. It is worth mentioning that the participants should adjust their elbow and shoulder position as needed to help with the grasp.

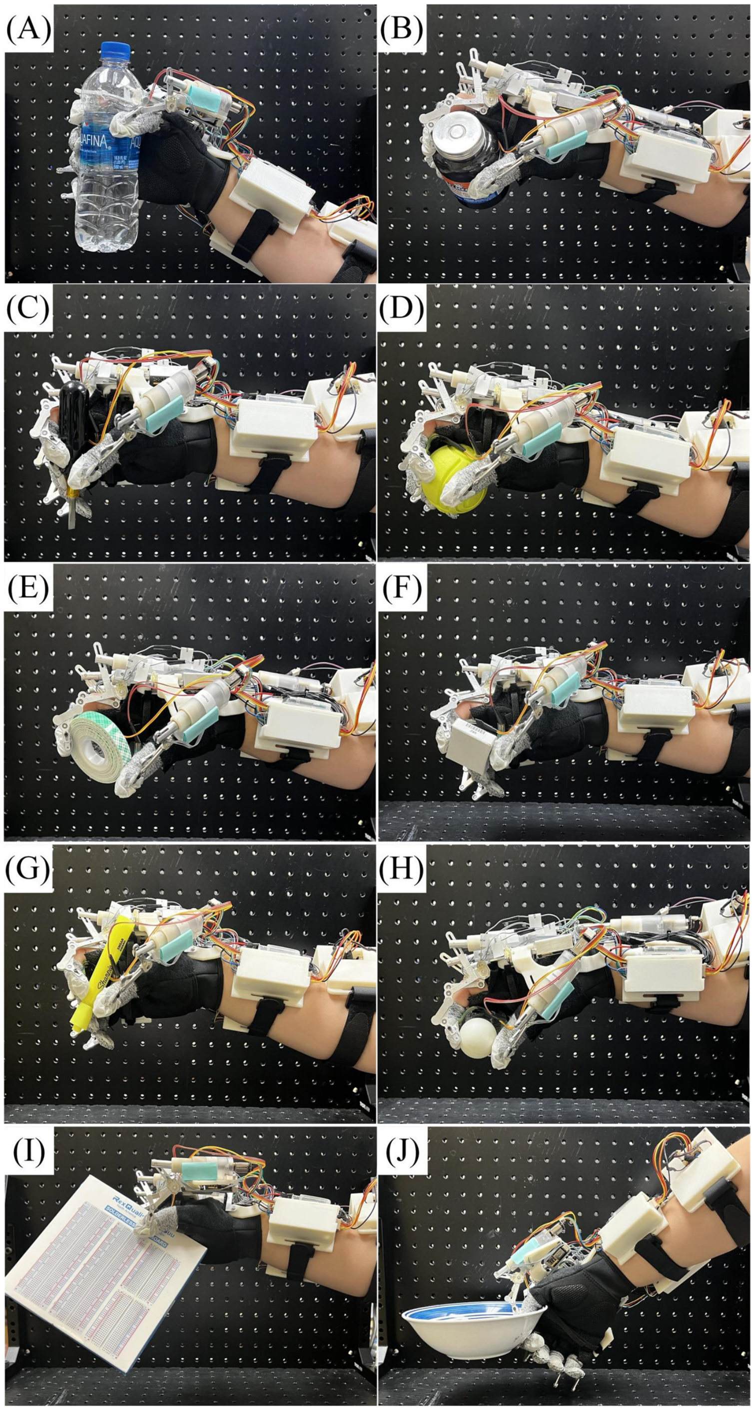

Figure 2.28: Examples of successful grasps of each object. Each object is grasped 5 times by a single participant. (A) bottle, (B) jar, (C) screw driver, (D) ball, (E) tape, (F) small box, (G) pen, (H) small ball, (I) flat box, (J) bowl.

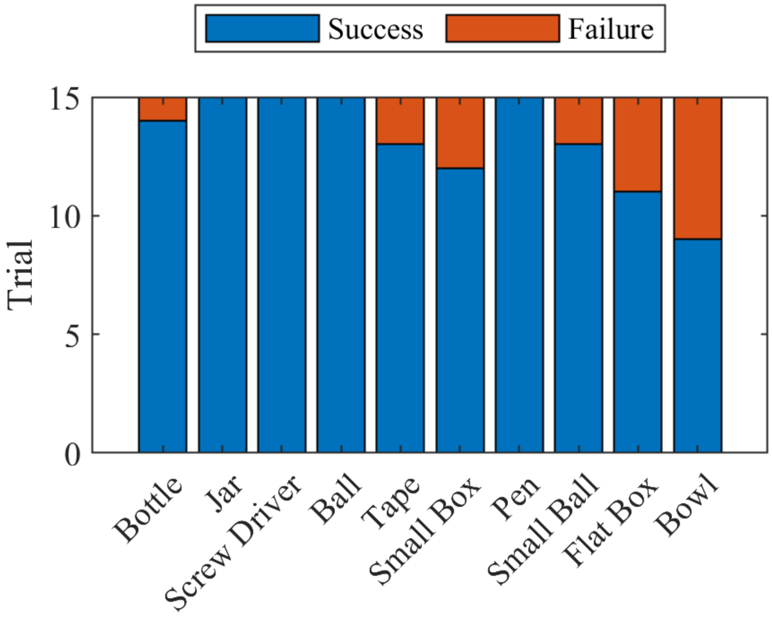

Figure 2.29: The experiment results for each objects. The flat box and bowl is hard to grasp since the lateral grasp is hard to be performed with insufficient DOF of thumb linkage.

Fig. 2.28 shows examples of successful grasps with 10 different objects. Fig. 2.29 shows the statistical results of 150 trials. The proposed exoskeleton glove system achieves a 100% success rate to grasp a jar, screwdriver, pen, and ball since they belong to the types of grasp which can be easily performed by designing a single DOF trajectory. There were 3 occasions when the bottle slipped away from the exoskeleton glove due to its smooth surface. For small objects such as a small box, tape and a small ball, the workspace of the SEA becomes the limitation. The lateral grasp (flat box and bowl) was hard to be performed because of the insufficient DOFs for the thumb motion even with adjustable thumb linkage position. The above results prove that our proposed exoskeleton glove system is able to help with the grasp of daily used objects.

2.7.2 Clinical Experiments

To comprehensively assess the performance of the proposed exoskeleton glove system, three clinical experiments are conducted involving patients with BPI. During these experiments, the patients were tasked with performing five different grasp types, as illustrated in Fig. 2.30. The results of these trials demonstrated the effectiveness of the exoskeleton glove in assisting patients with BPI in successfully grasping target objects that they previously struggled to grasp without the aid of the exoskeleton glove.

The clinical experiments provided valuable insights into the practical application and benefits of the exoskeleton glove for patients with hand disabilities. By enabling patients to perform a diverse range of grasp types, the exoskeleton glove holds the potential to significantly improve their functional capabilities and quality of life in ADLs.

2.8 Comparison with Existing Exoskeleton Glove System

To provide a comprehensive evaluation of our proposed exoskeleton glove system, eight other devices are compared with the proposed exoskeleton glove system, as summarized in Table 2.4. It is important to note that the measurements of peak fingertip force may vary among these devices, either based on their reported maximum pinch force or actual measured fingertip force.

In terms of weight, most of the devices have relatively lightweight gloves on their own. However, they require large and heavy actuation systems or workstations. Additionally, only a few devices cover all five fingers, while none of them consider the impact of wrist movement on grasping. Devices without force/torque sensing can only implement position-

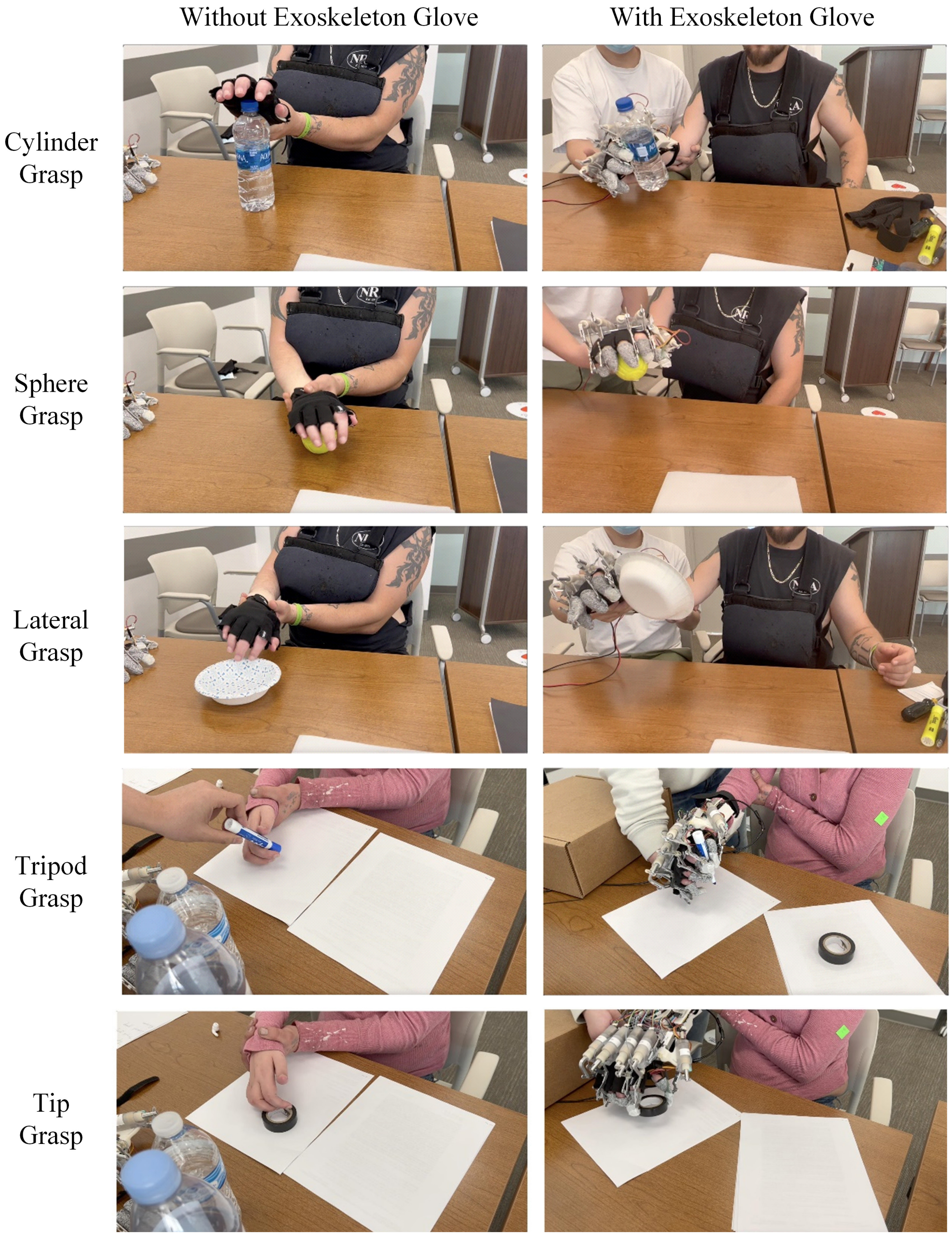

Figure 2.30: The clinical experimental results. The flat box and bowl is hard to grasp since the lateral grasp is hard to be performed with insufficient DOFs of thumb linkage.

Table 2.4: Summary of Hand Exoskeleton Grasp Assistance Systems

Device	Actuation, Transmission	Weight: glove/total	Peak Fingertip Force	Fingers	Wrist	Force/Torque Sensing	Intelligent Activation
Ryu et al.[81]	hydraulics, cable	2.62 kg / 2.74 kg	12 N	3	No	Yes	Yes
Nycz et al.[82]	linear motor, cable	113 g / 867 g	8.7 N	4	No	No	No
Gloreha Lite [83]	motor, cable	80 g / 5 kg	5 N	5	No	No	No
Hand of Hope [84]	linear motor, linkage	700 g / -	12 N	5	No	No	No
Dragusanu et al. [85]	linear motor, linkage	- / around 500 g	-	5	Yes	Yes	No
Ferguson et al. [86]	motor, cable	- / -	-	3	No	No	No
Graspy Glove [36]	motor, cable	250 g / 340 g	16 N	4	No	No	No
Agarwal et al. [45]	SEA, cable	80 g / -	-	1	No	Yes	No
KULEX Hand [34]	motor, linkage	- / 172 g	10 N	2	No	No	No
Our Glove System	**SEA, linkage**	**383 g/759 g**	**10 N**	**5**	**Yes**	**Yes**	**Yes**

based control, which is less effective for rehabilitation purposes [50, 87].

In comparison, the proposed glove system features a stable linkage-driven structure while maintaining a moderate overall weight among the compared devices. It can actuate all five fingers simultaneously and also provide coupled wrist motion to assist with grasping. The series elastic actuators (SEAs) with model-free data-driven force predictive control in our system enable the grasping of different objects with appropriate force, making it suitable for later stages of physical therapy or intelligent control.

Furthermore, our glove system incorporates personalized voice activation, enhancing the convenience of daily use for patients.

2.9 Conclusion

This chapter presented the design optimization, control, and development of an exoskeleton glove system for rehabilitating patients with brachial plexus injuries. The finger linkages of the exoskeleton glove were optimized to mimic human grasp motion, and both linear and rotaty SEAs were integrated into the linkages to provide force generation and measurement capabilities for force control. Two types of force prediction and motor position prediction algorithms, namely model-based and model-free approaches, were investigated and compared. A mathematical model for backlash was developed, and it was combined with a friction force compensation lookup table for implementation in the model-based prediction. The feature augmentation, feature matrix construction, and feature selection using LASSO regression for model-free prediction were also introduced. The Slip-Grasp force control policy was presented as well. Experimental results demonstrated that the proposed model-free prediction methods significantly improve force control accuracy.

In addition to the exploration of the algorithms, a complete prototype of the proposed exoskeleton glove system was designed and integrated with a total weight of 759 grams. To analyze the performance of the exoskeleton glove system, grasping experiments were conducted with three subjects and ten daily used objects which cover five kinds of grasp types. The results with high success rates showed that our exoskeleton glove system has the ability to complete grasping tasks for ADLs.

There are still several aspects of our glove system that could be improved upon. The reduced DOFs of the exoskeleton finger linkages limit the workspace and capability of the glove. This limitation causes difficulties in performing lateral grasps compared with other types of grasps.

Based on our current research, we believe that the proposed exoskeleton glove system is innovative and comfortable to wear due to its combination of portability and dexterity, enabled by novel actuation and control methodologies developed by our team.

Chapter 3

Modeling and Development of a Novel Low-profile Exoskeleton Glove

3.1 introduction

This chapter presents a novel, compact, low-profile, portable, and functional robotic exoskeleton glove designed specifically for patients with brachial plexus injuries. The primary focus of this research is to enhance the wearability, comfortability, and portability of robotic gloves based on the feedback from patients. A proof-of-concept prototype of the exoskeleton glove is shown in Fig. 3.1. Each finger linkage is driven by a customized linear actuator, and the rigid coupling hybrid mechanism (RCHM) is used to connect different links of each exoskeleton finger, reducing the number of degrees of freedom. The thumb motion is also taken into consideration in the design to improve wearability and comfortability.

The main contributions of this work are as follows. Firstly, a novel low-profile exoskeleton glove mechanism is proposed. Secondly, kinematic analysis and optimization-based kinematic synthesis are performed to determine the critical design parameters of the new mechanism. Thirdly, a proof-of-concept prototype is developed, and grasping experiments with various objects are conducted to evaluate the performance of the robotic glove. Compared to other hand exoskeletons, the new glove has unique characteristics, including:

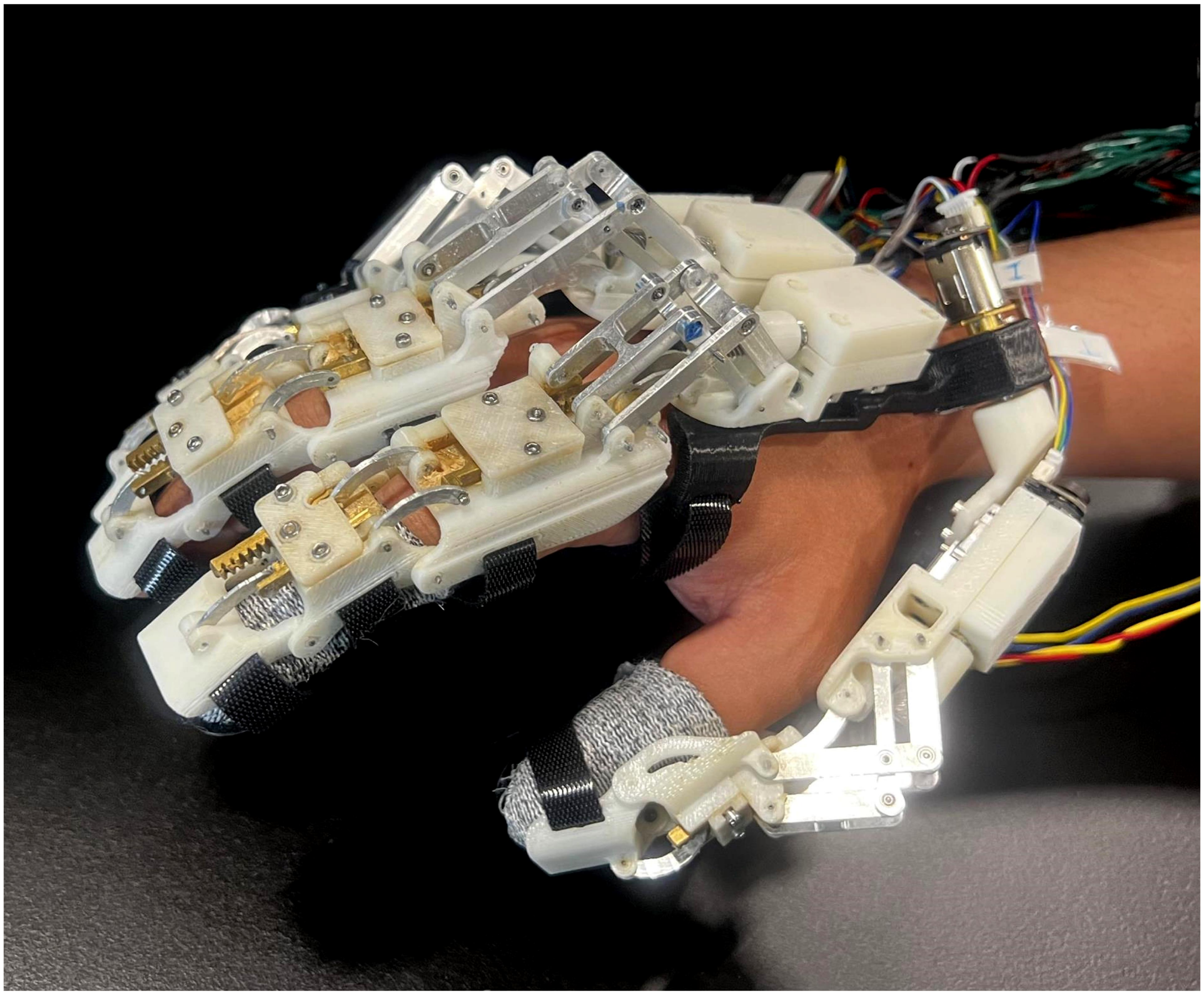

Figure 3.1: A proof-of-concept prototype of the new exoskeleton glove, which utilizes the rigid coupling hybrid mechanism (RCHM).

1. The use of a mechanically stable and robust linkage transmission mechanism, which incorporates an offset slider-crank mechanism and a rack-and-pinion mechanism.
2. The application of the RCHM concept in the finger mechanism, resulting in a low-profile and compact design.
3. The synthesis of the glove based on the imitation of actual human hand motion, leading to improved grasping performance for activities of daily living (ADLs) for patients.
4. The integration of actuators, which enhances the overall portability of the exoskeleton glove.

These contributions address the specific challenges faced by patients with brachial plexus injuries and aim to provide a more effective and user-friendly solution for hand rehabilitation.

3.2 Exoskeleton Finger Mechanism Design

This section dives into the design principles of the finger mechanism and explain the process of optimizing the motion trajectories for each finger. Additionally, final configurations of the prototype that were implemented are presented. It is worth noting that the total weight of the entire glove system, excluding electronics and batteries, amounts to 304 grams.

The proposed exoskeleton glove leverages the coupled motion between different phalanges of each finger during grasping. Building upon previous research findings [61, 62, 63], which suggest that a hand with reduced degrees of freedom (DOFs) is capable of performing most grasping motions required for activities of daily living (ADLs), the three DOFs of each finger (excluding abduction-adduction) can be simplified to just one DOF. By simplifying the exoskeleton finger to a single DOF, fewer actuators are required, resulting in a lighter glove. The proposed exoskeleton glove incorporates this concept and designs a single DOF finger mechanism based on the rigid coupling hybrid mechanism (RCHM) concept [88], using a rack-and-pinion mechanism as the rigid coupling mechanism. This unique design allows for a thin finger mechanism, improving wearability, comfortability, and portability of the glove.

The RCHM is employed to address challenges in transmitting motion within serially connected spatial mechanisms. Its core concept involves coupling the motion of each link with the subsequent link in the chain. Instead of being directly driven by the actuator, the motion of a given link is driven by its adjacent links, leading to a sequential propagation of motion from the actuator to the end link. The RCHM consists of two key components: a Parallel Mechanism (PM) that determines the fundamental mobility of the mechanism, and a Rigid Coupling Mechanism (RCM) that couples the motions of adjacent PMs. The RCM can take different forms, such as a rack-and-pinion mechanism or a four-bar mechanism, depending on the specific design requirements. In the proposed novel finger mechanism, two pairs of offset slider-crank mechanisms serve as the PM, while a rack-and-pinion mechanism serves as the RCM. Figure 3.2 depicts these two fundamental building block mechanisms of the single DOF finger mechanism.

The proposed novel exoskeleton glove is illustrated in Fig. 3.3, providing an overview of its design. The index finger exoskeleton comprises three links: a distal phalanx, a middle phalanx, and a proximal phalanx. It features three relative joints, including a distal interphalangeal (DIP) joint, a proximal interphalangeal (PIP) joint, and a metacarpophalangeal (MCP) joint. The thumb exoskeleton follows a similar structure, with the exception of the middle phalanx and DIP joint. To ensure a proper fit on the hand, each link of the exoskeleton finger corresponds to a specific phalanx on the human hand, while each joint aligns with the corresponding joint on the human hand. Additionally, a passive abduction and adduction mechanism (indicated by green arrows) is incorporated for each finger, enhancing

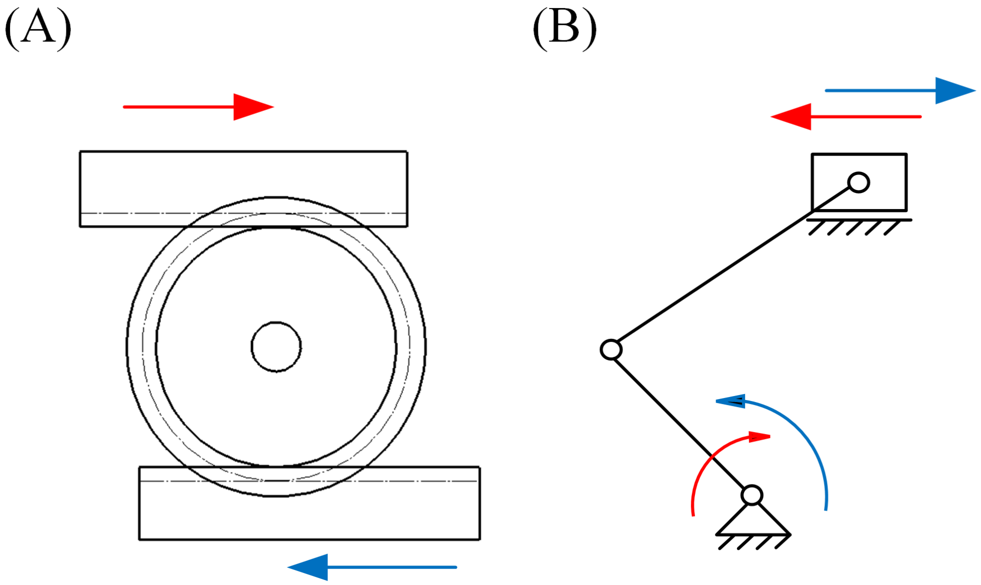

Figure 3.2: The two mechanism elements and the motions of the new finger mechanism: (A) a rack-and-pinion mechanism for motion reversing; (B) an offset slider-crank mechanism for motion conversion. The red arrow represents the input and the blue arrow represents the output.

wearer comfort during use.

The finger mechanism of the exoskeleton glove combines offset slider-crank mechanisms and rack-and-pinion mechanisms to link the different finger segments. As shown in Fig. 3.3, the principles underlying the finger mechanism are as follows:

1. A customized linear actuator, consisting of a motor and leadscrew, is driven by a DC motor located at the end. The leadscrew nut is connected to the proximal link through a connector, forming the first offset slider-crank mechanism around the MCP joint. This mechanism converts the linear motion generated by the linear actuator into rotary motion at the MCP joint, thereby driving the proximal link.
2. The housing of the linear actuator is connected to the sliding rack through another connector. This connection establishes the second offset slider-crank mechanism around the MCP joint, converting the rotary motion of the MCP joint into linear motion of

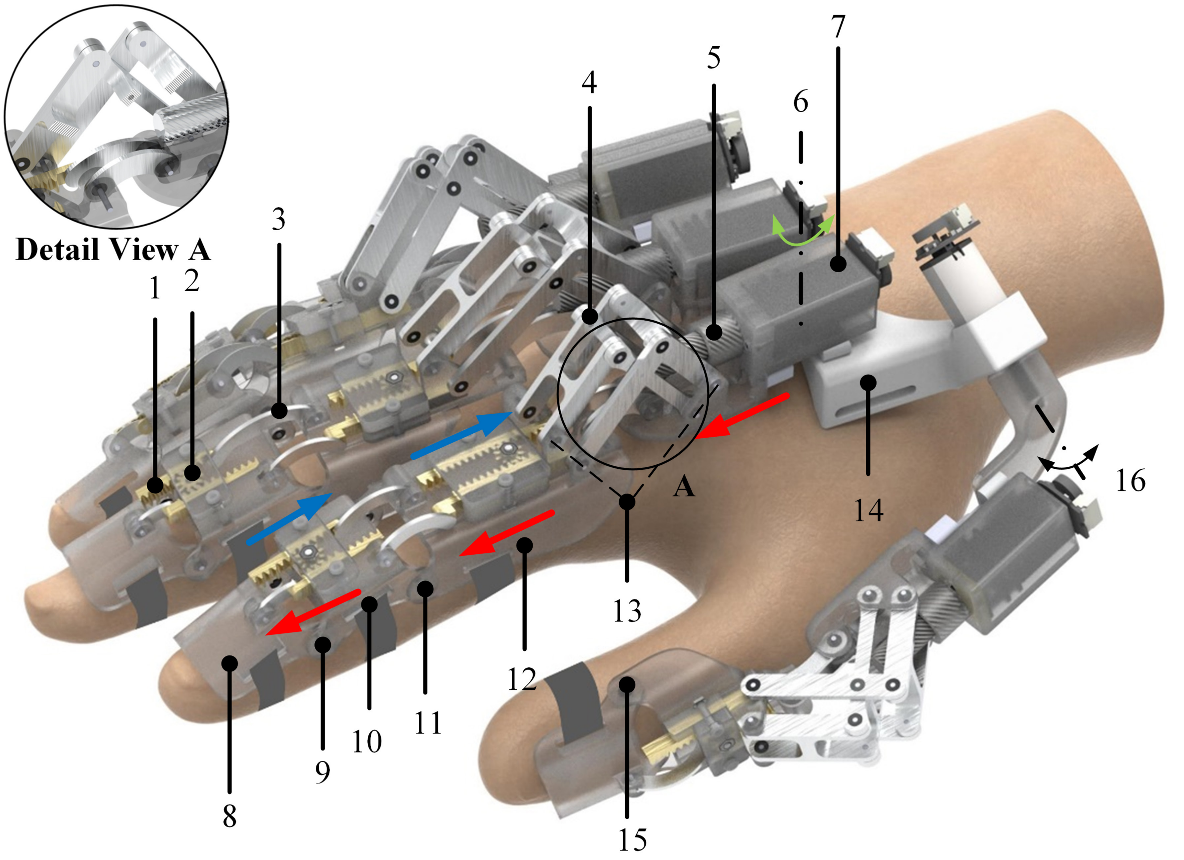

1. Rack
2. Pinion
3. Connector
4. RCM
5. Leadscrew Nut
6. Passive Abd-adduction Axis
7. DC motor
8. Distal Link
9. DIP Joint
10. Middle Link
11. PIP Joint
12. Proximal Link
13. MCP Joint (virtual)
14. Hand Base
15. IP Joint
16. Thumb Rotation Axis

Figure 3.3: Overview of the exoskeleton glove assembly. The detailed view A shows how the linear actuator is connected to the Proximal link. The red arrow shows the ”Driving” mechanism and the blue arrow shows the ”Measuring” mechanism.

the rack. Consequently, the motion generated by the linear actuator is transmitted to the linear motion of the rack on the proximal link, albeit in a different direction due to the rotation of the MCP joint.

3. To transmit the motion from the second offset slider-crank mechanism, a pinion-rack mechanism is employed to reverse the direction of motion and establish a connection between the second offset slider-crank mechanism around the MCP joint and the first offset slider-crank mechanism around the PIP joint. This coupling effectively links the motion of the MCP joint to the motion of the PIP joint.

4. The same process is repeated to transmit motion from the PIP joint to the DIP joint. Through the successive connections of the pinion-rack mechanisms and offset slider-crank mechanisms, the motion of all three joints (MCP, PIP, and DIP) on the same exoskeleton finger is coupled.

It is important to note that the MCP joint on the exoskeleton finger is virtual and replaced by a Remote Center of Motion (RCoM) mechanism to prevent interference with the patient's hand.

The first offset slider-crank mechanism, represented by the red arrow in Fig. 3.3, is called the "Driving" mechanism. It generates forward motion and drives the motion of the MCP joint in the finger mechanism. Conversely, the second offset slider-crank mechanism, represented by the blue arrow, is called the "Measuring" mechanism. It generates backward motion and its motion depends on the "Driving" mechanism, effectively measuring the output motion of the MCP joint. The rotation angle of the MCP joint, produced by the "Driving" mechanism, is measured by the "Measuring" mechanism and presented as the displacement of the rack.

A similar arrangement exists around the PIP joint, where another pair of "Driving" and

“Measuring” mechanisms are present. The rack-and-pinion mechanism connects the “Measuring” mechanism of the MCP joint to the “Driving” mechanism of the PIP joint, resulting in the coupling motion between the MCP joint and the PIP joint. The achievement of proposed sequential transmission of motion from the linear actuator to the end effector (distal link), enables coordinated and synchronized finger joints’ movements in the exoskeleton glove.

It is worth noting that there is no “Measuring” mechanism around the DIP joint since it is already connected to the last link, and its motion is directly coupled to the previous joint.

Furthermore, a passive abduction and adduction mechanism with mechanical limits is incorporated (indicated by the green arrow in Fig. 3.3). This mechanism introduces a revolute joint at the base of the actuator housing, connecting the finger linkage and the hand base. It enables comfortable movement for the patient while ensuring appropriate alignment.

This unique design allows us to make the exoskeleton finger mechanism as thin as possible and attach the whole mechanism to the top of each finger to avoid interference between the exoskeleton glove and the human hand, improving the wearability, comfortability, and portability of the glove.

3.3 Kinematic Analyses and Synthesis

Hand kinematics includes the four fingers kinematic chains and the thumb kinematic chains. Since the motion of different finger joints has similar coupling motion, their kinematics are summarized into a single formulation. The spatial kinematic chain from base to thumb Metacarpal is treated separately. One finger and thumb are used to simplify the model for illustration, as shown in Fig. 3.4.

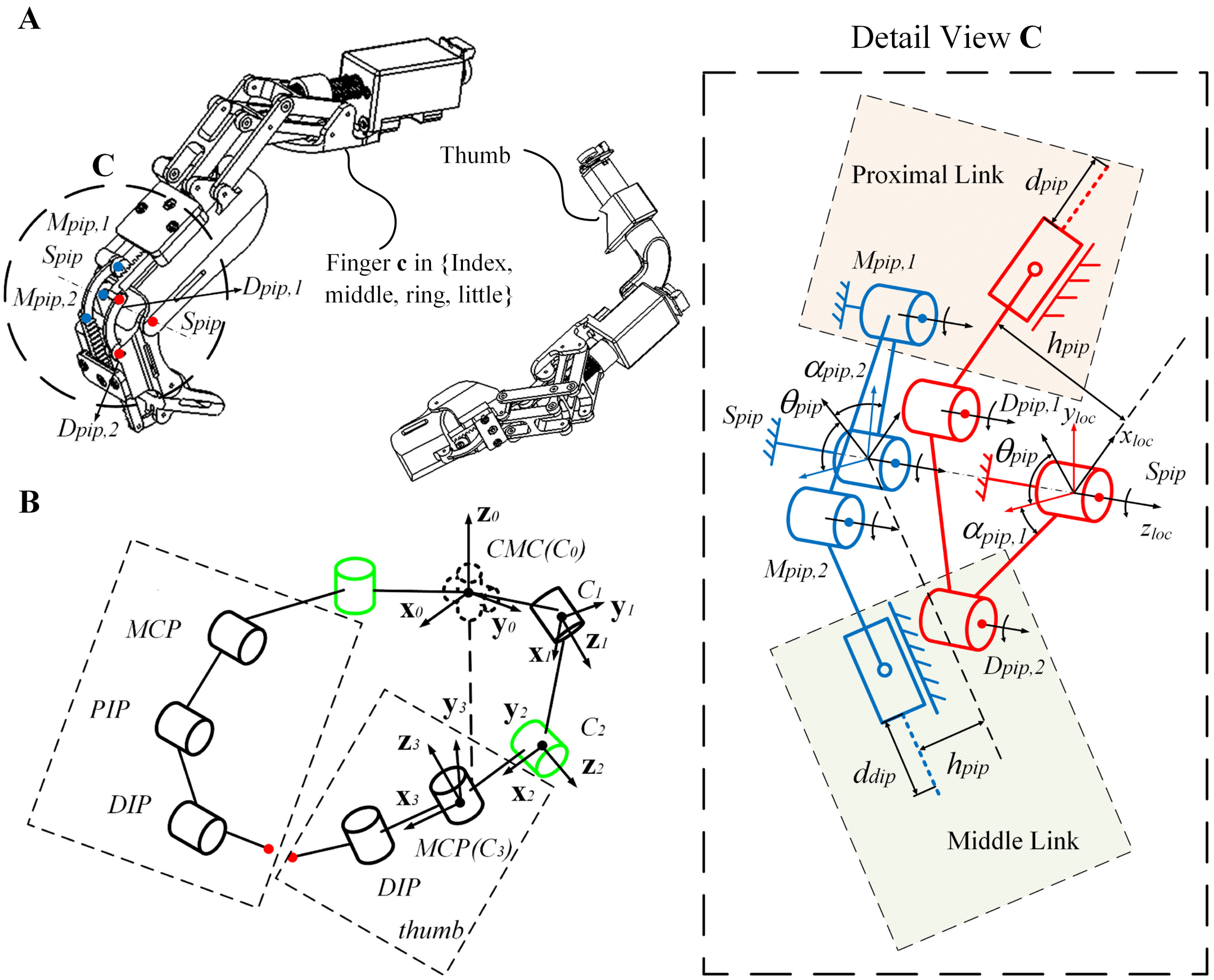

Figure 3.4: Kinematic model of the exoskeleton glove mechanism with index finger and thumb. Detail view C shows the kinematic model around the PIP joint on the index finger.

The proposed exoskeleton glove incorporates five distinct kinematic chains to accommodate different digits. Among them, the four fingers exhibit similar coupled planar motion, allowing their kinematics to be represented by a unified formulation. On the other hand, the kinematic chain of the thumb takes both the coupled planar motion and the spatial motion around the Carpo-Metacarpa (CMC) joint into account. By considering these variations, the exoskeleton glove achieves comprehensive control over the hand movements, accommodating the unique kinematics of each digit [89, 90].

3.3.1 Finger Linkage Kinematic Analysis

For the finger linkage kinematic analysis, the forward kinematic chain of the current finger c is given by Eqn. 3.1:

$$p_{x,c} + ip_{y,c} = l_{p,c}e^{i\theta_{mcp,c}} + l_{m,c}e^{i(\theta_{mcp,c}+\theta_{pip,c})} + l_{d,c}e^{i(\theta_{mcp,c}+\theta_{pip,c}+\theta_{dip,c})} \tag{3.1}$$

where $c \in \{index, middle, ring, little\}$ represents the current finger, $p_{x,c}$, $p_{y,c}$ are the x and y coordinates of the exoskeleton fingertip position in the finger motion plane. $\theta_{mcp,c}$, $\theta_{dip,c}$, and $\theta_{pip,c}$ are the rotating angles of the MCP joint, the PIP joint, and the DIP joint on the current exoskeleton finger, respectively. $l_{p,c}$, $l_{m,c}$ and $l_{d,c}$ are the lengths of the Proximal link, the Middle link, and the Distal link on the current exoskeleton finger, respectively.

The kinematic model of the proposed finger exoskeleton mechanism consists of two and a half pairs of serially connected "Driving" and "Measuring" chains as discussed in Section 3.2. Since both the "Driving" and the "Measuring" chains of each pair perform the same rotation around the corresponding finger joint, the following relationship can be obtained:

$$A_{c,jnt,i} = \sqrt{B^2_{c,jnt,i} - C^2_{c,jnt,i}} + D_{c,jnt,i} - E_{c,jnt,i} \tag{3.2}$$

where,

$$A_{c,jnt,i} = (l_{c,jnt,i} - d_{c,jnt}) \cos \alpha_{c,jnt,i} \tag{3.3}$$

$$B_{c,jnt,i} = l^2_{c,jnt,i} \cos \alpha_{c,jnt,i} \tag{3.4}$$

$$C_{c,jnt,i} = h^2_{c,jnt}(\cos \alpha_{c,jnt,1} - \cos(\alpha_{c,jnt,i} + \theta_{c,jnt})) \tag{3.5}$$

$$D_{c,jnt,i} = h_{c,jnt} \sin \alpha_{c,jnt,i} \tag{3.6}$$

$$E_{c,jnt,i} = h_{c,jnt} \cos(\alpha_{c,jnt,i} + \theta_{c,jnt}) \tag{3.7}$$

and $c \in \{index, middle, ring, little\}$, $jnt \in \{mcp, pip, dip\}$, $i \in \{1, 2\}$. Subscript $i = 1$ refers to the “Driving” chain and subscript $i = 2$ refers to the “Measuring” chain. l is the length of the connector, h is the distance between the joint and the middle plane of the rack, and α is the angle of the crank.

The kinematics of the human thumb involves three phalanges: the Proximal phalanx, the Distal phalanx, and the Metacarpal phalanx. The motion of the Proximal and Distal phalanges can be captured using the finger linkage kinematics described earlier, as they exhibit planar motion.

3.3.2 Thumb Kinematic Analysis

The human thumb consists of three links, which are the Proximal link, the Distal Link, and the Metacarpal link. The kinematics of the Proximal and Distal links are covered by the finger linkage kinematics (dashed block in Fig. 3.4), which are connected with the Interphalangeal (IP) and the MCP joint, both having one degree of freedom (DOF). Hence, this section mainly focuses on the kinematics from the Carpus to the Metacarpal link.

The Metacarpal link connects to the Carpus through the CMC joint, which provides two DOFs. To mimic the functionalities of the CMC joint, the exoskeleton glove uses two independent revolute joints ($C1$ and $C2$) as shown in Fig. 3.4. It's important to note that the second revolute joint ($C2$) is designed to be passive to maintain consistency with other finger exoskeletons.

As the CMC joint on the thumb and the CMC joint on the index finger are closely attached, the CMC (C_0) joint on the thumb is chosen as the origin of the global coordinates. Each link frame $\sum C_j := (C_j, \mathbf{x}_j, \mathbf{y}_j, \mathbf{z}_j)$, $(0 \leq j \leq 3)$, is defined at the joint j axis, where $\mathbf{z}_j$ coincides with the joint j axis, and $\mathbf{x}_j$ points to the next joint. The forward kinematics from the CMC joint on the hand to the MCP joint on the thumb can then be expressed as follows:

$$\mathbf{R}_{C_j} = \mathbf{R}_{C_{j-1}} \mathbf{R}_z(\beta_{C_j,z}) \mathbf{R}_y(\beta_{C_j,y}) \mathbf{R}_x(\beta_{C_j,x}) \mathbf{R}_z(\theta_{C_j}) \tag{3.8}$$

$$\mathbf{p}_{C_j} = \mathbf{R}_{C_{j-1}} \mathbf{p}_{C_{j-1},C_j} + \mathbf{p}_{C_{j-1}} \tag{3.9}$$

where $\mathbf{R}_{C_j}$ denotes the orientation of the frame $\sum C_j$, $\mathbf{R}_x(\cdot)$, $\mathbf{R}_y(\cdot)$, and $\mathbf{R}_z(\cdot)$ denote the principle rotation matrix functions with respect to the corresponding axis, $\boldsymbol{\beta}_{C_j} = [\beta_{C_j,x} \ \beta_{C_j,y} \ \beta_{C_j,z}]^T$ denotes the vector of rotation angles with respect to the corresponding axis, θ_{C_j} denotes the rotation angle of the joint C_j, $\mathbf{p}_{C_j}$ denotes the C_j position, $\mathbf{p}_{C_{j-1},C_j}$ denotes the vector from C_{j-1} to C_j. For the initial conditions, $\mathbf{R}_{C_0}$ is the identity matrix, θ_{C_0} is zero, $\mathbf{p}_{C_0}$ and $\boldsymbol{\beta}_{C_0}$ are zero vectors.

3.3.3 Kinematic Synthesis

The finger mechanism requires proper alignment of joint axis on the exoskeleton and the joint axis on the human finger. However, due to the significant size and shape variations among individuals, an optimization process is conducted based on the finger dimensions provided by the author, as indicated in Table 3.1. It is worth mentioning that the thumb does not have a middle link, and the parameter l_c for four fingers are ignored in the optimization process, as it has minimal impact on the finger motion.

Table 3.1: Finger Dimensions

Name	l_c (mm)	l_p (mm)	l_m (mm)	l_d (mm)
thumb	52.0	36.0	-	34.0
index	-	50.0	27.2	26.4
middle	-	57.0	35.4	24.2
ring	-	55.1	33.0	24.6
little	-	44.7	25.4	24.0

The design of the exoskeleton glove aims to replicate the natural grasping motion of the human hand. To achieve this, the design variables of the exoskeleton glove are optimized based on the UNIPI dataset [91], which provides joint trajectories of the fingers during grasping motions. Specifically, the finger joint data from the No. 1 subject while grasping the No. 8 object is selected, as it contains long trajectories of joint motion, thus expanding the exoskeleton glove's workspace.

Since the selected trajectories cover both grasping and releasing motions and contain thousands of data points, preprocessing is performed to extract only the grasping motion. From the grasping data, four equally distributed positions along the trajectory are chosen as landmarks. Each landmark is defined by fifteen joint angles (three distinct joints on each digit), which characterize the hand's posture.

The objective function is formulated as the weighted sum of the root mean squared error (RMSE) between the joint angles of the landmarks and the corresponding joint angles of the exoskeleton fingers. The RMSE is calculated for each joint angle, resulting in a vector $\mathbf{e} \in \mathbb{R}^{60\times 1}$. The weights $\mathbf{w}_k \in \mathbb{R}^{1\times 15}$ are assigned to each joint angle of the k-th landmark, and they reflect the importance of each landmark in the optimization. The objective function Z is defined as:

$$Z = [\mathbf{w}_1 \quad \mathbf{w}_2 \quad \mathbf{w}_3 \quad \mathbf{w}_4]\mathbf{e} \tag{3.10}$$

The selection of weights for the MCP, PIP, and DIP joints considers the different range of motion of each joint and its relationship with the adjacent joints. This allows the optimization to consider the relative importance of each joint angle in achieving a more accurate replication of the human motion trajectory [92],

$$0^\circ \leq \theta_{mcp} \leq 90^\circ \tag{3.11}$$

$$0^\circ \leq \theta_{pip} \leq 110^\circ \tag{3.12}$$

$$0^\circ \leq \theta_{dip} \leq 90^\circ \tag{3.13}$$

After several experiments, we chose the equally weights for different positions and different weights for each joint ($\mathbf{w}_1 = \mathbf{w}_2 = \mathbf{w}_3 = \mathbf{w}_4$).

For the finger linkage mechanism, additional nonlinear inequality constraints are introduced to incorporate the rack-and-pinion mechanisms. These constraints ensure that the motion of the rack and the rotation of the pinion are properly synchronized. The specific form of these constraints depends on the geometric characteristics and design parameters of the rack-and-pinion mechanism used in the exoskeleton glove.

$$2d_{pip} \leq l_p - h_{mcp}cos(\alpha_{mcp,1}) - h_{pip}\cos(\alpha_{pip,2}) \tag{3.14}$$

$$2d_{dip} \leq l_m - h_{pip}\cos(\alpha_{pip,1}) - h_{dip}\cos(\alpha_{dip,2}) \tag{3.15}$$

$$h_{pip} \leq h_{mcp} \tag{3.16}$$

$$h_{dip} \leq h_{pip} \tag{3.17}$$

The five digits are optimized together to achieve a better performance. The optimization problem is solved by the MATLAB function `fmincon` with the “interior-point” algorithm. The optimized design variables are collected in Table 3.2.

3.4 Hardware Development

Based on the synthesized results, a proof-of-concept prototype exoskeleton glove was designed and manufactured. Each link of the exoskeleton finger is 3D printed using acrylonitrile butadiene styrene (ABS). The connectors are made out of 6061T6 aluminum alloy. The racks and pinions are manufactured by customizing off-the-shelf 0.5 modulus brass gears and racks. The linear actuators are customized using a leadscrew (lead=20mm, starts=16, pitch diameter=5.5mm, thread angle=30°, lead angle=49.27°) and a direct current (DC) motor with gearbox that provides a torque constant of 980 $\text{N}\cdot\text{mm}$, a normal speed of 35 RPM, and a $1000:1$ reduction ratio. 681 miniature bearings are used for all the rotating joints. Each link is attached with Velcro to bind it securly on the patient’s finger. The total mass of the prototype is 304 grams.

Table 3.2: Optimized Design Variables

Index Finger				Middle Finger			
Variable	Value	Variable	Value	Variable	Value	Variable	Value
$l_{mcp,1}$	13.0 mm	$l_{mcp,2}$	13.9 mm	$l_{mcp,1}$	20.0 mm	$l_{mcp,2}$	19.3 mm
$l_{pip,1}$	15.0 mm	$l_{pip,2}$	15.6 mm	$l_{pip,1}$	14.3 mm	$l_{pip,2}$	21.7 mm
$l_{dip,1}$	8.2 mm	h_{mcp}	16.7 mm	$l_{dip,1}$	12.0 mm	h_{mcp}	14.3 mm
h_{pip}	10.0 mm	h_{dip}	10.0 mm	h_{pip}	10.0 mm	h_{dip}	10.0 mm
$\alpha_{mcp,1}$	17.1 deg	$\alpha_{mcp,2}$	22.3 deg	$\alpha_{mcp,1}$	17.8 deg	$\alpha_{mcp,2}$	17.2 deg
$\alpha_{pip,1}$	24.6 deg	$\alpha_{pip,2}$	30.0 deg	$\alpha_{pip,1}$	29.4 deg	$\alpha_{pip,2}$	30.0 deg
$\alpha_{dip,1}$	45.0 deg			$\alpha_{dip,1}$	47.1 deg		
Ring Finger				Little Finger			
$l_{mcp,1}$	17.2 mm	$l_{mcp,2}$	17.8 mm	$l_{mcp,1}$	13.4 mm	$l_{mcp,2}$	13.1 mm
$l_{pip,1}$	12.2 mm	$l_{pip,2}$	19.5 mm	$l_{pip,1}$	12.2 mm	$l_{pip,2}$	13.0 mm
$l_{dip,1}$	12.2 mm	h_{mcp}	16.0 mm	$l_{dip,1}$	11.2 mm	h_{mcp}	16.0 mm
h_{pip}	10.0 mm	h_{dip}	10.0 mm	h_{pip}	10.0 mm	h_{dip}	10.0 mm
$\alpha_{mcp,1}$	18.0 deg	$\alpha_{mcp,2}$	19.7 deg	$\alpha_{mcp,1}$	17.8 deg	$\alpha_{mcp,2}$	17.2 deg
$\alpha_{pip,1}$	25.8 deg	$\alpha_{pip,2}$	30.0 deg	$\alpha_{pip,1}$	22.1 deg	$\alpha_{pip,2}$	30.0 deg
$\alpha_{dip,1}$	45.0 deg			$\alpha_{dip,1}$	45.0 deg		
Thumb							
$l_{mcp,1}$	14.9 mm	$l_{mcp,2}$	20 mm	$l_{dip,1}$	15.9 mm	h_{mcp}	16.1 mm
h_{dip}	10.0 mm	$\alpha_{mcp,1}$	17.2 deg	$\alpha_{mcp,2}$	10.0 deg	$\alpha_{dip,1}$	30.0 deg
$p_{C_0,C_1,x}$	-14.8 mm	$\beta_{C_1,x}$	-154.5 deg	$p_{C_0,C_1,y}$	10.1 mm	$\beta_{C_1,y}$	-170.2 deg
$p_{C_0,C_1,z}$	16.3 mm	$\beta_{C_1,z}$	-128.8 deg	$p_{C_1,C_2,x}$	2.9 mm	$\beta_{C_1,x}$	115.7 deg
$p_{C_1,C_2,y}$	-24.0 mm	$\beta_{C_1,y}$	170.4 deg	$p_{C_1,C_2,z}$	-18.6 mm	$\beta_{C_1,z}$	38.6 deg
l_{C_2,C_3}	40.0 mm						

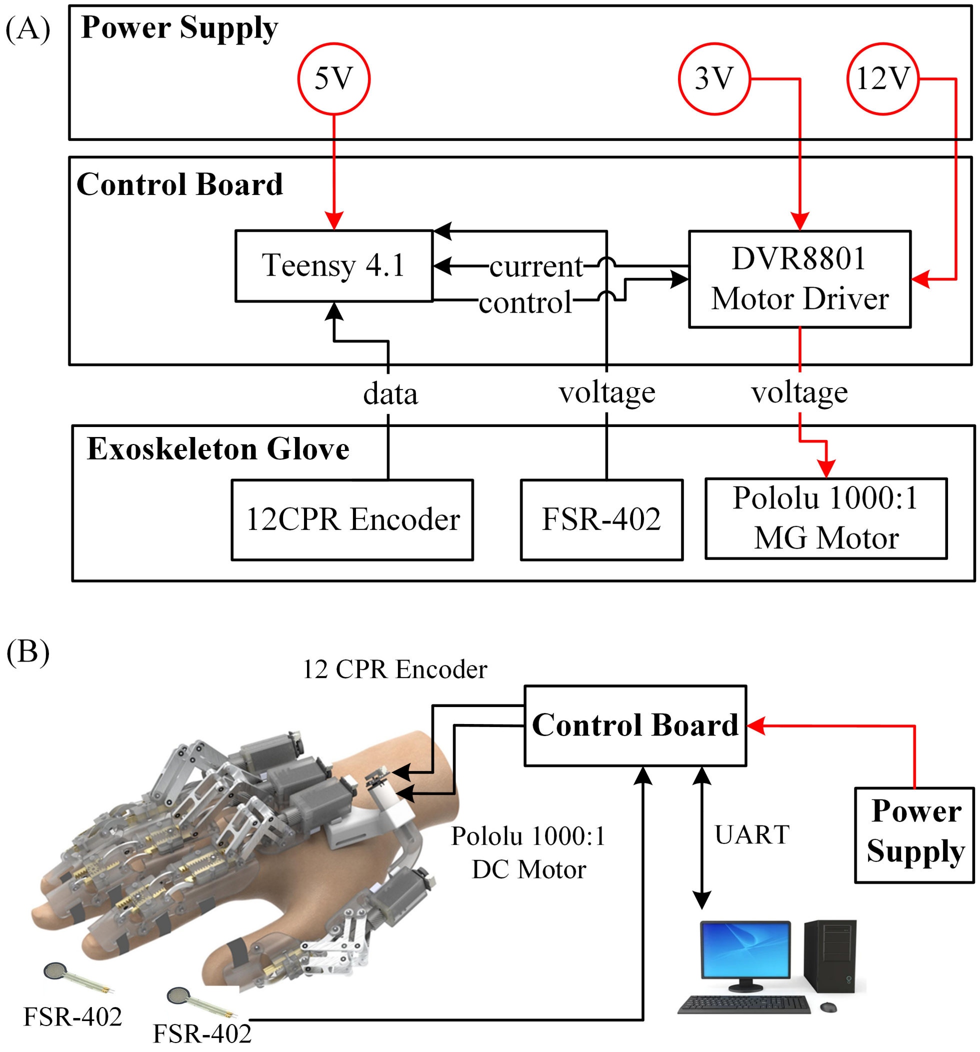

Figure 3.5: (A) Electronics block diagram. (B) Rendered exoskeleton glove with electronics.

Fig. 3.5. illustrates the electronics block diagram of the system. The electronics system is divided into three parts. The first part comprises power supply units that provide 3V, 5V, and 12V voltage output.

The second part is the control board, consists of a Teensy 4.1 microcontroller and seven DVR8801 motor drivers. The onboard Teensy 4.1 microcontroller handles sensor readings and performs various low-level control tasks, such as motor current control, motor force control, and motor PID position control. To minimize sensor reading latency and enable parallel computing, a real-time system is employed. The microcontroller communicates with a desktop computer to perform deep reinforcement learning.

Third, the exoskeleton glove uses six dual-shaft 12V 1000:1 Pololu metal gear motors to produce sufficient power and torque to generate motion in the proposed exoskeleton glove (one for each finger and one for the thumb thenar). Each motor is paired with a DVR-8801 motor driver and 12-CPR magnetic encoders. The electrical current consumption of the motor can be measured using the DVR-8801 motor driver. We use a 5^{th} order low-pass butter-worth filter with a 2Hz cut-off frequency to filter the measured current. Two Interlink fsr-402 force sensitive resistors (FSRs) are placed on wearable finger sleeves on the thumb and index finger. Both FSRs are connected to a 3.3V voltage source with a 100kΩ pull-down resistor, which can measure the contact force from 0N to 4N using a 3V, 12-bit ADC bus.

3.5 Control

Given that the proposed exoskeleton glove lacks highly accurate force sensors on each finger, achieving precise force control poses a challenge. Instead, the force outputs of the actuators are indirectly managed by regulating the electrical current consumed by the motors. Additionally, to detect contact and provide approximate measurements of contact forces for the control policy introduced in Chapter 4, two FSRs are calibrated and affixed to the fingertips of the index finger and thumb. This section will delve into the conversion process from current to force.

To perform the linear actuator current-force conversion, we placed a load cell to measure the force exerted by the last linkage of the middle finger mechanism (see Fig. 3.6 A). Force is measured by the load cell in the perpendicular direction to the ground. The measured force on the load cell can be modeled using Eq. 3.18

$$F_{lc} = F_m \cdot R(p) \cdot \cos\theta \tag{3.18}$$

where F_{lc} denotes the force measured by load cell, F_m denotes the force output by linear actuator, $R(p)$ denotes the actuator to fingertip linkage force transformation ratio as a function of actuator position, θ denotes the angle between load cell and fingertip linkage.

The actuator can be calibrated by mapping the current consumption I to the actuator output force F_m. I can be measured directly by the motor controller. F_m can be calculated using Eq. 3.18, where actuator to fingertip force transformation ratio is a function of the actuator position shown in Fig. 3.6 B. The encoder measures the actuator position p, and θ is measured by hand. 135 current - force data pairs are collected at different angles to perform the fitting and use 90 pairs to validate the result. The fitting result is shown in Fig. 3.6 C. The calibration achieved an average force difference of 21.15% mean absolute percentage error (MAPE) at the fingertip linkage. The actuator can output around 13.5N and 1.6N—2.76N to fingertip linkage based on different linkage angle.

For the purpose of rotatory actuator current-torque conversion, a load cell was positioned to quantify the force applied by the thumb mechanism (as depicted in Figure 3.7 A). The load cell measures force in the direction perpendicular to the ground. The force measured

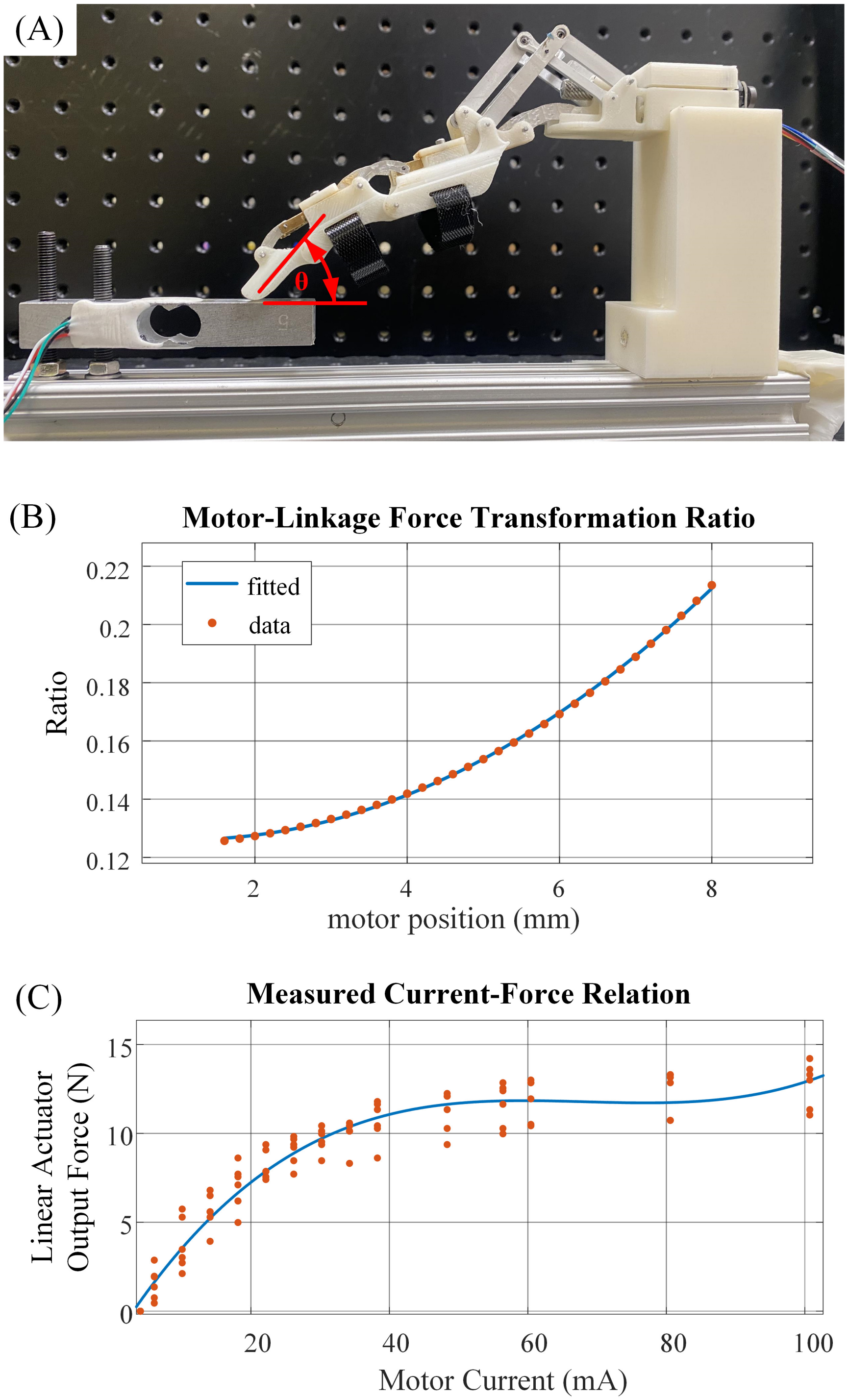

Figure 3.6: Current – force conversion experiment when $\theta = 49.7°$. (A) Experiment platform. (B) Force transformation ratio as a function of linear actuator position. (C) Linear actuator output force as a function of motor current consumption.

by the load cell is used to calculate the torque using Equation 3.19.

$$\tau_t = F_{lc} \cdot \cos(\theta) \cdot r \tag{3.19}$$

Where F_{lc} is the force measured by load cell τ_t represents the torque output by rotatory actuator, θ represents the angle between ground plane and rotatory actuator rotational axis, and r represents rotatory actuator leverage.

The actuator can be calibrated by mapping the current consumption I to the actuator output force τ_t. I can be measured directly by the motor controller. τ_t can be calculated using Eq. 3.19, where $\theta = 38.2°$ is measured by the model in SolildWorks and r is measured by hand. 64 pairs of force-current data are collected at different rotation angles with different r to perform the fitting and additional 48 pairs to validate the result. The fitting results are shown in Fig. 3.7 (b). The calibration achieved an average torque difference of 10.25% mean absolute percentage error (MAPE) and the maximum actuator output torque is $37\text{N} \cdot \text{cm}$.

Two FSRs are strategically positioned, with one affixed to the fingertips of the index finger and the other located on the inner side of the thumb. These particular locations were selected due to the involvement of these two digits in all kinds of grasp types. The FSRs fulfill roles in assisting with force sensing, contact detection, and slip detection. The calibration procedure for the FSRs involves employing weights of 25g, 50g, 100g, and 200g. Each weight is successively applied to both FSRs twenty times, and the resulting average Analog-to-Digital Converter (ADC) reading is recorded for each trial. The resulting calibration curve, graphically illustrated in Fig. 3.8, illustrates the functional relationship between the exerted force and the corresponding ADC readings.

The low-level control is implemented on the Teensy 4.1 micro-controller with FreeRTOS, and its primary functions include parsing the force command received from the high-level

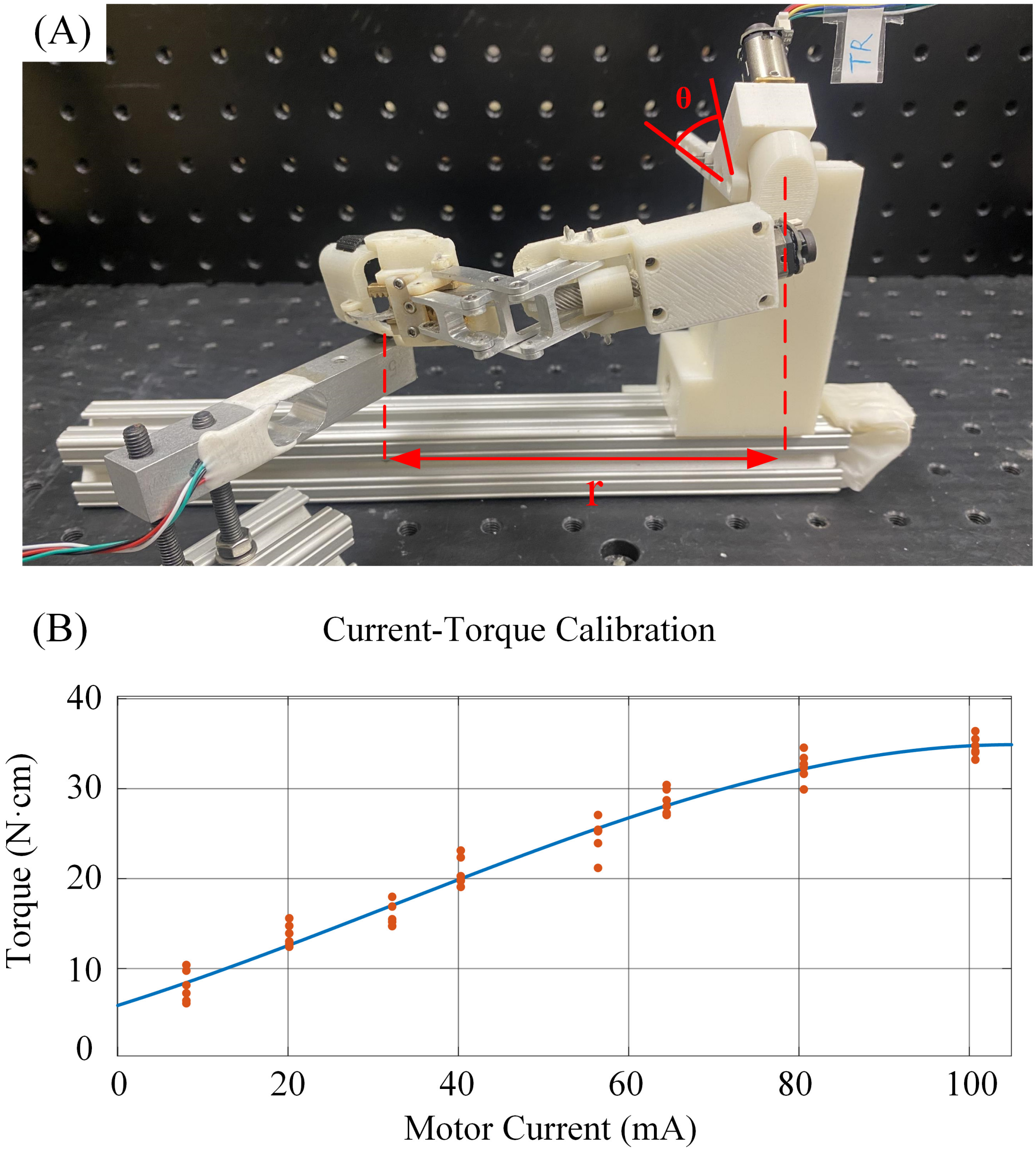

Figure 3.7: Current – torque conversion for the rotatory actuator. (A) Experiment platform. (B) Actuator output torque as a function of motor current consumption.

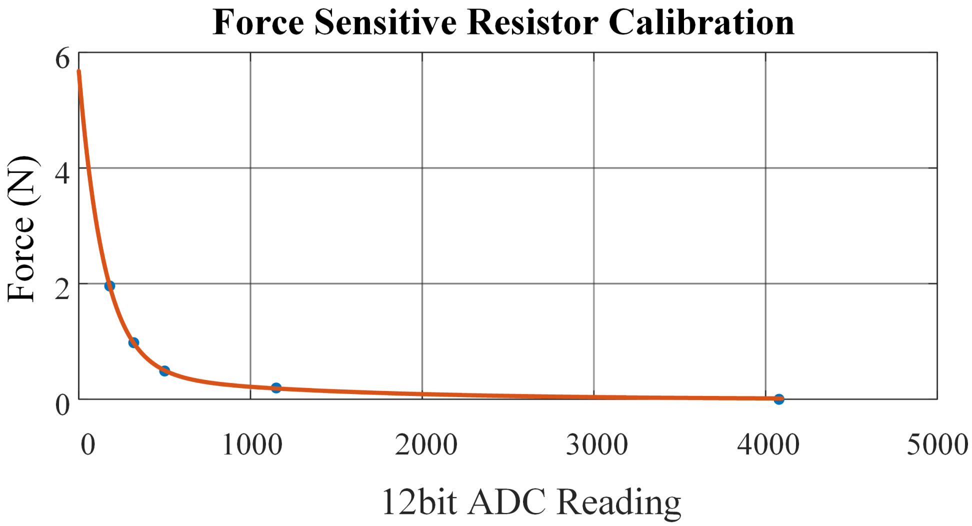

Figure 3.8: Force calibration for FSR-402 force sensitive resistor.

controller, generating the desired force output for each actuator, and transmitting sensor feedback to the high-level controller. The structure of the low-level controller is illustrated in Fig. 3.9, which consists of four threads: (1) Communication Thread: This thread facilitates the exchange of data between the high-level controller and the low-level controller. (2) Motor Control Thread: Responsible for running the motor current PID controller and motor position PID controller, ensuring precise motor control. (3) Force Control Thread: Executes the motor current-force calibration, enabling accurate force control. (4) Sensor Thread: Collects sensor data and applies a bandpass filter to reduce sensor noise, ensuring reliable and accurate measurements.

The high-level controller is responsible for executing a deep deterministic policy gradient (DDPG) reinforcement learning agent, which is extensively elaborated upon in Chapter 4. The training of this DDPG agent has been carried out within the MATLAB Simscape simulation environment, as comprehensively detailed in Section 4.2. The control structure is depicted in Fig. 3.10. This DDPG agent is operational on a desktop computer, where it acquires observations from the low-level controller and subsequently communicates back the

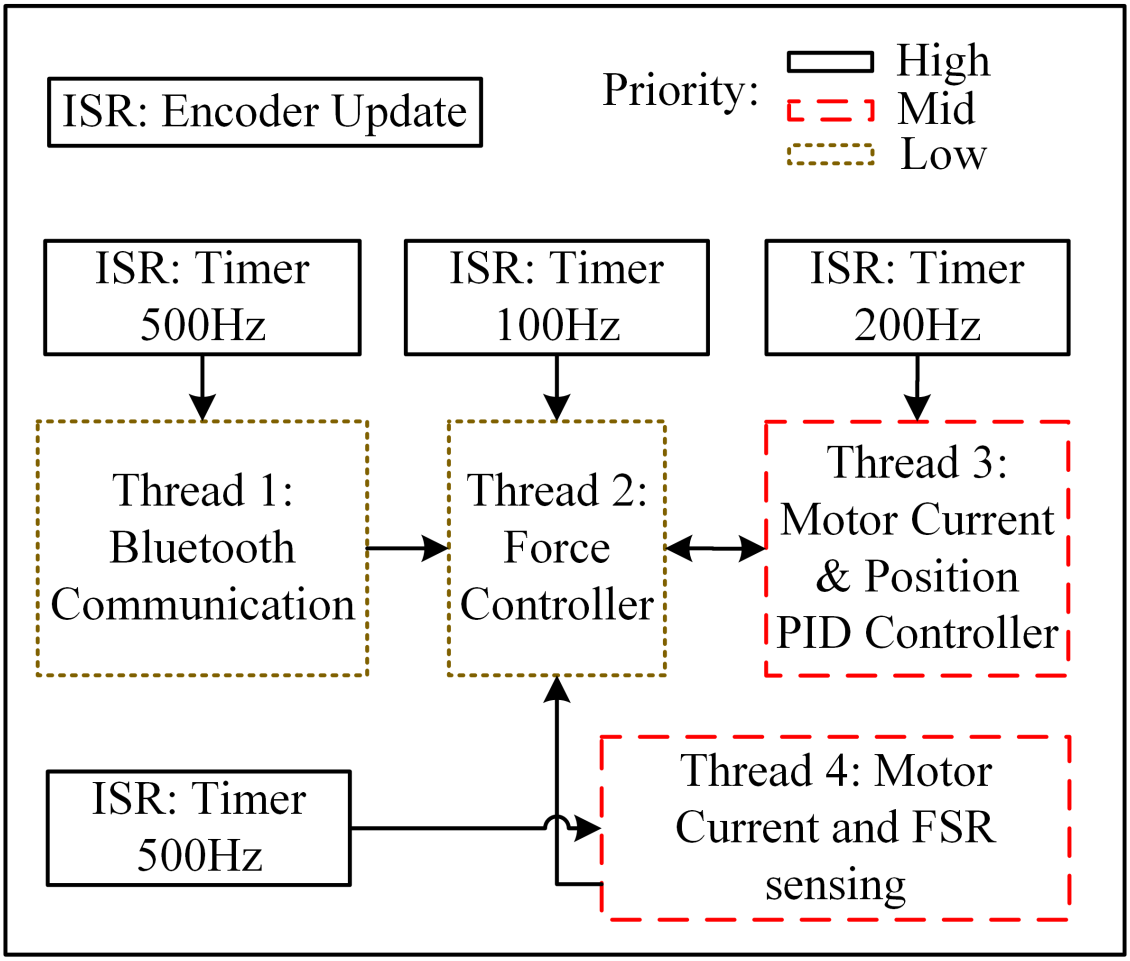

Figure 3.9: Exoskeleton glove low-level control block diagram.

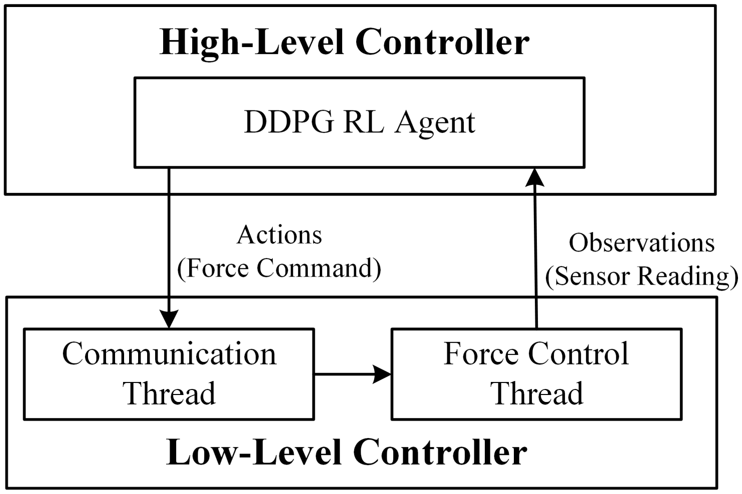

Figure 3.10: Exoskeleton glove control block diagram.

appropriate actions to the low-level controller.

3.6 Conclusion

This chapter presented a novel exoskeleton glove mechanism that has a low-profile, compact, and portable design feature for individuals with hand disabilities, to assist their activities of daily living and for rehabilitation. Mechanism and mechanical design were presented first. Kinematic analysis and kinematic synthesis of the novel mechanism for a better alignment with the actual human hand motion were then conducted. The optimized exoskeleton achieved a similar motion as a human finger for grasping objects. The glove and the actuators were integrated and mounted on the back of the hand to avoid external actuation. A proof-of-concept prototype was then built and the low level control is also introduced.

Comparing the novel low-profile exoskeleton glove with the previous exoskeleton glove integrated with SEA (mentioned in Chapter 2), several significant improvements are observed. The new exoskeleton glove is considerably lighter in weight, thanks to the compact design and utilization of the novel mechanism. This leads to a substantial enhancement in wearability, providing a more comfortable experience for the users.

The innovative mechanism design effectively addresses the problem of interference with the human hand. Specifically, the new finger mechanism minimizes the movements gap between the exoskeleton glove and the human hand during grasping, resulting in a much closer fit and improved overall functionality. Additionally, the unique thumb mechanism design plays a crucial role in reducing interference and ensuring seamless integration with the user's hand.

Overall, the novel low-profile exoskeleton glove demonstrates remarkable advancements in terms of weight, design, and wearability, effectively solving the previous challenges associated with the exoskeleton glove's fit and comfort during use. These improvements are crucial in enhancing the user's experience and promoting the widespread adoption of such devices for hand rehabilitation and assistance.

Chapter 4

Exoskeleton Glove Control by Using Deep Reinforcement Learning

4.1 Introduction

This chapter presents the exoskeleton glove control by using deep reinforcement learning. The current research on exoskeleton gloves primarily focuses on mechanism design, with limited attention given to the development of force control algorithms [93]. Many existing control policies are designed to demonstrate the feasibility of the mechanisms but lack the capability to adjust forces during grasping and adapt to different grasp types [35]. Recognizing these shortcomings, we propose an adaptive force control method based on reinforcement learning. This approach aims to enable real-time force adjustment during grasping based on different target objects. By employing this method, we seek to enhance the exoskeleton glove's ability to plan forces according to the specific requirements of different grasping tasks.

4.2 Simulation Environment Setup

Simulation plays a crucial role in verifying the functionality of both the hardware and control system, as well as accelerating the design process for complex control algorithms. The proposed exoskeleton glove simulation is conducted using Matlab Simscape R2022b. Comparing to other simulation softwares such as Mujoco, V-rep, and Gazebo, Simscape offers a more stable solution for simulating coupling mechanisms and parallel robots. It also provides an easy way to import complex 3D models, establish connections between the simulation environment and agent, and implement real-time control based on trained agents.

The simulation can be divided into three main parts: (1) selection of simulation parameters, (2) control of simulated actuators, and (3) analysis of simulation results.

4.2.1 Simulation Parameter Selection

To ensure the accuracy and reliability of our simulation, three distinct sets of parameters are established.

The first set of parameters in our simulation pertains to the representation of the physical attributes of the simulated objects. These attributes encompass the mass, center of mass, and moment of inertia. To uphold precision and uniformity, we systematically generate these attributes for the exoskeleton glove by appropriately assigning material properties within SolidWorks.

For the target objects, their dimensions and weights undergo controlled variations spanning ±15% of their original values (Table 4.1). This deliberate variation aims to simulate real-world scenarios where objects exhibit slight discrepancies in their properties, such as size and weight.

The second parameter set governs the internal mechanisms of the simulated actuators. The physical exoskeleton glove comprises seven actuators: one for each digit, another for the thumb carpometacarpal (CMC) joint, and one for the wrist (solely for mimicking wrist motion within the simulation environment). To emulate the abduction and adduction motions of human fingers, passive revolute joints are utilized between the finger mechanism and the exoskeleton glove base. In the simulation, these passive joints are endowed with high stiffness and constraints to optimize computational efficiency. This configuration obviates the need for calculating contact forces between distinct fingers. As a result, each finger incorporates two actuators: a prismatic joint for linear control and a revolute joint for simulating abduction and adduction. Furthermore, an extra actuator is dedicated to the rotary motion of the thumb's thenar. To model the behavior of a motor in physical hardware, a spring-damper system is adopted as the internal mechanism for these simulated actuators. The spring-damper system of the prismatic joint possesses a spring stiffness of 0N/m and a damping ratio of 1300N/(m/s). On the other hand, the spring stiffness of the thumb's rotary joint stands at 0 $(\mathrm{N} \cdot \mathrm{m})/\mathrm{deg}$, accompanied by a damping ratio of $0.001\mathrm{N} \cdot \mathrm{m}/(\mathrm{deg}/\mathrm{s})$. These specific values are determined through iterative experimentation to align with the behavior exhibited by the hardware.

The third parameter set encompasses the depiction of contact forces, specifically in the context of interactions between the fingers and the target objects, aiming to achieve a faithful representation within the simulation results. These parameters encompass stiffness, damping ratio, static friction, and dynamic friction. These values are informed by prior research [94].

4.2.2 Actuator Control in Simulation Environment

In the simulation environment, each free joint is equipped with an actuator for generating the necessary motion, using either force/torque or position control. Specifically, the revolute joints responsible for emulating the abduction and adduction motions are governed by an integrated position controller, enabling them to maintain specific positions corresponding to the given grasp type. Additionally, the motor and leadscrew combination for each digit is simulated as a single linear actuator, with these linear actuators being regulated through a built-in force controller to ensure meticulous force control. Lastly, the torque controller integrated within the system is employed to manage the thumb's rotary actuator, thereby facilitating precise torque control. These meticulously designed control strategies effectively dictate the behavior of the simulated actuators in the system.

4.3 Deep Reinforcement Learning for Force Control

Deep reinforcement learning (DRL) techniques are notably advantageous for mastering learning tasks in environments characterized by high-dimensional continuous observation and action spaces. In contrast to conventional reinforcement learning approaches, DRL capitalizes on deep neural networks to establish mappings between states and actions. This empowers DRL to effectively navigate intricate and continuous environments, obviating the necessity for a predetermined or acquired dynamics model [95].

4.3.1 Policy Selection

In the realm of model-free deep reinforcement learning (DRL) methods, two prominent strategies tailored for continuous action spaces are Proximal Policy Optimization (PPO) [96] and Deep Deterministic Policy Gradient (DDPG) [97]. PPO, operating within the on-policy paradigm, directly enhances policies through policy gradient techniques. It integrates a trust region framework to ensure the stability of policy updates, employing a clipped surrogate objective to forestall excessively large policy alterations. However, PPO's generation of actions based on mean and standard deviation makes it challenging to enforce physical constraints on the action space. This might necessitate additional training steps to ensure actions adhere to desired boundaries. Furthermore, the high cost of sampling from the simulation environment inflates training time.

Conversely, DDPG belongs to the off-policy category, constructing a deterministic policy and leveraging an off-policy experience replay buffer to heighten sample efficiency and stability. It employs an actor-critic architecture, with the actor network shaping the policy and the critic network shaping the value function. This methodology has proven effective in managing continuous control tasks.

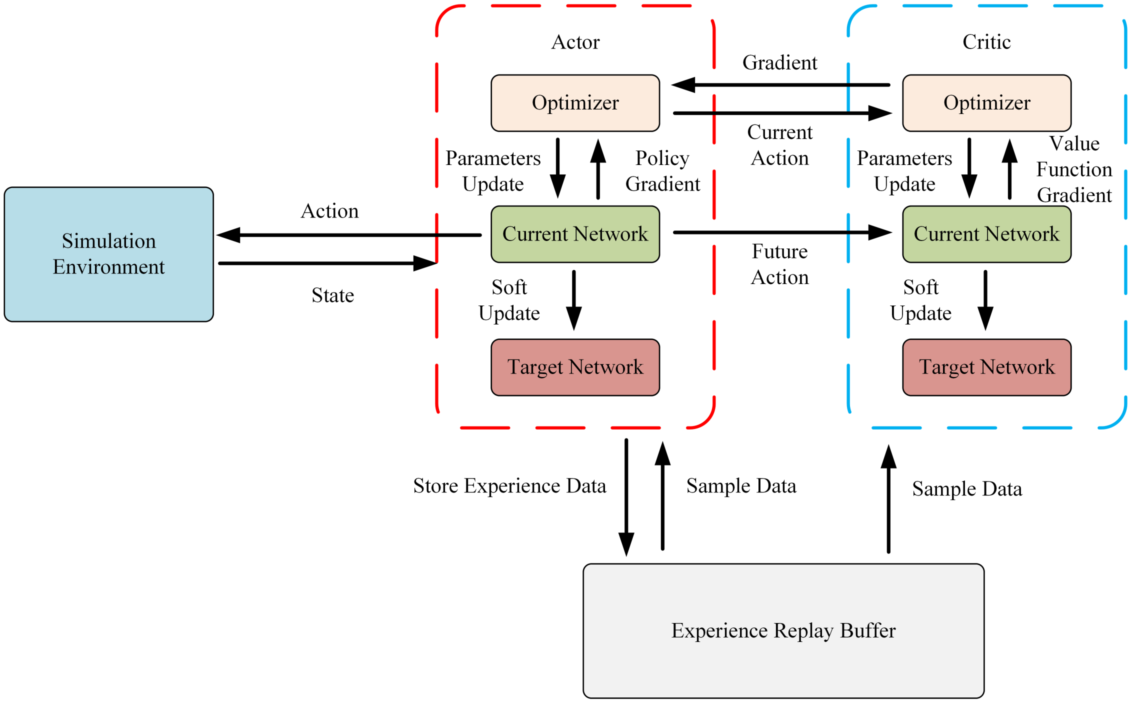

Figure 4.1: The general structure of DDPG algorithm.

Our approach employs the DDPG algorithm to implement the force controller for the proposed exoskeleton glove, serving as a proof of concept. Fig. 4.1 shows the general structure of DDPG algorithm. The DDPG agent encompasses both an Actor and a Critic neural network to embody policy and value functions, respectively. The actor network devises actions based on its prevailing policy and environment observations, while the critic evaluates these actions using observations and rewards. The simulation environment encompasses a simulated exoskeleton model, as previously outlined.

4.3.2 Reward Function

Designing a suitable reward function is one of the key challenges in training the DRL agent. The reward function must fulfill two simultaneous requirements. Firstly, the exoskeleton should exert minimal effort while successfully lifting objects of various sizes and shapes. Secondly, the exoskeleton's motion should closely adhere to the position limitations and natural movements of the human hand. During a cylinder grasp, it is important that all fingers extend until they make contact with the target object. Additionally, it is desirable for the extension of each finger to remain relatively consistent, without significant variation.

In light of these considerations, the reward function can be defined as follows:

$$r = c_1 R_s + c_2 R_h + c_3 R_f + c_4 R_{fd} + c_5 R_c \tag{4.1}$$

where

$$R_s = -|h_e - h_o| \tag{4.2}$$

$$R_h = \begin{cases} 3, & \text{if lift height} \geq 3\text{mm} \\ 0, & \text{otherwise} \end{cases} \tag{4.3}$$

$$R_f = -\sum_n f_n \tag{4.4}$$

$$R_{f_d} = -\sum_n |f_{d_n}| \tag{4.5}$$

$$R_c = \begin{cases} T_s/T_f, & \text{if contact is detected} \\ 0, & \text{otherwise} \end{cases} \tag{4.6}$$

and c_i denotes the weights for different partial rewards, subscript $i \in \{1, 2, 3, 4, 5\}$, h_e denotes the height of the exoskeleton glove, h_o denotes the height of the object, f_n denotes to the force generated by each finger actuator, $n \in \{thumb, index, middle, ring, little\}$, f_d represents the first-order derivative of the generated force, T_s denotes the sample time, and T_f denotes the final simulation time of the environment.

The term R_s is utilized to penalize the agent in the condition of slip occurrence, while R_h encourages the agent to successfully lift the target object. To promote minimal effort in lifting, the term R_f penalizes the force generated by each actuator. In order to enhance consistency in the generated force, R_{f_d} penalizes significant variations in force. Additionally, R_c is incorporated to motivate the agent to avoid premature termination.

4.3.3 Observation & Action Spaces

The observation space determines the available information about the environment for robot agent. At each time step, the robot agent receives the following observations:$\{p_n, q_n, v_n, c_i\}$, where p denotes the position of the linear actuator, q denotes the force generated from linear actuator, v denotes the speed of the linear actuator, $n \in \{thumb, index, middle, ring, little\}$, c denotes the contact force on the thumb and index fingertips, and $i \in \{thumb, index\}$. The selection of only two fingertips' contact forces is deliberate, driven by the limited repeatability of FSRs and the desire to minimize reliance on such observations. And these two fingertips contact forces are essential for the five target grasp types. These specific observations were selected based on the measurable characteristics of the exoskeleton glove in real-world scenarios. To ensure consistency and compatibility, all observations are normalized between 0 and 1 before being inputted to the DDPG agent for training and decision-making.

The action space of the exoskeleton glove is inherently uncomplicated, aligning with the number of actuators it encompasses. The deep neural network is trained to generate motor control instructions, with any requisite error correction or refinement being learned by the policy network itself. To guarantee that the output from the actor neural network remains within the intended spectrum, a sigmoid function is applied to the final layer. This sigmoid function effectively normalizes the output between 0 and 1. By subsequently scaling this bounded action with the corresponding force coefficient, the resultant output can be seamlessly converted to the desired force control span, ranging from 0N to 13N for the fingers and from $0N \cdot m$ to $0.35N \cdot m$ for the thumb in this specific instance.

It is important to note that in the real-world scenario, the lifting motion is typically controlled by human. However, in the simulation environment, a simplified approach is taken. When the thumb and index finger make contact with the object, a constant force of 25N is applied to simulate the lifting action. This approximation is used to mimic the lifting process observed in the real-world, but it is important to note that this lifting motion is not generated by the DDPG agent itself. Instead, it is triggered by the simulation environment to provide an interaction between the exoskeleton glove and the object being lifted.

4.3.4 Episode Termination Criteria in DRL Training

Episode termination criteria play a crucial role in halting ongoing training episodes when the agent deviates irrecoverably far from its intended objective, thereby saving valuable time. Throughout the training process, we integrate three distinct termination criteria to halt each episode's simulation. Firstly, if the object has slipped by more than 3 centimeters, indicating a loss of grip. Secondly, when the exoskeleton reaches an uncomfortable position, such as when the distance between each finger actuator exceeds 4mm, resulting in an unnatural finger separation gesture. Lastly, if the simulation time surpasses a predefined threshold, the episode is brought to an end.

4.4 Experimental Results

To showcase the exoskeleton glove's capabilities, a series of grasp experiments were conducted both in a simulation environment and using the physical exoskeleton glove. Nine target objects (listed in Table 4.1) were selected for performing five different types of grasp: Cylinder grasp, Sphere grasp, Tripod grasp, Lateral grasp, and Tip grasp. The experiments will be discussed from three perspectives: simulation results, bridging the gap between simulation environment with physical environment, and physical experiments with the exoskeleton glove hardware.

Table 4.1: Objects used in grasp experiments

Name	Weight (g)	Grasp Type
Glue Jar	200	Cylinder
Water Bottle	600	Cylinder
Orange	385	Sphere
Tennis Ball	69	Sphere
Pen	13	Tripod
Flat Box	102	Lateral
Paper Bowl	8	Lateral
Small Box	11	Tip
Heavy Box	211	Tip

4.4.1 Bridge the Gap Between Simulations and Physical Environment

To mitigate discrepancies between the simulation and physical environments, diligent efforts were undertaken to align the observations and actions of the reinforcement learning agent. The agent's observations include actuators' position, speed and force, and fingertip contact force. The position and speed of the linear actuators can be directly measured. The calibrated FSRs forces, as discussed in Section 3.5, corresponds to fingertip contact forces within the simulation environment. Moreover, the actuators forces, as calibrated using motor current consumption as outlined in Section 3.5, aligns with the actuators forces in the observations. The subsequent-time-step actuators' forces function as the control output within the simulation environment and are transformed into motors' currents through the calibration outcomes delineated in Section 3.5.

4.4.2 Results

To validate the effectiveness of the trained reinforcement learning agent in performing grasping tasks, a series of grasp experiments were conducted in the simulation environment.

As shown in Fig. 4.2, the reinforcement learning agent successfully grasped the target objects in the simulation environment. The agent demonstrated the ability to execute precise and coordinated finger movements, resulting in effective grasping of the objects. The agent's capability to adapt and learn from interactions with the environment allowed it to grasp objects of various shapes and sizes, demonstrating its versatility and robustness in handling different grasping scenarios.

The experimental outcomes also demonstrates the reinforcement learning agent's adept control of the exoskeleton within the physical environment. The finger gestures observed in the real-world closely mirror those acquired in the simulation, affirming the successful transference of learned behavior from the virtual domain to the tangible reality. This accomplishment underscores the agent's capacity to adapt and generalize its grasp strategy across varying environments and object configurations.

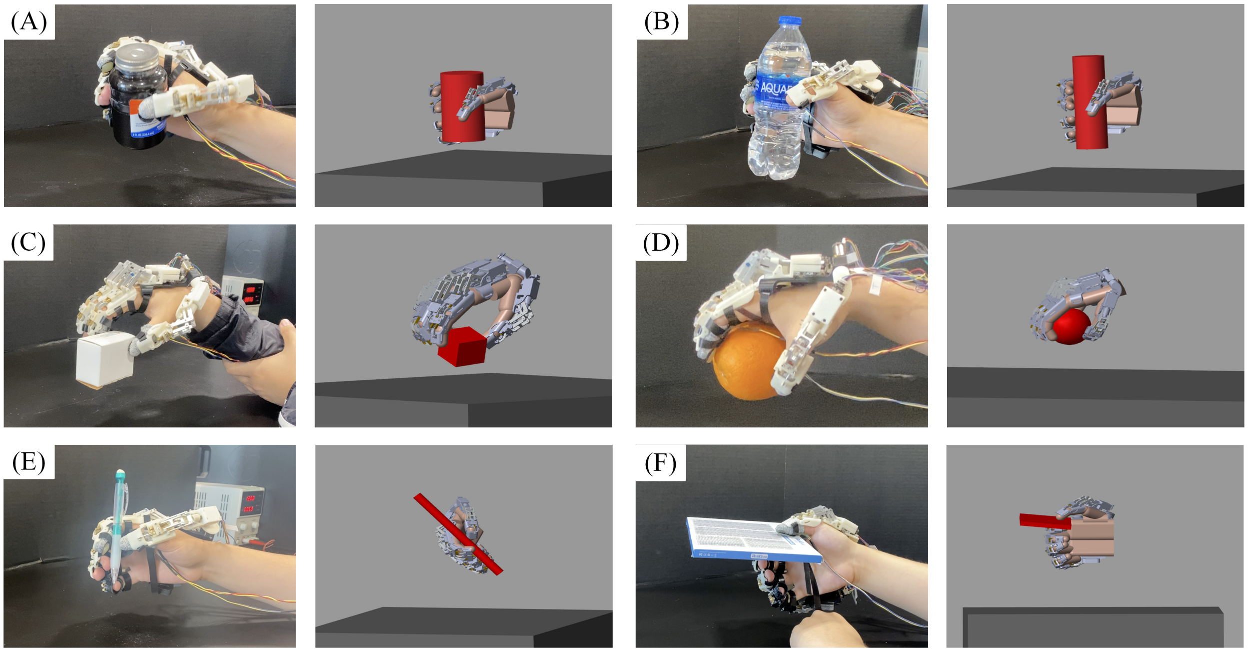

Figure 4.2: Successful grasps of various objects in both simulation environment and real-world. (A) jar, (B) bottle, (C) small box, (D) orange, (E) pen, (F) flat box.

4.4.3 Real-World Application

The reinforcement learning agent was effectively implemented and tested on the physical exoskeleton glove, with a healthy individual participating in the experiments. We opted for a human subject rather than a wooden hand in consideration of the latter's inability to perform passive abduction and adduction motions. Additionally, the exoskeleton glove's rigid linkage design prohibits subjects from applying force to the exoskeleton, reinforcing the appropriateness and justification of involving a healthy participant.

Through the presentation of successful grasp performances in the physical environment (Figure 4.2), the validity of the reinforcement learning agent and its proficient control of the exoskeleton glove is established. This substantiates its potential as a promising methodology for practical applications, particularly in assisting individuals with hand disabilities.

Additionally, Figure 4.3 provides a comparison between the measured force and the planned force generated by the reinforcement learning agent during the grasp experiments. It is important to note that the only the curve corresponding to the digits or CMC joint that is sensed with normal force are chosen to be displayed, ensuring clarity and simplicity. Meanwhile, the remaining actuators move to their respective end positions at full speed.

The results clearly demonstrate that the measured force closely tracks the planned force generated by the reinforcement learning agent, except when the control limit is reached. This close alignment between the planned and measured forces highlights the agent's exceptional ability to accurately control the exoskeleton's force output. The agent's precise and reliable grasp control during the experiments further emphasizes its potential for assisting individuals with hand disabilities in performing various daily living tasks.

4.5 Conclusion

The deep reinforcement learning approach was used to provide real-time, self-adjustable force control based on different objects. A simulation environment was built to train the control policies, allowing us to simulate various scenarios and train the agents effectively. Through several experiments, the ability of our exoskeleton glove to grasp daily objects with dexterity is demonstrated.

The successful grasp performances in the physical simulation environment validated the efficacy of the reinforcement learning agent and its ability to effectively control the exoskeleton glove. This made it a promising approach for real-world applications in assisting individuals with hand disabilities.

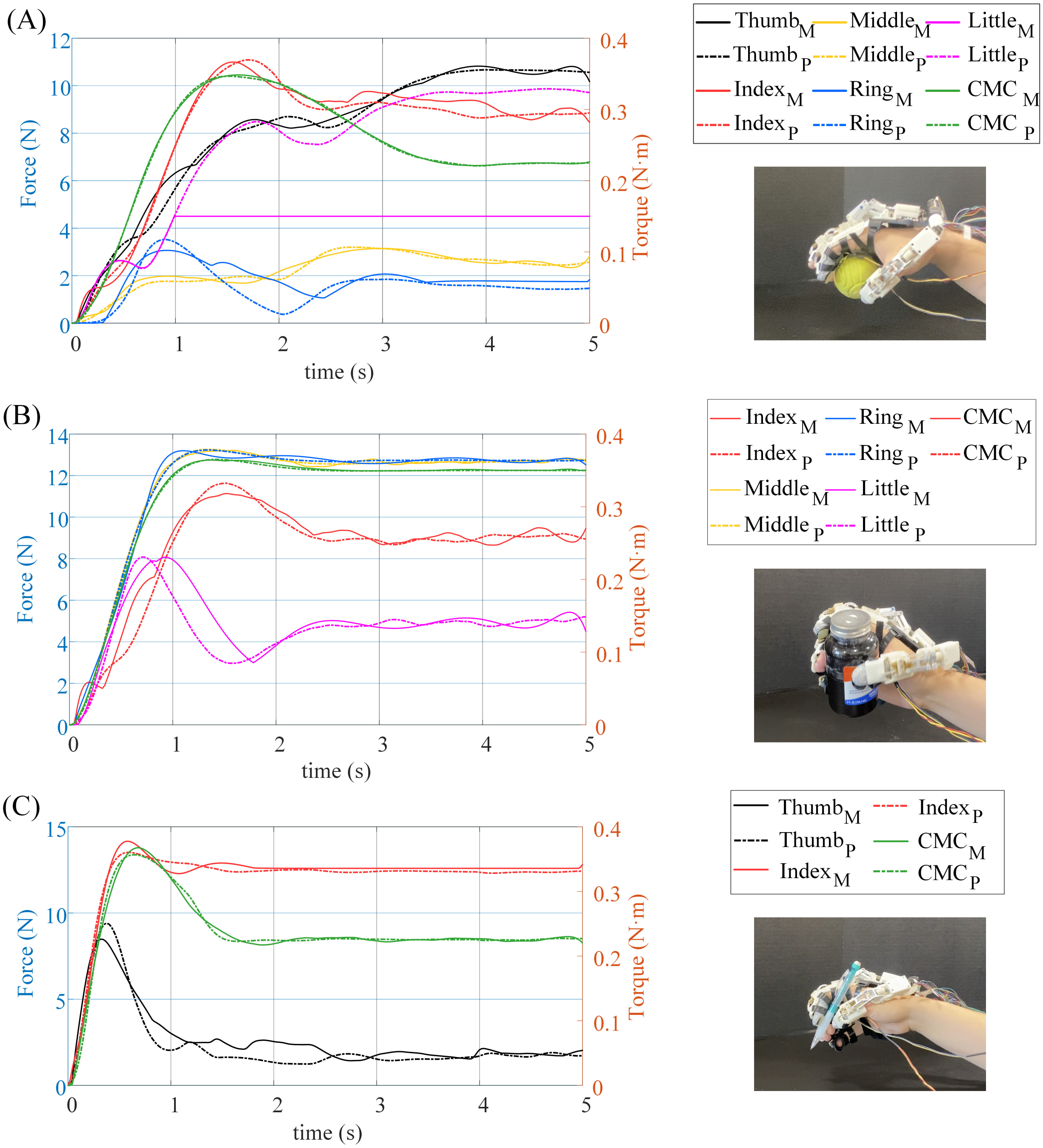

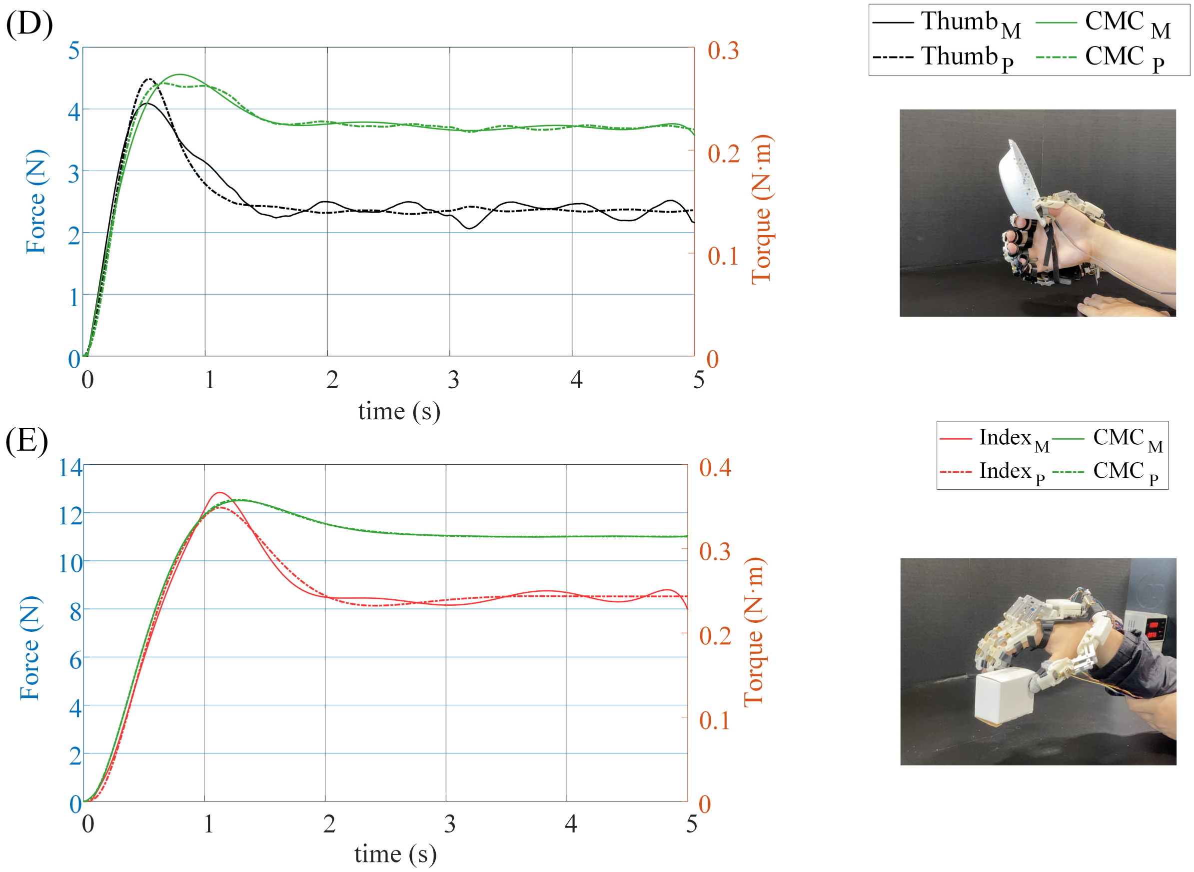

Figure 4.3: The comparison between planned actuator force and measured actuator force when perform five different types of grasp. The subscript P denotes the planned force/torque (shown as dash line) on the actuators based on the trained DDPG agent. The subscript M denotes the calculated force/torque (shown as solid line) on the actuators based on the calibration results. Five different grasp types are performed: (A) sphere grasp (little finger hit control limit), (B) cylinder grasp, (C) tripod grasp, (D) lateral grasp, (E) tip grasp.

The successful tracking of the planned force by the exoskeleton glove confirmed the effectiveness of the reinforcement learning agent's training process. This finding indicated that the agent had learned appropriate force control strategies, allowing it to perform grasping tasks in a controlled and stable manner.

Despite the success achieved in the physical grasp experiments, there are several challenges that need to be addressed to further enhance the performance and practicality of the exoskeleton glove. One of the primary challenges is accurately modeling the non-backdrivable actuators in the simulation environment. The predefined mass-spring-damper model in MATLAB lacks the properties of actual linear actuators, leading to discrepancies between the simulated and real-world behaviors. This disparity may result in variations in force output and finger movements, affecting the overall grasp performance.

Additionally, the reinforcement learning agent may not consistently provide a constant force during stable grasps. This variability is attributed to the noise intentionally added to the agent's actions during training to promote exploration. While the noise is essential for learning and adapting to different scenarios, it can lead to less consistent force control during practical applications, especially for tasks requiring precise and steady force application.

Furthermore, the long-term use of the exoskeleton glove may lead to data-based calibration drift, necessitating periodic re-calibration to bridge the gap between the simulation environment and real-world conditions. This drift can impact the accuracy and reliability of the glove's force control and finger movements, potentially affecting the wearer's grasp performance over time.

Overall, the successful deployment of the reinforcement learning agent onto the physical exoskeleton glove, along with the close resemblance between the simulated and physical finger gestures, underscores the potential of our approach for real-world applications in hand rehabilitation and assistance. The close tracking of planned and measured forces further validates the efficacy of the reinforcement learning-based control strategy in achieving accurate force control in the exoskeleton glove.

Chapter 5

Conclusion and Future Work

This chapter summarizes the dissertation by recapping the major work of this research and providing directions for future research.

5.1 Summary

This dissertation made significant contributions in three key areas. Firstly, it provided a comprehensive investigation into the modeling, analysis, and control aspects of exoskeleton gloves, covering both traditional exoskeleton gloves with SEA and the novel low-profile exoskeleton glove. This thorough exploration addressed critical design challenges faced by existing exoskeleton glove devices.

Secondly, this research introduced two innovative robotic exoskeleton glove mechanisms, specifically designed to overcome various design challenges. These novel mechanisms represented a significant advancement in the field of exoskeleton glove development, offering improved wearability, comfortability, and portability.

Thirdly, a deep reinforcement learning-based method was proposed for real-time self-adjustable force control based on different objects. By utilizing intelligent force control, the exoskeleton glove could adapt its grasping force in response to different objects, enhancing its performance and versatility during manipulation tasks.

Overall, this dissertation contributed to the fields of modeling, analysis, intelligent force control, and hardware development for exoskeleton gloves intended for patients with hand disabilities. The findings of this research laid the foundation for future studies aimed at creating human-like robotic exoskeleton gloves, not only in terms of morphology but also in their ability to mimic natural hand motions effectively. The impact of this work extended to the advancement of wearable robotics and rehabilitation technologies, ultimately improving the quality of life for individuals with hand disabilities.

5.2 Future Research Directions

Although the research presented in this work provides significant progress in the area of exoskeleton glove, much work remains to be done in an effort to match or even exceed the performance of the developed exoskeleton glove in comparison to healthy human hand in terms of motion agility, dexterity, and versatility. This section discusses the potential future directions of this research.

5.2.1 Compact and portable exoskeleton glove with multiple degrees of freedom

Indeed, the number of actuated DOFs is a critical consideration in hand exoskeleton design, especially when aiming to achieve a balance between task complexity and portability. Low DOFs are often preferred based on the premise that many activities of daily living (ADLs) do not necessarily require fine and independent control or a high number of DOFs in the hand. However, certain delicate grasping tasks, such as index finger extension, ventral grasp, and precision grasp, may necessitate additional DOFs to achieve specific hand postures. The manipulation of the thumb is also of utmost importance in hand exoskeleton studies and in the literature on robotic hands and prosthetics due to its fundamental role in grasping. Nonetheless, increasing the number of DOFs introduces the need for more actuators, which subsequently increases the size and weight of the exoskeleton device, ultimately affecting its compactness and portability for everyday activities.

Therefore, a crucial research direction involves striking a balance between the DOFs of the exoskeleton glove and its overall portability to ensure it can perform as many grasp tasks as possible while maintaining portability and usability in real-world scenarios. Achieving this balance will facilitate the development of exoskeleton gloves that enhance hand functionality for individuals with hand disabilities, enabling them to engage in a broader range of activities and improving their overall quality of life.

5.2.2 Elaborate sensor design and dexterous force/torque control algorithms

The direct sensing of each joint angle or grasping force can significantly enhance precise control in exoskeleton gloves. However, achieving this level of sensing precision requires elaborate sensor design, fabrication, and assembly processes, all of which contribute to an increase in overall system complexity. As a result, there exists a trade-off relationship between control capability and system simplicity.

Current exoskeleton gloves utilize feed-forward control methods to actuate the system. Actuators are employed to provide actuation using pre-calibrated trajectories corresponding to specific grasping postures. While this control scheme offers a simple and concise system design, it may not consistently provide optimal control performance due to the complex and uncertain hand kinematics of the user.

Therefore, a promising future research direction involves the development of non-invasive, bio-compatible, and small sensors, specifically designed for exoskeleton gloves. These sensors should be integrated into intelligent force control algorithms, which aims to uniformly provide elaborate force/torque control for various grasp types, different target objects, and diverse users' hand shapes and sizes. By achieving such advancements, exoskeleton gloves can offer more seamless and natural control, effectively enhancing the user's grasping experience and overall functionality.

5.2.3 Exoskeleton glove evaluation methods establishment

Quantifying the performance of exoskeleton gloves during usage by human subjects is crucial to assess their operational efficacy and mechanical capabilities. However, the type and methodology of testing widely vary among published literature in the field of hand exoskeletons. This diversity can be attributed to the numerous testing mechanisms available for analyzing hand motion function. The wide range of evaluation methods used in hand exoskeleton literature makes it challenging to discuss and compare different tests without proper categorization.

Therefore, an important and promising research direction is to establish standardized evaluation methods specifically tailored for medical exoskeleton gloves. Developing a set of standardized tests will allow for more consistent and reliable performance comparisons across different exoskeleton devices. These evaluation methods should take into account various aspects of hand function, such as grasping capabilities, dexterity, precision, force sensitivity, and user comfort.

Bibliography

[1] M. W. Brault *et al.*, *Americans with disabilities: 2010.* US Department of Commerce, Economics and Statistics Administration, US ..., 2012.

[2] R. Midha, “Epidemiology of Brachial Plexus Injuries in a Multitrauma Population,” *Neurosurgery*, no. June, pp. 1182–1189, 1997.

[3] H. R. Park, G. S. Lee, I. S. Kim, and J.-C. Chang, “Brachial Plexus Injury in Adults,” *The Nerve*, vol. 3, no. 1, pp. 1–11, 2017.

[4] M. Sumida, M. Fujimoto, A. Tokuhiro, T. Tominaga, A. Magara, and R. Uchida, “Early rehabilitation effect for traumatic spinal cord injury,” *Archives of physical medicine and rehabilitation*, vol. 82, no. 3, pp. 391–395, 2001.

[5] G. Scivoletto, B. Morganti, and M. Molinari, “Early versus delayed inpatient spinal cord injury rehabilitation: an italian study,” *Archives of physical medicine and rehabilitation*, vol. 86, no. 3, pp. 512–516, 2005.

[6] J. L. Giuffre, S. Kakar, A. T. Bishop, R. J. Spinner, and A. Y. Shin, “Current Concepts of the Treatment of Adult Brachial Plexus Injuries,” *Journal of Hand Surgery*, vol. 35, pp. 678–688, 4 2010.

[7] R. A. Bos, C. J. Haarman, T. Stortelder, K. Nizamis, J. L. Herder, A. H. Stienen, and D. H. Plettenburg, “A structured overview of trends and technologies used in dynamic hand orthoses,” *Journal of NeuroEngineering and Rehabilitation*, vol. 13, no. 1, pp. 1–25, 2016.

[8] A. Borboni, M. Mor, and R. Faglia, “Gloreha-Hand Robotic Rehabilitation: Design, Mechanical Model, and Experiments,” *Journal of Dynamic Systems, Measurement and Control, Transactions of the ASME*, vol. 138, 11 2016.

[9] F. Orihuela-Espina, G. F. Roldán, I. Sánchez-Villavicencio, L. Palafox, R. Leder, L. E. Sucar, and J. Hernández-Franco, “Robot training for hand motor recovery in subacute stroke patients: A randomized controlled trial,” *Journal of Hand Therapy*, vol. 29, pp. 51–57, 1 2016.

[10] P. Polygerinos, Z. Wang, K. C. Galloway, R. J. Wood, and C. J. Walsh, “Soft robotic glove for combined assistance and at-home rehabilitation,” *Robotics and Autonomous Systems*, vol. 73, pp. 135–143, 2015.

[11] Y. Chen, Z. Yang, and Y. Wen, “A soft exoskeleton glove for hand bilateral training via surface emg,” *Sensors*, vol. 21, no. 2, p. 578, 2021.

[12] R. Deimel and O. Brock, “A novel type of compliant and underactuated robotic hand for dexterous grasping,” *The International Journal of Robotics Research*, vol. 35, pp. 161–185, 1 2016.

[13] F. Ilievski, A. D. Mazzeo, R. F. Shepherd, X. Chen, and G. M. Whitesides, “Soft Robotics for Chemists,” *Angewandte Chemie*, vol. 123, pp. 1930–1935, 2 2011.

[14] M. Haghshenas-Jaryani, R. M. Patterson, N. Bugnariu, and M. B. Wijesundara, “A pilot study on the design and validation of a hybrid exoskeleton robotic device for hand rehabilitation,” *Journal of Hand Therapy*, vol. 33, no. 2, pp. 198–208, 2020.

[15] Y. M. Zhou, D. Wagner, K. Nuckols, R. Heimgartner, C. Correia, M. Clarke, D. Orzel, C. O’Neill, R. Solinsky, S. Paganoni, *et al.*, “Soft robotic glove with integrated sensing for

intuitive grasping assistance post spinal cord injury," in *2019 International conference on robotics and automation (ICRA)*, pp. 9059–9065, IEEE, 2019.

[16] H. K. Yap, J. H. Lim, F. Nasrallah, and C.-H. Yeow, "Design and preliminary feasibility study of a soft robotic glove for hand function assistance in stroke survivors," *Frontiers in neuroscience*, vol. 11, p. 547, 2017.

[17] A. Stilli, A. Cremoni, M. Bianchi, A. Ridolfi, F. Gerii, F. Vannetti, H. A. Wurdemann, B. Allotta, and K. Althoefer, "Airexglove—a novel pneumatic exoskeleton glove for adaptive hand rehabilitation in post-stroke patients," in *2018 IEEE international conference on soft robotics (RoboSoft)*, pp. 579–584, IEEE, 2018.

[18] H. Al-Fahaam, S. Davis, S. Nefti-Meziani, and T. Theodoridis, "Novel soft bending actuator-based power augmentation hand exoskeleton controlled by human intention," *Intelligent Service Robotics*, vol. 11, pp. 247–268, 2018.

[19] H. K. Yap, B. W. Ang, J. H. Lim, J. C. Goh, and C. H. Yeow, "A fabric-regulated soft robotic glove with user intent detection using EMG and RFID for hand assistive application," in *Proceedings - IEEE International Conference on Robotics and Automation*, vol. 2016-June, pp. 3537–3542, Institute of Electrical and Electronics Engineers Inc., 6 2016.

[20] Z. Ma, P. Ben-Tzvi, and J. Danoff, "Sensing and Force-Feedback Exoskeleton Robotic (SAFER) Glove Mechanism for Hand Rehabilitation," *Proceedings of the ASME Design Engineering Technical Conference*, vol. 5A-2015, pp. 1–8, 2015.

[21] M. Aiple and A. Schiele, "Pushing the limits of the CyberGrasp™ for haptic rendering," *Proceedings - IEEE International Conference on Robotics and Automation*, pp. 3541–3546, 2013.

[22] U. A. Hofmann, T. Bützer, O. Lambercy, and R. Gassert, "Design and Evaluation of a Bowden-Cable-Based Remote Actuation System for Wearable Robotics," *IEEE Robotics and Automation Letters*, vol. 3, no. 3, pp. 2101–2108, 2018.

[23] B. B. Kang, H. Choi, H. Lee, and K.-J. Cho, "Exo-glove poly ii: A polymer-based soft wearable robot for the hand with a tendon-driven actuation system," *Soft robotics*, vol. 6, no. 2, pp. 214–227, 2019.

[24] P. Tran, S. Jeong, S. L. Wolf, and J. P. Desai, "Patient-specific, voice-controlled, robotic flexotendon glove-ii system for spinal cord injury," *IEEE Robotics and Automation Letters*, vol. 5, no. 2, pp. 898–905, 2020.

[25] S. Jeong, P. Tran, and J. P. Desai, "Integration of self-sealing suction cups on the flexotendon glove-ii robotic exoskeleton system," *IEEE Robotics and Automation Letters*, vol. 5, no. 2, pp. 867–874, 2020.

[26] Y.-J. Kim, Y.-J. Jeong, H.-S. Jeon, D.-W. Lee, and J.-I. Kim, "Development of a soft robotic glove with high gripping force using force distributing compliant structures," in *2017 IEEE/RSJ International Conference on Intelligent Robots and Systems (IROS)*, pp. 3883–3890, IEEE, 2017.

[27] D. H. Kim and H.-S. Park, "Cable actuated dexterous (cadex) glove for effective rehabilitation of the hand for patients with neurological diseases," in *2018 IEEE/RSJ International Conference on Intelligent Robots and Systems (IROS)*, pp. 2305–2310, IEEE, 2018.

[28] M. K. Burns, D. Pei, and R. Vinjamuri, "Myoelectric control of a soft hand exoskeleton using kinematic synergies," *IEEE transactions on biomedical circuits and systems*, vol. 13, no. 6, pp. 1351–1361, 2019.

[29] D. Leonardis, M. Barsotti, C. Loconsole, M. Solazzi, M. Troncossi, C. Mazzotti, V. P. Castelli, C. Procopio, G. Lamola, C. Chisari, M. Bergamasco, and A. Frisoli, "An EMG-controlled robotic hand exoskeleton for bilateral rehabilitation," *IEEE Transactions on Haptics*, vol. 8, no. 2, pp. 140–151, 2015.

[30] N. S. Ho, K. Y. Tong, X. L. Hu, K. L. Fung, X. J. Wei, W. Rong, and E. A. Susanto, "An EMG-driven exoskeleton hand robotic training device on chronic stroke subjects: Task training system for stroke rehabilitation," in *IEEE International Conference on Rehabilitation Robotics*, 2011.

[31] I. Sarakoglou, A. Brygo, D. Mazzanti, N. G. Hernandez, D. G. Caldwell, and N. G. Tsagarakis, "Hexotrac: A highly under-actuated hand exoskeleton for finger tracking and force feedback," in *2016 IEEE/RSJ International Conference on Intelligent Robots and Systems (IROS)*, pp. 1033–1040, IEEE, 2016.

[32] M. Malvezzi, T. L. Baldi, A. Villani, F. Ciccarese, and D. Prattichizzo, "Design, development, and preliminary evaluation of a highly wearable exoskeleton," in *2020 29th IEEE International Conference on Robot and Human Interactive Communication (RO-MAN)*, pp. 1055–1062, IEEE, 2020.

[33] A. Chiri, N. Vitiello, F. Giovacchini, S. Roccella, F. Vecchi, and M. C. Carrozza, "Mechatronic design and characterization of the index finger module of a hand exoskeleton for post-stroke rehabilitation," *IEEE/ASmE Transactions on mechatronics*, vol. 17, no. 5, pp. 884–894, 2011.

[34] M. B. Hong, S. J. Kim, Y. S. Ihn, G.-C. Jeong, and K. Kim, "Kulex-hand: An underactuated wearable hand for grasping power assistance," *IEEE Transactions on Robotics*, vol. 35, no. 2, pp. 420–432, 2018.

[35] P. Tran, S. Jeong, K. R. Herrin, and J. P. Desai, “Hand exoskeleton systems, clinical rehabilitation practices, and future prospects,” *IEEE Transactions on Medical Robotics and Bionics*, vol. 3, no. 3, pp. 606–622, 2021.

[36] D. Popov, I. Gaponov, and J.-H. Ryu, “Portable exoskeleton glove with soft structure for hand assistance in activities of daily living,” *IEEE/ASME Transactions on Mechatronics*, vol. 22, no. 2, pp. 865–875, 2016.

[37] H. Zhao, J. Jalving, R. Huang, R. Knepper, A. Ruina, and R. Shepherd, “A helping hand: Soft orthosis with integrated optical strain sensors and emg control,” *IEEE Robotics & Automation Magazine*, vol. 23, no. 3, pp. 55–64, 2016.

[38] C. Correia, K. Nuckols, D. Wagner, Y. M. Zhou, M. Clarke, D. Orzel, R. Solinsky, S. Paganoni, and C. J. Walsh, “Improving grasp function after spinal cord injury with a soft robotic glove,” *IEEE Transactions on Neural Systems and Rehabilitation Engineering*, vol. 28, no. 6, pp. 1407–1415, 2020.

[39] S. W. O Driscoll and N. J. Giori, “Continuous passive motion (cpm): theory and principles of clinical application,” *Journal of rehabilitation research and development*, vol. 37, no. 2, pp. 179–188, 2000.

[40] M. Mulas, M. Folgheraiter, and G. Gini, “An emg-controlled exoskeleton for hand rehabilitation,” in *9th International Conference on Rehabilitation Robotics, 2005. ICORR 2005.*, pp. 371–374, IEEE, 2005.

[41] L. Lucas, M. DiCicco, and Y. Matsuoka, “An emg-controlled hand exoskeleton for natural pinching,” *Journal of Robotics and Mechatronics*, vol. 16, pp. 482–488, 2004.

[42] M. Gabardi, M. Solazzi, D. Leonardis, and A. Frisoli, “Design and evaluation of a novel

5 dof underactuated thumb-exoskeleton," *IEEE Robotics and Automation Letters*, vol. 3, no. 3, pp. 2322–2329, 2018.

[43] C. N. Schabowsky, S. B. Godfrey, R. J. Holley, and P. S. Lum, "Development and pilot testing of hexorr: hand exoskeleton rehabilitation robot," *Journal of neuroengineering and rehabilitation*, vol. 7, pp. 1–16, 2010.

[44] A. Borboni, M. Mor, and R. Faglia, "Gloreha—hand robotic rehabilitation: design, mechanical model, and experiments," *Journal of Dynamic Systems, Measurement, and Control*, vol. 138, no. 11, p. 111003, 2016.

[45] P. Agarwal, J. Fox, Y. Yun, M. K. O'Malley, and A. D. Deshpande, "An index finger exoskeleton with series elastic actuation for rehabilitation: Design, control and performance characterization," *The International Journal of Robotics Research*, vol. 34, no. 14, pp. 1747–1772, 2015.

[46] Y. Yun, S. Dancausse, P. Esmatloo, A. Serrato, C. A. Merring, P. Agarwal, and A. D. Deshpande, "Maestro: An emg-driven assistive hand exoskeleton for spinal cord injury patients," in *2017 IEEE international conference on robotics and automation (ICRA)*, pp. 2904–2910, IEEE, 2017.

[47] J. Iqbal, N. Tsagarakis, A. E. Fiorilla, and D. Caldwell, "Design requirements of a hand exoskeleton robotic device," in *14th IASTED International Conference on Robotics and Applications (RA), Massachusetts US*, vol. 664, pp. 44–51, 2009.

[48] A. A. Blank, J. A. French, A. U. Pehlivan, and M. K. O'Malley, "Current trends in robot-assisted upper-limb stroke rehabilitation: promoting patient engagement in therapy," *Current physical medicine and rehabilitation reports*, vol. 2, no. 3, pp. 184–195, 2014.

[49] R. Colombo, F. Pisano, S. Micera, A. Mazzone, C. Delconte, M. C. Carrozza, P. Dario,

and G. Minuco, “Robotic techniques for upper limb evaluation and rehabilitation of stroke patients,” *IEEE transactions on neural systems and rehabilitation engineering*, vol. 13, no. 3, pp. 311–324, 2005.

[50] A. U. Pehlivan, F. Sergi, and M. K. O’Malley, “A subject-adaptive controller for wrist robotic rehabilitation,” *IEEE/ASME Transactions on Mechatronics*, vol. 20, no. 3, pp. 1338–1350, 2014.

[51] W. S. Harwin, T. Rahman, and R. A. Foulds, “A review of design issues in rehabilitation robotics with reference to north american research,” *IEEE Transactions on Rehabilitation Engineering*, vol. 3, no. 1, pp. 3–13, 1995.

[52] E. M. Refour, B. Sebastian, R. J. Chauhan, and P. Ben-Tzvi, “A General Purpose Robotic Hand Exoskeleton With Series Elastic Actuation,” *Journal of Mechanisms and Robotics*, vol. 11, 12 2019.

[53] T. Vanteddu, B. Sebastian, and P. Ben-Tzvi, “Design optimization of RML glove for improved grasp performance,” in *ASME 2018 Dynamic Systems and Control Conference, DSCC 2018*, vol. 1, American Society of Mechanical Engineers (ASME), 2018.

[54] J. Lee and P. Ben-Tzvi, “Design of a wearable 3-DOF forearm exoskeleton for rehabilitation and assistive purposes,” in *ASME International Mechanical Engineering Congress and Exposition, Proceedings (IMECE)*, vol. 3, pp. 1–10, 2017.

[55] Y. Guo, W. Xu, S. Pradhan, C. Bravo, and P. Ben-Tzvi, “Integrated and configurable voice activation and speaker verification system for a robotic exoskeleton glove,” in *International Design Engineering Technical Conferences and Computers and Information in Engineering Conference*, vol. 83990, American Society of Mechanical Engineers, 2020.

[56] Y. Guo, W. Xu, S. Pradhan, C. Bravo, and P. Ben-Tzvi, “Personalized voice activated grasping system for a robotic exoskeleton glove,” *Mechatronics*, vol. 83, p. 102745, 2022.

[57] E. Refour, B. Sebastian, and P. Ben-Tzvi, “Design and integration of a two-digit exoskeleton glove,” in *Proceedings of the ASME Design Engineering Technical Conference*, vol. 5A-2017, pp. 1–8, 2017.

[58] A. J. Kurdila and P. Ben-Tzvi, *Dynamics and Control of Robotic Systems.* John Wiley & Sons, Incorporated, 2019.

[59] W. Xu, Y. Guo, C. Bravo, and P. Ben-Tzvi, “Design, control, and experimental evaluation of a novel robotic glove system for patients with brachial plexus injuries,” *IEEE Transactions on Robotics*, vol. 39, no. 2, pp. 1637–1652, 2022.

[60] J. F. Soechting and M. Flanders, “Flexibility and repeatability of finger movements during typing: analysis of multiple degrees of freedom,” *Journal of computational neuroscience*, vol. 4, no. 1, pp. 29–46, 1997.

[61] G. A. Bekey, R. Tomovic, and I. Zeljkovic, “Control architecture for the belgrade/usc hand,” in *Dextrous robot hands*, pp. 136–149, Springer, 1990.

[62] Z. Ma, P. Ben-Tzvi, and J. Danoff, “Hand Rehabilitation Learning System with an Exoskeleton Robotic Glove,” *IEEE Transactions on Neural Systems and Rehabilitation Engineering*, vol. 24, no. 12, pp. 1323–1332, 2016.

[63] E. Refour, B. Sebastian, and P. Ben-Tzvi, “Two-digit robotic exoskeleton glove mechanism: Design and integration,” *Journal of Mechanisms and Robotics*, vol. 10, 4 2018.

[64] M. Valenzuela and B. Bordoni, *Anatomy, Shoulder and Upper Limb, Hand Dorsal Interossei Muscle.* StatPearls Publishing, 1 2020.

[65] B. J. Lee, A. Williams, and P. Ben-Tzvi, "Intelligent Object Grasping with Sensor Fusion for Rehabilitation and Assistive Applications," *IEEE Transactions on Neural Systems and Rehabilitation Engineering*, vol. 26, no. 8, pp. 1556–1565, 2018.

[66] B. Alexander and K. Viktor, "Proportions of hand segments," *International Journal of Morphology*, vol. 28, no. 3, pp. 755–758, 2010.

[67] M. Liu, "Hust dataset (march 2016)," Mar 2016.

[68] G. Pratt and M. Williamson, "Series elastic actuators," in *Proceedings 1995 IEEE/RSJ International Conference on Intelligent Robots and Systems. Human Robot Interaction and Cooperative Robots*, vol. 1, pp. 399–406 vol.1, 1995.

[69] W. Xu, S. Pradhan, Y. Guo, C. Bravo, and P. Ben-Tzvi, "A novel design of a robotic glove system for patients with brachial plexus injuries," in *International Design Engineering Technical Conferences and Computers and Information in Engineering Conference*, vol. 83990, American Society of Mechanical Engineers, 2020.

[70] Y. Yun, P. Agarwal, J. Fox, K. E. Madden, and A. D. Deshpande, "Accurate torque control of finger joints with ut hand exoskeleton through bowden cable sea," in *2016 IEEE/RSJ International Conference on Intelligent Robots and Systems (IROS)*, pp. 390–397, IEEE, 2016.

[71] V. Agrawal, *Modeling and control of cable actuated surgical robotic systems.* PhD thesis, Purdue University, 2011.

[72] T. Do, T. Tjahjowidodo, M. Lau, T. Yamamoto, and S. Phee, "Hysteresis modeling and position control of tendon-sheath mechanism in flexible endoscopic systems," *Mechatronics*, vol. 24, no. 1, pp. 12–22, 2014.

[73] C. W. Rowley, I. Mezić, S. Bagheri, P. Schlatter, and D. S. Henningson, “Spectral analysis of nonlinear flows,” *Journal of fluid mechanics*, vol. 641, pp. 115–127, 2009.

[74] P. J. Schmid, “Dynamic mode decomposition of numerical and experimental data,” *Journal of fluid mechanics*, vol. 656, pp. 5–28, 2010.

[75] H. Schaeffer, R. Caflisch, C. D. Hauck, and S. Osher, “Sparse dynamics for partial differential equations,” *Proceedings of the National Academy of Sciences*, vol. 110, no. 17, pp. 6634–6639, 2013.

[76] V. Ozoliņš, R. Lai, R. Caflisch, and S. Osher, “Compressed modes for variational problems in mathematics and physics,” *Proceedings of the National Academy of Sciences*, vol. 110, no. 46, pp. 18368–18373, 2013.

[77] S. L. Brunton, J. L. Proctor, and J. N. Kutz, “Discovering governing equations from data by sparse identification of nonlinear dynamical systems,” *Proceedings of the national academy of sciences*, vol. 113, no. 15, pp. 3932–3937, 2016.

[78] E. Kaiser, J. N. Kutz, and S. L. Brunton, “Sparse identification of nonlinear dynamics for model predictive control in the low-data limit,” *Proceedings of the Royal Society A*, vol. 474, no. 2219, 2018.

[79] J. B. Lee, “Development of Intelligent Exoskeleton Grasping Through Sensor Fusion and Slip Detection Development of Intelligent Exoskeleton Grasping,” Master’s thesis, Virginia Polytechnic Institute and State University, 2018.

[80] T. Feix, J. Romero, H. B. Schmiedmayer, A. M. Dollar, and D. Kragic, “The GRASP Taxonomy of Human Grasp Types,” *IEEE Transactions on Human-Machine Systems*, vol. 46, no. 1, pp. 66–77, 2016.

[81] D. Ryu, K.-W. Moon, H. Nam, Y. Lee, C. Chun, S. Kang, and J.-B. Song, "Micro hydraulic system using slim artificial muscles for a wearable haptic glove," in *2008 IEEE/RSJ International Conference on Intelligent Robots and Systems*, pp. 3028–3033, IEEE, 2008.

[82] C. J. Nycz, T. Bützer, O. Lambercy, J. Arata, G. S. Fischer, and R. Gassert, "Design and characterization of a lightweight and fully portable remote actuation system for use with a hand exoskeleton," *IEEE Robotics and Automation Letters*, vol. 1, no. 2, pp. 976–983, 2016.

[83] "Gloreha glove.." `https://www.gloreha.com/`. Accessed: 2022-02-02.

[84] X. Hu, K. Tong, X. Wei, W. Rong, E. Susanto, and S. Ho, "The effects of post-stroke upper-limb training with an electromyography (emg)-driven hand robot," *Journal of Electromyography and Kinesiology*, vol. 23, no. 5, pp. 1065–1074, 2013.

[85] M. Dragusanu, M. Z. Iqbal, T. L. Baldi, D. Prattichizzo, and M. Malvezzi, "Design, development, and control of a hand/wrist exoskeleton for rehabilitation and training," *IEEE Transactions on Robotics*, 2022.

[86] P. W. Ferguson, B. Dimapasoc, Y. Shen, and J. Rosen, "Design of a hand exoskeleton for use with upper limb exoskeletons," in *International Symposium on Wearable Robotics*, pp. 276–280, Springer, 2018.

[87] C. Li, Z. Rusák, I. Horváth, L. Ji, and Y. Hou, "Current status of robotic stroke rehabilitation and opportunities for a cyber-physically assisted upper limb stroke rehabilitation," in *Proceedings of TMCE*, vol. 1, pp. 899–914, 2014.

[88] Y. Liu and P. Ben-Tzvi, "Design, analysis, and integration of a new two-degree-of-

freedom articulated multi-link robotic tail mechanism," *Journal of Mechanisms and Robotics*, vol. 12, no. 2, p. 021101, 2020.

[89] W. Xu, Y. Liu, and P. Ben-Tzvi, "Design, analysis, and prototyping of a novel single degree-of-freedom index finger exoskeleton mechanism," in *International Design Engineering Technical Conferences and Computers and Information in Engineering Conference*, vol. 86281, p. V007T07A047, American Society of Mechanical Engineers, 2022.

[90] W. Xu, Y. Liu, and P. Ben-Tzvi, "Development of a novel low-profile robotic exoskeleton glove for patients with brachial plexus injuries," in *2022 IEEE/RSJ International Conference on Intelligent Robots and Systems (IROS)*, pp. 11121–11126, IEEE, 2022.

[91] C. Della Santina, M. Bianchi, G. Averta, S. Ciotti, V. Arapi, S. Fani, E. Battaglia, M. G. Catalano, M. Santello, and A. Bicchi, "Postural hand synergies during environmental constraint exploitation," *Frontiers in Neurorobotics*, vol. 11, no. August, pp. 1–14, 2017.

[92] J. Lin, Y. Wu, and T. S. Huang, "Modeling the constraints of human hand motion," *Proceedings - Workshop on Human Motion, HUMO 2000*, pp. 121–126, 2000.

[93] P. W. Ferguson, Y. Shen, and J. Rosen, "Hand exoskeleton systems—overview," *Wearable Robotics*, pp. 149–175, 2020.

[94] J. Park, N. Pažin, J. Friedman, V. M. Zatsiorsky, and M. L. Latash, "Mechanical properties of the human hand digits: Age-related differences," *Clinical Biomechanics*, vol. 29, no. 2, pp. 129–137, 2014.

[95] D. Di Febbo, E. Ambrosini, M. Pirotta, E. Rojas, M. Restelli, A. L. Pedrocchi, and S. Ferrante, "Does reinforcement learning outperform pid in the control of fes-induced elbow flex-extension?," in *2018 IEEE International Symposium on Medical Measurements and Applications (MeMeA)*, pp. 1–6, IEEE, 2018.

[96] J. Schulman, F. Wolski, P. Dhariwal, A. Radford, and O. Klimov, “Proximal policy optimization algorithms,” *arXiv preprint arXiv:1707.06347*, 2017.

[97] T. P. Lillicrap, J. J. Hunt, A. Pritzel, N. Heess, T. Erez, Y. Tassa, D. Silver, and D. Wierstra, “Continuous control with deep reinforcement learning,” *arXiv preprint arXiv:1509.02971*, 2015.